CHARMED MESON MEASUREMENTS USING A SILICON TRACKER IN AU+AU COLLISIONS AT $\sqrt{S_{NN}} = 200$ GEV IN STAR EXPERIMENT AT RHIC

A dissertation submitted to
Kent State University in partial
fulfillment of the requirements for the
degree of Doctor of Philosophy

by

Jaiby J. Ajish

December, 2011

Dissertation written by

Jaiby J. Ajish

B.Sc., Mahatma Gandhi University, 2000

M. Sc., Mahatma Gandhi University, 2002

Ph.D., Kent State University, 2011

Approved by

Dr. Spyridon Margetis, _____ Chair, Doctoral Dissertation Committee

Dr. Declan Keane, _____ Members, Doctoral Dissertation Committee

Dr. Mark Manley, _____

Dr. Sonia Kabana, _____

Dr. Robert Twieg, _____

Dr. Jin Ruoming, _____

Accepted by

Dr. Jim Gleeson, _____ Chair, Department of Physics

Dr. John R.D. Stalvey, _____ Dean, College of Arts and Sciences

Table of Contents

List of Figures

List of Tables

Acknowledgments

To the memory of my father. He instilled in me the importance of education and taught me to dream big and reach for the stars. Your memories never fade and the example you set still inspires me. I thank you for all the affection you showed me and for watching over me from the heaven.

My thanks and appreciation goes to my advisor, Spiros Margetis, for taking me as his student and for all the support he gave me over the years. He initiated me into the world of advanced research and taught me the art of thinking critically. His candid and humorous comments, while creating lighter moments, also stimulated thought. I cherish and appreciate the training and guidance received from him.

The members of my dissertation committee, Declan Keane, Mark Manley, Sonia Kabana, Robert Tweig, and Jin Ruoming have generously given their time and expertise to improve my work. I thank them for their contribution. I am thankful to Jonathan Bouchet, who helped me get started with ROOT programming and being patient with my constant pestering. I am grateful to members of the Kent State Nuclear group, with whom i worked over the years, especially Joe, Wei-Ming, Yadav and Jeremy for some enlightening discussions on the subject.

This work was done in collaboration with Yuri Fisyak and Victor Perevoztchikov of Brookhaven National Lab (BNL) and the University of Nantes group under Sonia Kabana. I am grateful to the collaborating members for their contribution. One of the best learning experience I had during my research was the presentation sessions by students. I deeply appreciate the time and effort of Declan Keane who was always

present at those sessions and gave us his feedback. I thank the members of the STAR collaboration, especially the heavy flavor group, who provided every help possible. I also want to acknowledge the friendship and support of my colleagues at BNL, where i spent two years for my research.

I am grateful to S. Sankararaman, one of the best teachers I had, for inspiring me to aim higher. I also thank all my physics teachers for imparting the knowledge that sparked my interest in the subject. I would like to acknowledge my many good friends who cared for me and gave me emotional support. I express my deep appreciation for Sheeba, Limsy, Biby, Ancy, Sinu, Hari, Fanindra, Madhabi, Saonti, Reeba, Revathy, Sylvia and to the Reith family. The love and support of my friends in Kent made this city a home away from home for me. I thank the office staff at Physics Department, Loretta, Cindy, Kim and Chris for their support - it really felt like a family with all of you around.

I thank my mom for her unflinching support. Your prayers and love give me strength to move on. I wouldn't have reached here without you. I thank my brothers and sisters for their love and affection. Special thanks to *Kunjettai* for being there. Thank you *Chachan*, *Amma* and *Veena* for understanding and loving me. I thank my uncle, Abraham for supporting me.

My husband, Ajish, patiently waited for me during the course of this degree. You always encouraged me when the journey of life seemed rocky. I sincerely appreciate the emotional support you gave, especially during the home stretch. My daughter Annie has been the greatest joy of my life. Watching her giggle brighten up my days.

Finally, I thank God almighty for every blessing I have received.

Chapter 1

Introduction

The initial condition of the universe is not precisely known, but it is now widely accepted that the universe started out with the Big Bang, as an initial hot stage some 10^{10} years ago and that it is continuously expanding, even today. At RHIC (Relativistic Heavy Ion Collider), we try to recreate the Big Bang by colliding heavy ion beams at velocities close to light speed, which creates a "little bang" capable of shedding some light onto what happened moments after the Big Bang. We aim particularly at studying the strong interaction thermodynamics in the laboratory; to explore color deconfinement and the resulting new state of matter. Phenomenological models have done a great deal to form the concepts of the field. Quantum Chromo Dynamics (QCD) is the basis for our current understanding of the hot and dense matter and it provides us the tools to probe it. In this chapter, I will provide a brief summary of the most important pieces of the theoretical framework, their underlying assumptions and their most robust predictions. The chapter concludes with some of the important observations from RHIC.

1.1 The Standard Model

The Standard Model is the theory of elementary particles and their interactions. It was formulated in the 1970s and is currently well established. It is a synthesis of three of the four forces of nature: strong, electromagnetic and weak interactions. The goal of this theory is to find a common ground for the fundamental forces and thus it

falls short in explaining the effects of gravitational interactions. The Standard Model describes elementary particles: bosons and fermions. Bosons have integer spin and fermions have half - integer spin. The fermions in the Standard Model are particles that make up matter. The bosons are generally particles that transmit the forces.

The fermions in the Standard Model are classified into six quarks (up, down, charm, strange, top, bottom) and six leptons (electron, electron neutrino, muon, muon neutrino, tau, tau neutrino). This classification is done based on how they interact and what charges they carry. Quarks have non-integer charge and leptons have integer charge. Each fermion has a corresponding antiparticle. The particles that make up the matter are grouped into three generations. The gauge bosons in the Standard Model are photons (γ) - for the electromagnetic interaction, gluons (g) - for the strong interaction and W and Z bosons - mediating the weak force. Table 1.1 shows how the fermions are organized. The gauge bosons are also shown.

The quarks carry color charge labeled red, blue and green. The antiquarks carry anticolor, namely, anti-red, anti-blue and anti-green. Through the confining behavior of strong interaction, quarks form composite particles and remain color neutral. These color neutral composite particles are referred to as hadrons. Thus, all observable particles in our physical world are color neutral. The color charge was introduced to explain how quarks could coexist inside hadrons in identical quantum states without violating the Pauli exclusion principle. The strong interaction is mediated through gluons. Gluons themselves carry color and hence participate in strong interactions in addition to mediating it. Figure 1.1 shows some examples of strong interactions. Gluons interact only with particles carrying color. There are eight independent gluon color states, which can be considered as "combined states" of color and anticolor

PARTICLE FAMILY	NAME (SYMBOL)	CHARGE $[\lvert q_e \rvert]$	MASS $[\mathrm{MeV}/c^2]$
	FIRST GENERATION		
Quarks	Up (u)	$+2/3$	1.5-3.3
	Down (d)	$-1/3$	3.5–6
Leptons	Electron (e^-)	-1	0.511
	Electron neutrino ($\bar{\nu}_e$)	0	$\leq 2.2 \cdot 10^{-6}$
	SECOND GENERATION		
Quarks	Charm (c)	$+2/3$	1160–1340
	Strange (s)	$-1/3$	70–130
Leptons	Muon (μ^-)	-1	105.7
	Muon neutrino ($\bar{\nu}_\mu$)	0	≤ 0.17
	THIRD GENERATION		
Quarks	Top (t)	$+2/3$	171300±1200
	Bottom (b)	$-1/3$	4130–4370
Leptons	Tau (τ^-)	-1	1776.84
	Tau neutrino ($\bar{\nu}_\tau$)	0	≤ 15.5

FORCE	GAUGE BOSONS	MASS $[\mathrm{GeV}/c^2]$	ELECTRIC CHARGE $[\lvert q_e \rvert]$
Strong	g (8 gluons)	0	0
Electromagnetic	γ (photon)	0	0
Weak	$W^\pm$	80.3980 ± 0.0250	± 1
	Z^0	91.1876 ± 0.0021	0

Table 1.1: Overview of the three generations of fermions that make up matter. The bottom part shows the bosons that mediate strong, electromagnetic and weak interactions. Values are taken from [1]

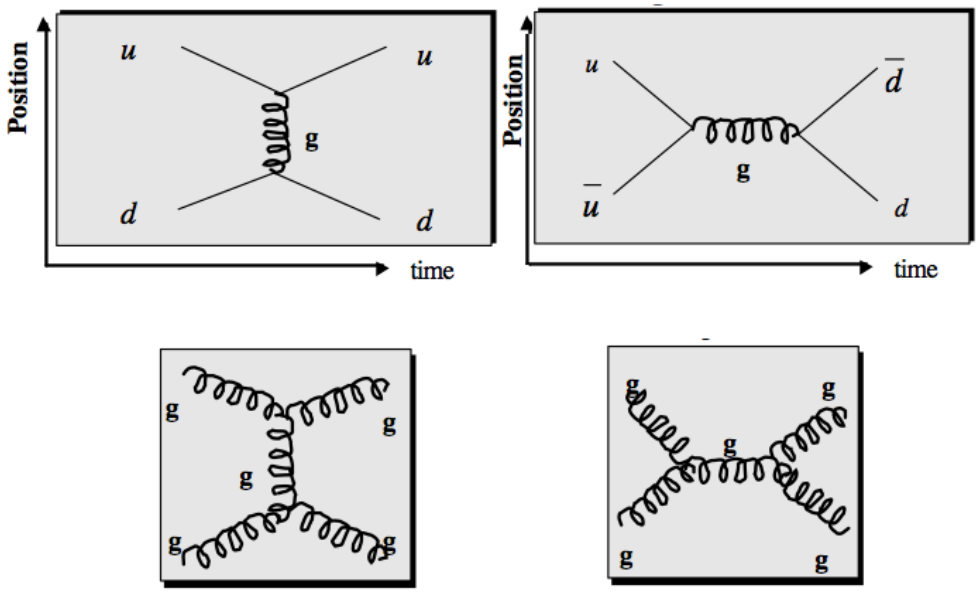

Figure 1.1: Examples of Strong Interaction

charges.

The color confinement can be disrupted only at high temperatures and high densities, creating a new state of matter where quarks and gluons can propagate a longer distance. Hadrons contain quarks and antiquarks. Hadrons are classified into mesons (normally containing a quark and antiquark) and baryons (normally containing three quarks). The leptons on the other hand, do not carry color charge. However, because of the electric charge in electron, muon and tau, they can interact electromagnetically. The neutrinos do not carry electric charge and hence they are influenced by the weak nuclear force only. There is a classification scheme for the hadrons –The Quark Model. This was necessary as more and more particles were discovered. The quarks and antiquarks gives rise to quantum numbers for hadrons, and these are used for identifying and classifying the hadrons.

1.2 Quantum Chromo Dynamics (QCD)

QCD is the theory of strong interactions and an important part of the Standard Model. It describes the interactions between quarks and gluons, and in particular how they bind together to form hadrons. In ultra-relativistic heavy ion collisions, we apply this model to complex and dynamically evolving systems of finite size and under extreme temperature and density. A new state of the matter is formed when the energy density exceeds the typical hadronic value of 1 GeV/fm^3. In this condition, matter no longer contains hadrons, which melt into their constituent quarks and gluons, a phase known as the Quark Gluon Plasma (QGP). According to STAR's 2003 white paper [2], we can define QGP as a (local) thermally equilibrated state of matter in which quark and gluons are deconfined from hadrons, so that color degrees of freedom become manifest over nuclear, rather than merely nucleonic, volumes [2].

Based on the two assumptions of high temperature and/or high density for Quark Gluon Plasma, we might find QGP in three places: (i) in the early Universe, (ii) at the center of compact stars and (iii) in the initial stage of colliding heavy nuclei at high energies. The early Universe, experienced an expansion from a singularity at time zero. If we extrapolate our expanding universe backward in time towards the Big Bang, the matter and radiation become hotter and hotter, resulting in a primordial fireball[1]. If we go back in time to $10^{-5} \sim 10^{-4}$s after its inception, the universe is likely to have experienced the QCD phase transition at a temperature in the range of $150 \sim 190$ MeV (corresponding to an energy density of about 1 GeV/fm^3) and an electro-weak phase transition at T $\sim$ 200 GeV, as shown in Fig. 1.2.

[1]Named by Gamow. The discovery of T $\sim$ 2.73 K $\sim 3 \times 10^{-4}$ eV Cosmic Microwave Background (CMB) radiation by Penzias and Wilson (1965) confirmed the remnant light of this hot era of the Universe.

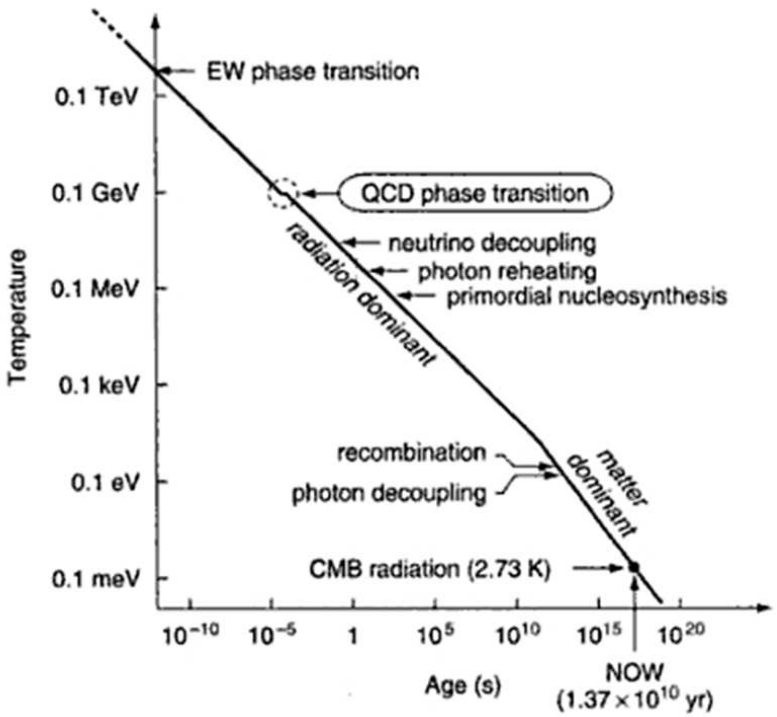

Figure 1.2: Evolution of the Universe: Temperature vs Time

At the core of super dense stars, when the central density of the neutron star reaches 5-10 times the density of normal baryonic matter ($\sim 0.16\text{fm}^3$) there is a possibility of the existence of quark matter. So far there is no convincing evidence of the existence of quark stars.

In relativistic heavy ion collisions, we accelerate heavy ions to very high energies and cause a head-on collision. When the beams are accelerated to relativistic energies, the nuclei are Lorentz-contracted like a "pancake". When the energy per nucleon is about 100 GeV, the colliding nuclei pass through each other creating very high density and temperature or a "fireball". The QGP supposedly created in the initial stages of the collision cools rapidly to a hadron gas through the QCD phase transition. Even before accepting QCD as the theory for strong interactions, there

were assumptions that 1) The phenomena of quark confinement was a result of the non-perturbative structure of the vacuum and 2) that this vacuum structure is modified at high temperatures and/or densities, suggesting that a strongly interacting new phase of matter is formed. It was a great triumph of modern particle physics when QCD could successfully account for the strong interactions processes observed at the colliders, most notably the dramatic phenomena of hadronic jet and heavy quark production. (These will be discussed later in this chapter).

1.2.1 QCD Phase Diagram

A schematic phase diagram of QCD matter is shown in Fig. 1.3 in the plane of temperature, T, and baryon density, ρ. There are basically two phases: the hadronic phase and the QGP phase.

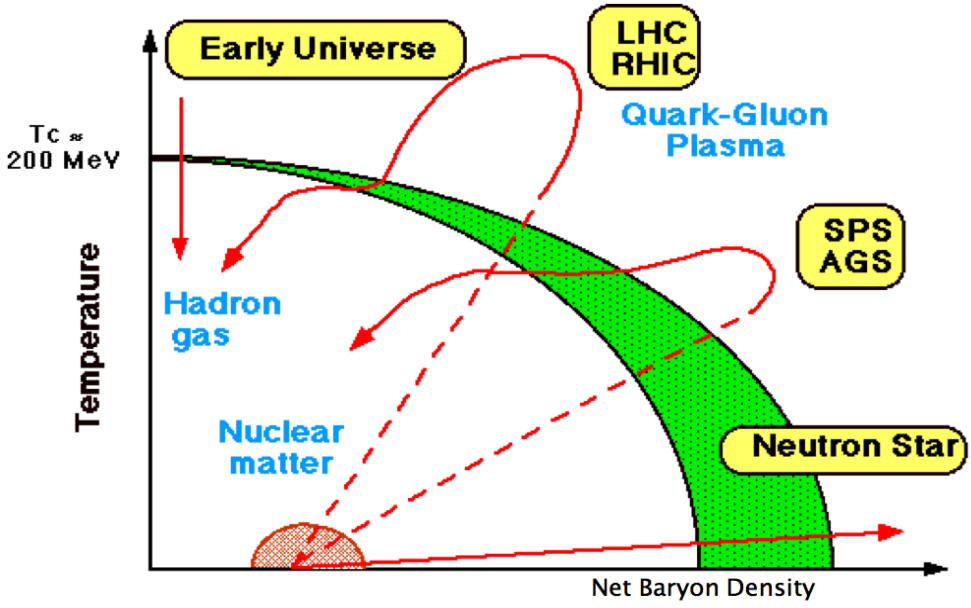

Figure 1.3: QCD Phase Diagram: Temperature vs Baryonic Density

The left arrow that points down shows the path taken by the early universe, as it cooled from the QGP phase to normal nuclear matter. The bottom arrow shows

the path taken by neutron stars in their formation. Heavy ion collisions follow a path between these two extremes. Possible phases of QCD and the precise locations of critical lines and critical points are currently being actively studied. The search for Color Glass Condensate[2] (coherent, high density gluons) is a rigorously followed field. Unraveling the QCD phase structure is one of the central aims of future theoretical and experimental research in the field of QCD. In heavy ion collisions, a QGP is created if the temperature of the system exceeds the critical temperature, T_c (theoretical calculations using lattice QCD predicts $T_c \sim 170$ MeV[4], which corresponds to energy density $\sim 1\text{GeV/fm}^3$, nearly an order of magnitude larger than cold nuclear matter).

Figure 1.4 shows the space-time evolution of a heavy ion collision. After the creation of the QGP, the system expands, cools and passes through chemical freeze out temperature T_{ch} where the inelastic scatterings stop and the relative abundance of particle types stabilizes. The system further cools off and kinetic freeze-out occurs at T_{fo}, below which the elastic collisions also end. At this point, the particles move towards the detectors without anymore space interactions.

1.2.2 Asymptotic Freedom and Confinement in QCD

QCD provides us with two important characteristics of quark-gluon dynamics. At high energies, the interaction becomes small, and quarks and gluons interact weakly - this is asymptotic freedom. At low energy, the interaction becomes strong and leads

[2]The hadron cross section increases very slowly with energy, whereas the gluon density rises much more rapidly. The number of gluons in a hadron wave function is usually measured in terms of the ratio of the gluon energy to the total energy of a hadron in a frame where the hadron has very high energy, $x = \frac{E_{\text{gluon}}}{E_{\text{hadron}}}$. As x decreases, the gluon density increases. The high-energy limit is the high gluon density limit. High phase-space density gives rise to a condensate. Studying the low-x properties can shed light onto the origin of glue and sea quarks and the initial conditions for the formation of Quark-Gluon Plasma.

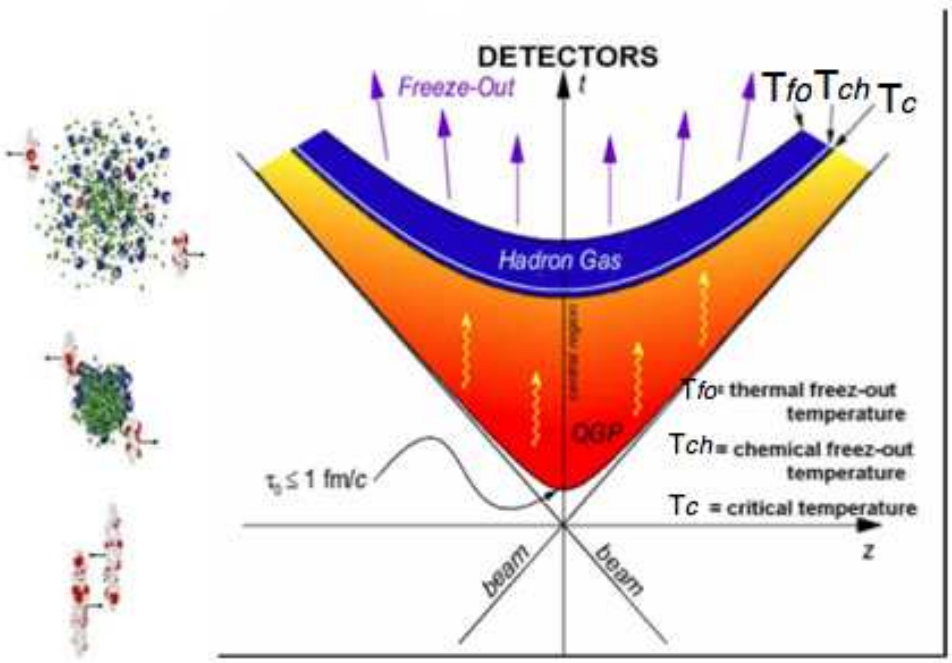

Figure 1.4: The space-time picture - Evolution stages of relativistic heavy ion collision

to the confinement of color. The asymptotic freedom is related to the anti-screening of color charge. Because the gauge fields themselves have color, a bare color charge centered at the origin is diluted away in space by the gluons. Therefore as one tries to find the bare charge by going through the cloud of gluons, one finds a smaller and smaller portion of the charge. This is in sharp contrast to the case of Quantum Electro Dynamics (QED), where the screening of a bare charge takes place due to a cloud of, for example, electron-positron pairs surrounding the charge.

Shown in Fig. 1.5 is an illustration of the effective (or running) coupling constant in QCD (QED) with the anti-screening (screening) feature [3]. The typical length scale decreases as the energy scale increases. QCD predicts that the strong coupling strength α_s decreases with increasing energy or momentum transfer (Q^2). α_s shows

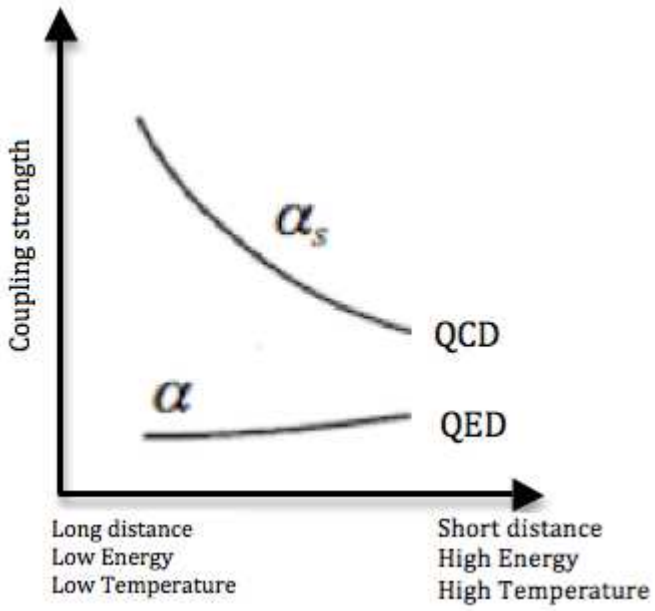

Figure 1.5: Response of coupling strength with distance scale - QCD and QED

a logarithmic decrease with increasing Q^2:

$$\alpha_s(Q^2) \propto \frac{1}{\ln(Q^2/\Lambda^2)} \tag{1.1}$$

This is why we can expect QGP at high temperatures, for which the typical thermal energies of the quarks and gluons are large and thus the interactions become weak. Figure 1.5 also indicates that the interaction in QCD becomes stronger at long distances or low energies. This is the color confinement. Thus the potential between a quark and antiquark at large separation increases linearly, and even if we try to separate the quark and antiquark, they cannot be forced apart. Beyond some critical distance, the potential energy becomes large enough such that a new quark-anti quark pops up from the vacuum. Then the original quark antiquark pair becomes two pairs. This way, quarks are always confined inside hadrons and can

never be isolated in QCD.

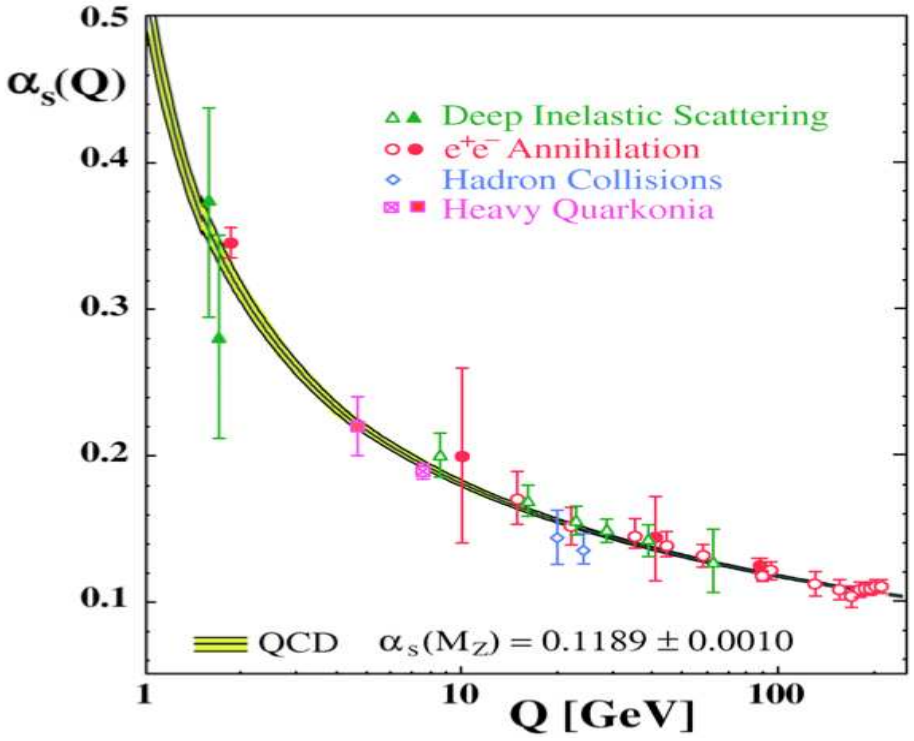

Figure 1.6: Summary of measurements of $\alpha_s(Q)$

The concept of asymptotic freedom, i.e., the QCD prediction of an inverse logarithmic decrease of the coupling strength, α_s, with the energy or the momentum transfer in high energy scattering reactions was shown to be significantly and reliably verified by a number of different measurements. They demonstrate evidence for the running of α_s. Figure 1.6 shows a summary of various measurements from different experiments [5].

The dynamics of quarks and gluons are controlled by the QCD Lagrangian. The large number of field components, and the presence of the self-interaction terms, together with a large value of the QCD coupling constant α_s, make the calculations

of the non-perturbative QCD very complicated. For large values of Q^2 ("hard collisions"), one can use perturbative methods, while for small Q^2 ("soft collisions") numerical methods are used. Various techniques have been developed to work with QCD. Some of these are discussed below.

1.2.3 Perturbative QCD (pQCD)

This method assumes asymptotic freedom at very high energies to utilize perturbation theory. It has produced some accurate results in QCD to date, although it is limited in scope. In order to use it, the requirement is $\alpha_s \ll 1$. At high energies where α_s is small, we can use perturbative techniques to predict the various subprocesses. Descriptions of hadronic production are possible in perturbative QCD when the mass of the produced quark is large compared to 1 GeV/c^2, the typical scale of strong interactions.

1.2.4 Lattice QCD (LQCD)

Because the QCD coupling strength α_s becomes large at long distances, we cannot adopt a perturbative method in this regime. Also perturbation theory never reveals the physics of a phase transition, which is intrinsically non-perturbative. Therefore lattice QCD is used as a framework to investigate non-perturbative phenomena such as confinement and quark-gluon plasma formation.

Lattice QCD is a powerful method that treats four-dimensional space-time as a lattice, in which quarks occupy lattice points while the gauge field occupies lattice links. The quarks and gluons reside on the lattice points. Naturally, it introduces a momentum cut off at $\frac{1}{a}$, where a is the lattice spacing. Therefore lattice QCD is mathematically well defined. The calculations can reproduce some of the pQCD

results. It is approximated to a continuum by reducing the spacing between vertices to as low as possible. However, it has uncertainties related to the limitations on the lattice spacing and on the size of the lattice. It is difficult to reduce the lattice spacing in order to reach the continuum and to extend its size due to limited computing power.

At finite temperatures, recent lattice simulations describe the QCD thermodynamics reliably, since larger volumes and quark masses closer to their physical values are used [6][7][2].

1.2.5 Phenomenological Models

While the techniques for studying perturbative QCD have been well developed, analytical and numerical solutions of problems in non-perturbative QCD are rather difficult to obtain. Various models of QCD have been proposed, such as the MIT bag model, the potential model, the Nambu-Jona-Lasinio (NJL) Model, the Parton Model, the Dyson-Schwinger Model, etc. They are widely used and are quite useful in elucidating some of the essential features of QCD in the non-perturbative regime. In the MIT bag model, quarks are treated as massless particles inside a bag of finite dimension and are infinitely massive outside the bag.

1.3 Predicted Signatures of QGP

Experimental results from AGS (Alternating Gradient Synchrotron), SPS (Super Proton Synchrotron) and RHIC (Relativistic Heavy Ion Collider) have stimulated impressive theoretical advances in the past decade on the thermodynamic and hydrodynamic properties of the hot and strongly interacting matter and the propagation of partons through the medium. However, the complexities of heavy ion collisions and hadron formation bring in ambiguities to such models. The following are some

of the robust predictions of the formation of QGP, which survive the quantitative ambiguities.

1.3.1 Features of Quark-Hadron Phase Transition

At low temperature (T) and low baryon density (ρ), QCD exhibits dynamical breaking of chiral symmetry (exhibit actual quark current mass) and confinement. On the other hand, at sufficiently high temperatures and densities (T and $\rho^{\frac{1}{3}}$ much larger than the QCD scale parameter[3] $\Lambda_{QCD} \sim 200$ MeV.) the QCD running coupling constant becomes small. Furthermore, the long-range color electric force is subject to plasma screening and becomes short-ranged. These considerations suggest that the QCD vacuum undergoes a phase change at some values of $T(T_c)$ and ρ. This phase transition restores the broken chiral symmetry, i.e., makes the quarks behave as though they are massless [7]. Various model approaches and numerical simulations of QCD strongly indicate the existence of a transition from the hadronic phase to the quark-gluon phase. The new color degrees of freedom would then be manifested as a rapid increase in entropy density, hence in pressure, and by a consequent change in the equation of state (EOS). The transition can be understood in terms of the number of degrees of freedom [8]. Above the transition temperature, the gluon and quark degrees of freedom are activated. For gluons, 8(color) $\times$ 2(spin) gives a total of 16 degress of freedom and for quarks, 2-3 (light flavors) $\times$ 2 (quark-antiquark) $\times$ 3

[3]The QCD scale parameter and the running coupling are related (also given in Eq.1.1) by the following equation:

$$\alpha_s(k^2) = \frac{4\pi}{\beta_0 \ln(k^2/\Lambda^2)}, \tag{1.2}$$

where $\beta_0 = 11 - \frac{2}{3}n_f$, with n_f the number of light quarks. According to the generally adopted convention one defines the value of α_s at the mass of the Z^0 boson to be $\alpha_{m_z} = 0.118 \pm 0.002$. This gives the value of the scale constant $\Lambda = 217^{+25}_{-23}$MeV

(colors) $\times$ 2 (spin) gives a total of 24-36 degrees of freedom. Thus, in the Quark-Gluon Plasma there are about 40-50 internal degrees of freedom in the temperature range (1-3)T_c. As the number of degrees of freedom increases, energy density increases. In the limit, where the deconfined quarks and gluons are non-interacting and the quarks are massless, the Stefan-Boltzmann pressure P_{SB} of this partonic state as a function of temperature T, at zero chemical potential (i.e., zero net quark density), would be simply determined by the number of degrees of freedom:

$$\frac{P_{SB}}{T^4} = [2(N_c^2 - 1) + \frac{7}{2} N_c N_f] \frac{\pi^2}{90}, \tag{1.3}$$

(Stefan-Boltzmann law for massless bosons with degeneracy $P \propto T^4$),

where N_c is the number of colors and N_f is the number of quark flavors. Here we took $\hbar = c = 1$. The two terms on the right represent the gluon and quark contributions respectively. Refinements to this equation to incorporate effects of color interactions among the constituents, non-vanishing quark masses and chemical potential, in order to predict the transition point from hadronic to partonic degrees of freedom are done with lattice QCD. To get physically relevant predictions, we extrapolate the lattice spacing to the continuum (lattice spacing$\rightarrow$ 0), chiral mass to actual current quark mass and thermodynamic (large volume) limits. Within the constraints of computing cost and technical complications lattice QCD calculations have put forth the predictions described below.

Thermodynamics: There is a transition between hadronic and QGP phase occurring at a temperature in the vicinity of $T_c \sim 170$ MeV (150-200 MeV) for zero chemical potential. The pressure divided by T^4 rises rapidly above T_c, then begins to saturate by about $2T_c$, but the values are substantially below the Stefan-Boltzmann (SB) limit. This is expected since the number of degrees of freedom increases steeply

corresponding to a transition to the deconfined quarks and gluon state. The deviation from the SB limit indicates the remaining interactions among the quarks and gluons in the QGP phase. There is a significant change in energy density as well. The dependence of the energy density ϵ, divided by T^4 on $T = T_c$ and pressure divided by T^4 is presented in Fig. 1.7[9]. The nature of the transition from hadronic to QGP phase is highly sensitive to the number of dynamical quark flavors included in the calculation and to the quark masses.

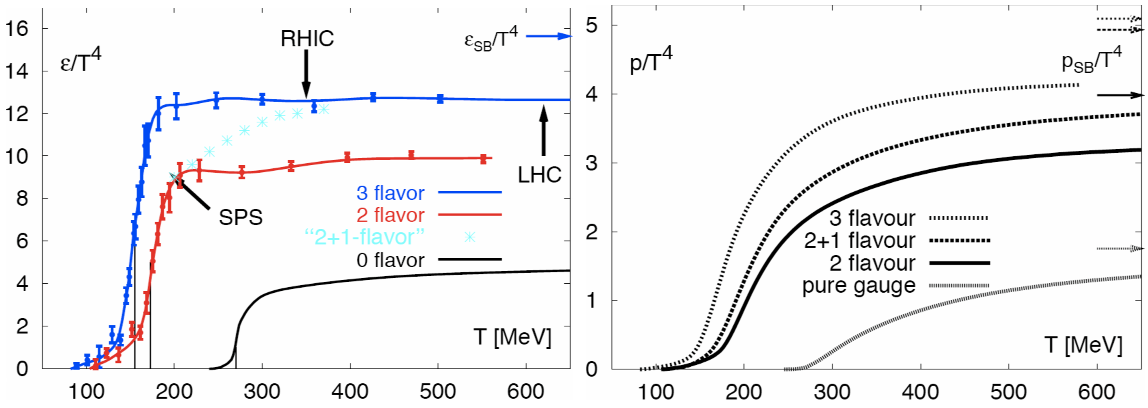

Figure 1.7: Lattice QCD calculation for the energy density and pressure vs temperature.

J/ψ **Suppression**: Matsui and Satz (1986) proposed that the J/ψ yields in relativistic heavy ion collisions is suppressed because the binding potential becomes short-ranged due to the color Debye-screening [10]. Above T_c, the effective potential between a heavy quark-antiquark pair takes the form of a screened Coulomb potential, with screening mass (or inverse screening length) rising rapidly as temperature increases above T_c [11]. The increased screening mass leads to a shortening of the range of the $q\bar{q}$ interaction, and thus a suppression of the J/ψ, the bound state of charm and anti-charm ($c\bar{c}$), in relation to open charm [10]. Figure 1.8 shows the strong deviation of the screening mass from perturbative QCD expectations in the vicinity of

T_c, which indicates large non-perturbative effects. A sufficiently strong reduction in the number of J/ψ particles leaving the fireball suggests that hot quark-gluon plasma was made in the initial stages of collision.

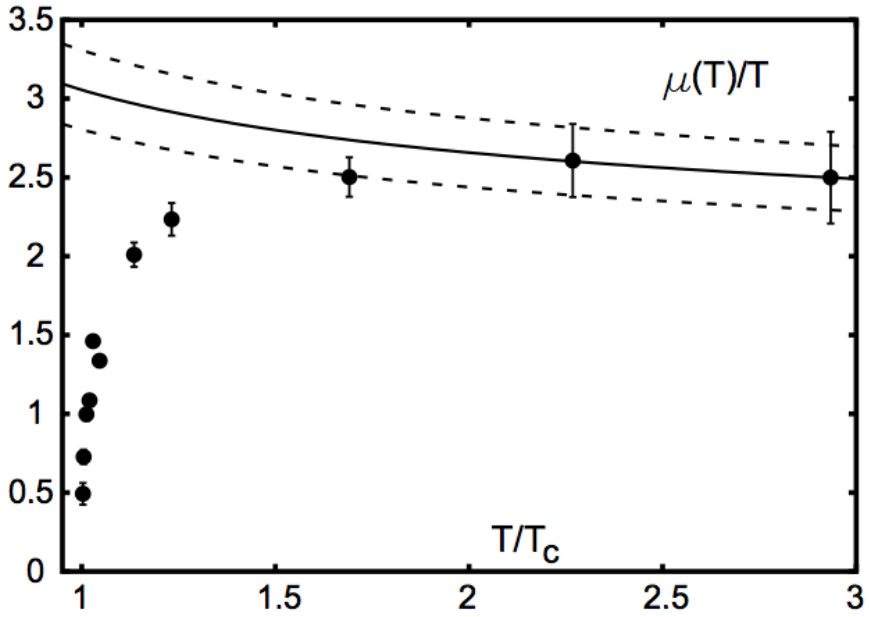

Figure 1.8: Temperature dependence of heavy-quark screening mass.

Strangeness Production Enhancement: The strangeness production enhancement is another central prediction for the formation of QGP. There are two factors behind this enhancement. 1) The production mechanism for producing strange particles in QGP is different from a hadron gas. 2) The equilibrated time scale for strange particle production is much smaller in QGP than in hadron gas [12]. Therefore dynamical effects do not suppress the produced strange particles.

In QGP, the associated production of $s\bar{s}$ can proceed by the fusion of two gluons or two light quarks (q = u, d). So in that case, the energy threshold for strange particle production is given by the mass of the strange-antistrange quark pair, $E^{\mathrm{QGP}}_{\mathrm{threshold}} =$

$2m_s \sim 300$ MeV, where m_s is the mass of the strange quark. On the other hand, hadronic strangeness production proceeds in vacuum with a considerably larger energy threshold, most often via $\pi\pi \longrightarrow K\bar{K}, \pi N \longrightarrow K\Lambda, NN \longrightarrow N\Lambda$K. In the first case, the energy threshold is

$$E^{\mathrm{HG}}_{threshold} = 2M_K - 2M_\pi \sim 710\mathrm{MeV}. \tag{1.4}$$

The second and third production channels also give comparable values, ~ 670 MeV and ~ 530 MeV, respectively. Thus, in a hadron gas, the threshold is considerably larger (~ 600 MeV) compared to QGP (~ 300 MeV). The number of strange quarks produced can give us some insight on QGP since their production requires more energy than the production of up and down quarks. Furthermore, since multi-strange

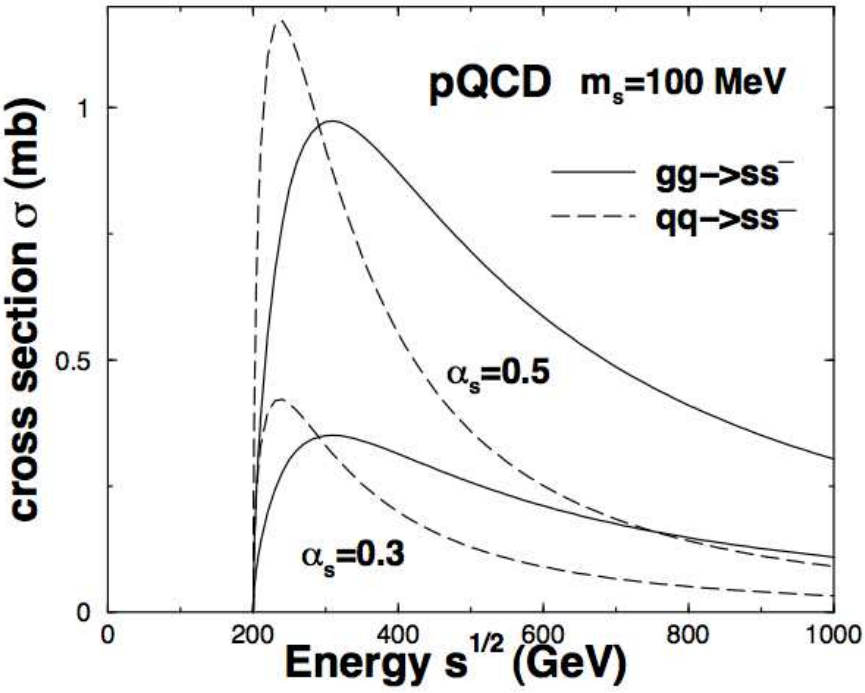

Figure 1.9: Strangeness production cross section as a function of colliding energy

hadrons have to be created in multi-step reactions, i.e., first a strange particle and then a multi-strange one, they are even more suppressed than the single-strange hadrons in the hadron gas compared to QGP. The strange-antistrange quark pair production via gluon fusion dominates over the quark production cross section for higher energies (see Fig. 1.9). In addition, the mass of the strange quarks and antiquarks ($m_s \sim 100$ MeV) is of the same magnitude as the temperature at which the hadrons (protons, neutrons etc) are expected to melt into quarks [4]. This means that the abundance of strange quarks is sensitive to the conditions, structure and dynamics of the deconfined-matter phase.

Hard Partons (high p_T probes): Quarks and gluons with very high energies might be formed during the early stages of a collision. These high transverse momentum partons result from the initial hard scattering (large momentum transfer) of nucleon constituents. After a hard scattering, the parton undergoes fragmentation to create a high-energy cluster (jet) of particles. A high momentum parton traversing the medium is subjected to large energy loss and may be absorbed in the medium. The disappearance of the back-to-back partner of the dijet, which goes into the bulk matter generated in the collisions is known as jet quenching. Hard scattering processes have been established at high transverse momentum (p_T) in elementary collisions at high energy. When such a parton traverses deconfined matter it can lose energy by gluon radiation[4], which results in a suppression of the fragmenting high p_T hadrons relative to the yield in baseline $p+p$ measurement [13]. Fast partons lose more energy per unit length in a QGP than in hadronic matter through gluon radiation; hence the energy loss might be a signal of whether QGP is created.

[4]The medium-induced radiative energy loss

Chiral Symmetry Restoration: The Chiral perturbation theory approach[5] assumes chiral symmetry, where quarks are assumed to be massless. For this reason, it cannot be applied to heavy quarks. In most calculations, the deconfining phase transition is also followed by the chiral symmetry restoration. In vacuum, the thermal expectation value $\langle q\bar{q}\rangle$ (order parameter for chiral symmetry breaking in the chiral limit, $m_q \to 0$) is a measure of the dynamical breaking of chiral symmetry at finite temperature and it tends to vanish at the QGP phase transition. $\langle q\bar{q}\rangle$ is called the quark condensate [7].

Elliptic Flow (v_2): In collisions of high energy nuclei, a large number of secondary particles is produced. Thus, occurrence of multi-particle correlations, or a collective phenomenon is expected and is observed. During non-central collisions, the

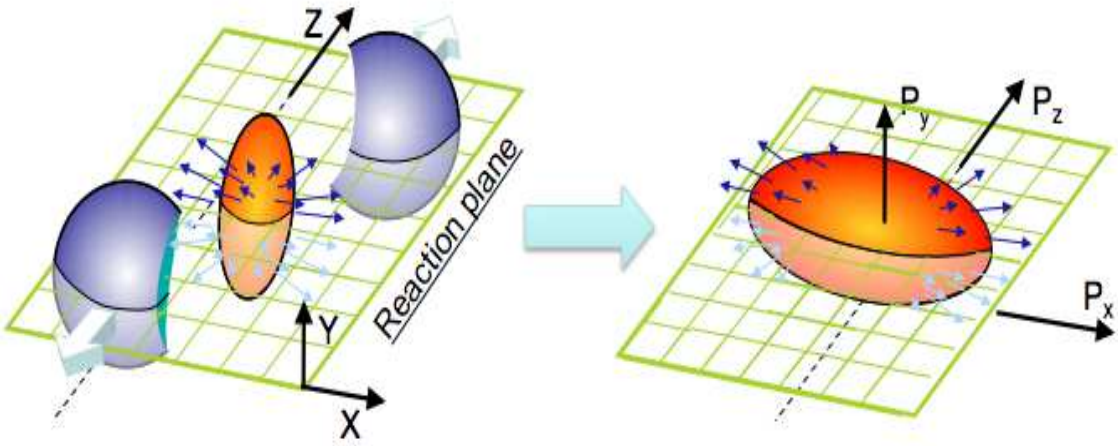

Figure 1.10: Schematic of the development of spatial anisotropy into momentum anisotropy

[5]Another theoretical approach to extract the low energy dynamics of QCD.

nuclear overlap is an ellipsoid in the early stages of a collision. This causes a pressure gradient and it is largest in the shortest direction of the ellipsoid. This initial spatial anisotropy develops into a momentum space anisotropy. Figure 1.10 shows a schematic of this process. We use only anisotropic transverse flow from the particle azimuthal distributions at fixed rapidity or pseudorapidity. The azimuthal distributions can be conveniently described by means of Fourier expansion [15]. Anisotropic flow corresponding to the first two harmonics plays a very important role and we use special terms for them, directed and elliptic flow, respectively. The "elliptic" comes from the fact that the azimuthal distribution of produced particles with non-zero second harmonic represents an ellipse.

Elliptic flow (v_2) is the second Fourier coefficient in the expansion of the azimuthal distribution of the particle with respect to the azimuthal angle ψ_{RP} of the reaction plane:

$$\frac{dN}{d\phi} \propto \Big\{1 + \sum_{n=1}^{\infty} 2v_n(p_{\mathrm{T}}, y)\cos(n\phi - \psi_{RP})\Big\}. \tag{1.5}$$

Because of the symmetry $\phi \leftrightarrow -\phi$ in the collision geometry, no sine terms appear in the above equation. The anisotropic flows v_n generally depend on the particle transverse momentum and rapidity. The coefficients v_n are calculated to be

$$v_n(p_{\mathrm{T}}, y) = \langle \cos n(\phi - \psi_{RP})\rangle \tag{1.6}$$

where $\langle \cdots \rangle$ denotes an average over the azimuthal distribution of all particles in all events studied. It has been shown that the elliptic flow is sensitive to the early dynamics of produced matter in relativistic heavy ion collisions and it is a robust observable for studying the interactions in the partonic matter [16][17].

The transition of ordinary matter into a soup of quarks and gluons happens under

extreme conditions. An estimate of the formation time relevant for the hydrodynamic calculations was predicted to be in the vicinity of $\tau_0 = 0.6$ fm/c, or approximately 10^{-24} s. This is shorter than the time taken by a massless particle to traverse the radius of a hadron ($\tau \sim 1$ fm/c). The temperature of this transition to QGP is about 150-200 MeV or 100,000 times the temperature of the center of the sun. The energy density is around $\epsilon = 30$ GeV/fm^3, and this should be compared with the energy density of a nucleon in its rest frame $\epsilon_N \sim 500$ MeV/fm^3, when the system is in local thermal equilibrium [18]. The hydrodynamic models suggest that collisions at RHIC make something that is hotter, denser, smaller and faster than anything observed before. No viscosity was needed to reproduce the RHIC data within experimental and theoretical uncertainities. Thus, the matter created at RHIC is a "nearly" perfect liquid. These extreme conditions permit us only to see the particles that escape from the fireball and reach the detector. These particles can retain the signatures of their past. We can use these signatures to work backwards in time to learn about the phase transition and the new matter created.

1.3.2 Heavy Quarks as a Probe of QGP

The results from RHIC so far, demonstrate that the partonic pressure gradient has been developed during the system evolution in heavy ion collisions. The next task is to test the local and early thermalization hypothesis experimentally. We expect the nucleons to undergo rapid thermalization if the Quark Gluon medium is created [19]. Heavy quarks (c, b), due to their early creation, can be valuable probes to this end. They are considered as the cleanest probes of QGP. Due to their heavier masses, heavy quarks require more rescatterings to reach a comparable collectivity as light quarks (u, d, s). If we observe the kinetic properties of these heavy quarks to

be similar to their lighter counterparts, then it is an indication of thermalization. If heavy quark collectivity is observed, there must be even more rescatterings happening among light quarks than expected, because the rescattering cross section among light quarks is larger than that between heavy and light quarks. So heavy quark collectivity indicates the thermalization of the light flavors, although heavy quarks themselves do not have to be thermalized. Therefore, measurement of heavy quark collectivity can give us pivotal information about the early thermalization of light quarks.

Charm quarks are a unique tool to probe the partonic matter created in collisions at RHIC energies. Gluon radiation is the dominant process for energy loss of high-energy partons traversing a strongly interacting medium. Due to their large mass ($\simeq 1.3$ GeV/c^2), charm quarks are predicted to lose less energy than light quarks by gluon radiation in the medium [22]. However, measurements of p_T distributions and nuclear modification factor through non-photonic electrons shows a suppression level similar to light hadrons [20][21]. The different energy loss mechanisms are not well understood so far, and thus it is an area of great interest.

Another factor that makes heavy quarks so interesting is that unlike light quarks, heavy quark masses are not modified by the excitations of the surrounding QCD medium during the heavy ion collisions. This is because the value of their masses is much higher than the initial excitation of the system. Thus the heavy quarks can retain valuable information about the medium formed in the collisions.

Bottom quarks, like charm, with their heavy mass, are expected to be produced early in the collision, and then to experience reduced coupling to the surrounding medium. However, since the bottom quark is heavier, it takes more energy for its creation, and is much rarer than charm. Both charm and bottom can be analyzed

through the single-electron decay channel, but analysis of the non-photonic electron[6] p_T distribution is complicated by an unknown mixture of charm and bottom contributions [23]. The single electron contribution from bottom is expected to become important at $p_T > 3$ GeV/c and would dominate above 4.5 GeV/c. This means we have to measure charm and bottom yields by direct topological reconstruction, since single electron spectra are not sufficient.

1.4 Important Results from STAR Experiment at RHIC

According to LQCD calculations, the transition to a QGP state occurs at energy densities $\sim$ 1GeV/fm^3. The energy density achieved at RHIC is well above this, and could be as high as $\sim$ 30 GeV/fm^3. In order to make strong conclusions about the medium created at RHIC, a variety of simultaneous studies are required. This is mostly due to the complexity of the system we are exploring here. The STAR detector at RHIC has several subdetectors capable of detecting many particle types and their momenta. In the previous years, STAR has gathered a wealth of data that has helped us to draw some strong conclusions about the formation and the properties of the medium created. Some of the most important QGP signatures observed at RHIC are: jet quenching, high p_T hadron suppression, collective flow and strangeness enhancement.

1.4.1 Jet Quenching and High p_T Hadron Suppression

The initial hard scattering of the nucleons produces high transverse momentum partons. These partons undergo fragmentation to create jets (a cluster of high energy particles). The jets are produced in pairs, and they travel in opposite directions.

[6] Electrons coming from heavy quarks, not from photonic conversions

When such a jet is created at the boundary of the fireball, one jet will travel out of the medium while the other jet will traverse the medium created. To measure this, we look for high momentum particles that are angularly correlated. To find a jet, we select a high momentum particle as the trigger particle and a second high momentum particle is found as a function of angular separation from the trigger particle. From two-particle azimuthal correlations, it was found that the "away-side" jet disappears in central AuAu collisions [25] compared to p+p data. QCD predicts that partons propagating through the QGP lose energy via gluon radiation with a magnitude depending strongly on the gluon density of the medium ($E_{\text{loss}} \sim dN_g/dy$). Figure 1.11 shows the measured azimuthal angular correlations of high p_T hadrons in

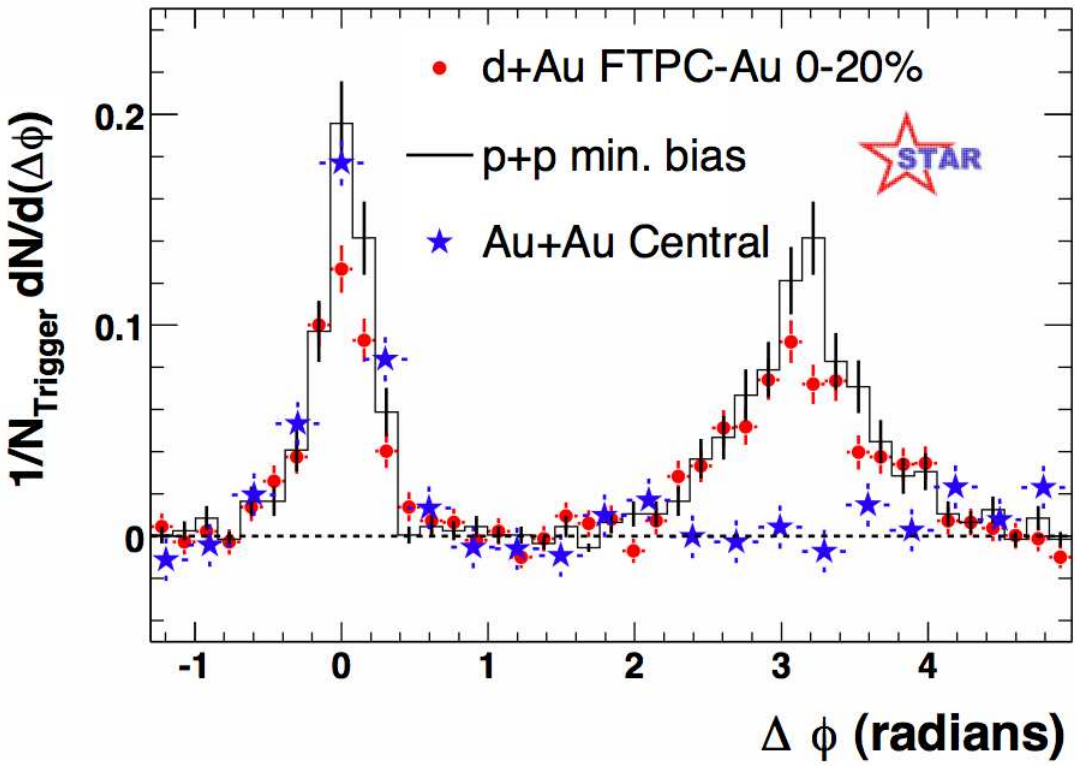

Figure 1.11: Dijet azimuthal correlations for hadrons in p+p, d+Au and Au+Au

p+p, d+Au and Au+Au collisions. No suppression is observed for the systems where the number participants is small, whereas in Au+Au there is a strong suppression observed for the high p_T partons (jets), indicating medium effects. In order to confirm that the observations in Au+Au are indeed due to the medium created during the collision, and not due to the initial-state effects, we look at d+Au collision results, where all the initial- state effects are the same but no final dense medium is created. As we can see from the figure, there is no jet quenching in d+Au, and this confirms the fact that quenching is a final-state effect.

The disappearance of the back-to-back partner of the dijet motivated a measurement of energy loss of high p_T partons as a function of p_T. For a comparison of spectra from nuclear collisions to a nucleon-nucleon (NN) reference, the nuclear modification factor, R_{AA} is defined as follows:

$$R_{AA}\left(p_T\right) = \frac{d^2N_{AA}(p_T)/dp_T dy}{(\langle N_{\rm coll}\rangle)(d^2N_{pp}(p_T)/dp_T dy)}. \tag{1.7}$$

It is the ratio of particle yield as a function of p_T in the nucleus-nucleus case (A+A) scaled by the number of binary collisions over the yield as a function of p_T in proton-proton collisions. R_{AA} can tell us if there are any medium effects. If there are no medium effects, R_{AA} should be unity for all p_T. The presence of QGP induces gluon radiation for high p_T partons, causing them to lose energy, and resulting in fewer high p_T particles. Figure 1.12 shows the significant suppression observed in a Au+Au system [26]. As can be seen from the figure, there is no suppression observed in d+Au [27] and it confirms the fact that high p_T hadron suppression is a final-state effect. It has been verified that hadronic energy loss cannot reproduce the factor of five suppression in Au+Au systems compared to d+Au, and thus points to the partonic energy loss, which can reproduce the observed suppression. However,

the four to five factor suppression is observed for the highest p_T in central Au+Au collisions. For the most peripheral collisions, R_{AA} is consistent with unity, while at intermediate centralities it smoothly interpolates between the two extremes. The strong suppression of the high p_T hadrons and the disappearance of the away-side correlation give strong evidence that a new medium is created at RHIC.

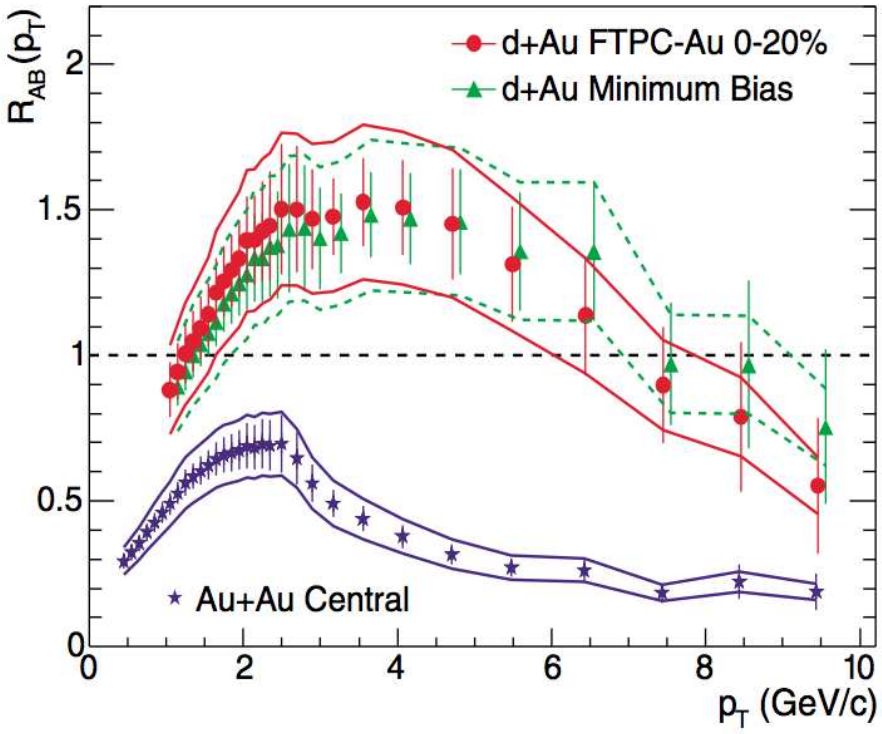

Figure 1.12: R_{dA} and R_{AA} plots for hadrons in STAR

1.4.2 Collective Flow

Substantial elliptic flow (v_2) signal is observed for a variety of particle species at RHIC, which might indicate their rapid thermalization. STAR measures the momentum anisotropy directly, whereas the initial spatial anisotropy is inferred indirectly from the centrality of the collision. Elliptic flow of multistrange hadrons (ϕ, Ξ and Ω)

was observed at STAR. Elliptic flow of these multistrange hadrons with their large masses and presumably small hadronic cross section [28] should be less sensitive to hadronic rescatterings in the later stage of the collision and therefore consistent with the creation of elliptic flow on a partonic level before hadron formation. To extend

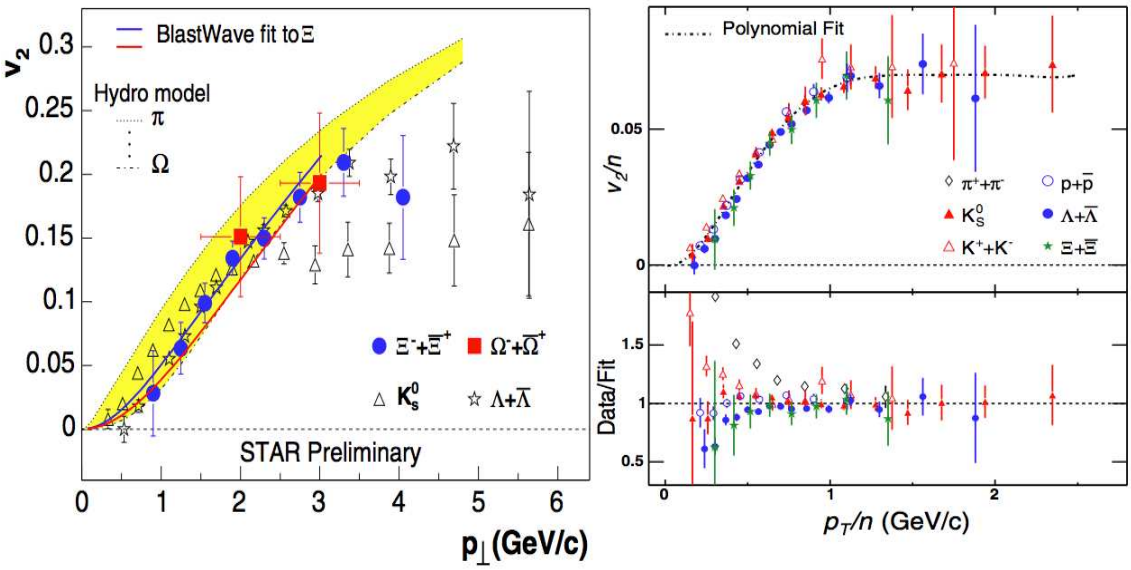

Figure 1.13: Elliptic flow measurement of multi-strange hadrons

this hypothesis further, the measured v_2 of the different particles is divided by the number of valence quarks, n, and plotted against p_T similarly scaled by the number of valence quarks. It shows an apparent scaling of the azimuthal anisotropy, revealing the development of anisotropy in the partonic stage of collision [29]. Figure 1.13 shows the elliptic flow results of multistrange hadrons from STAR. On the right plot, together with K^0_s, Λ and Ξ from STAR, data for pions, protons and charged kaons from PHENIX are also shown. The lower panel on the right represents the deviation from a fit to the data. With the exception of pions, the particles appear to scale very well. The low p_T/n region is dominated by hydrodynamics and there is some

deviation occurring in this region. The scaling is naturally reproduced in coalescence models where the elliptic flow is built up when the collision is in the deconfined state.

1.4.3 Strange Particle Production Enhancement

It was predicted that QGP formation is accompanied with a dramatic rise in the production of strange particles. As the centrality of the collision increases there is a jump in the strange particle yields versus the charged hadron yield [30][31]. Figure

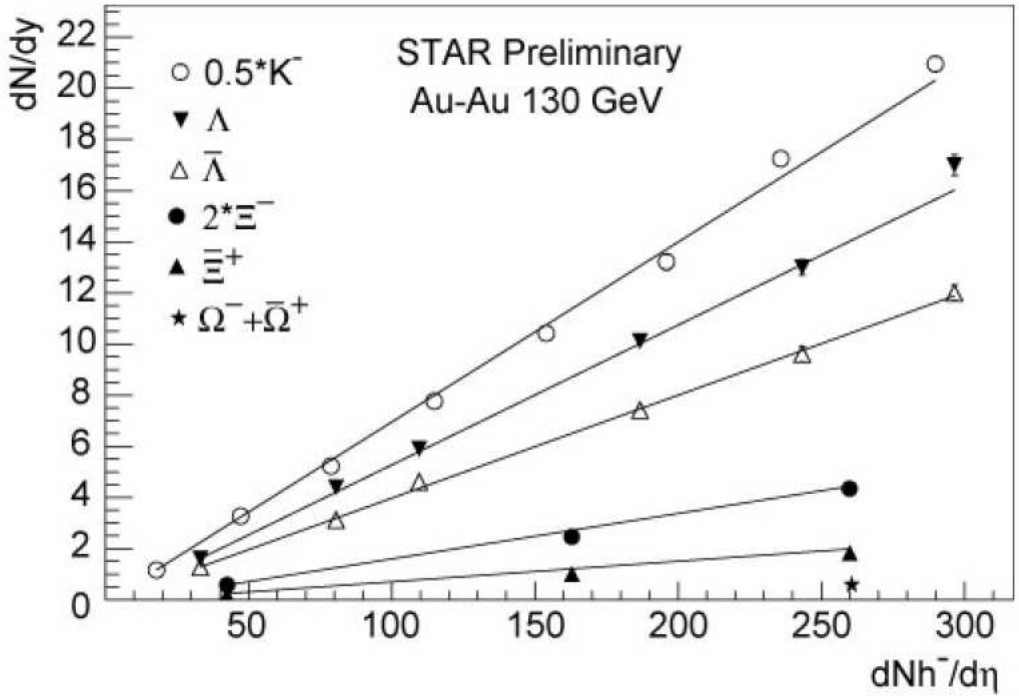

Figure 1.14: Strange Particle Production Enhancement

1.14 shows the STAR measurement of strange particle yield as a function of produced negative hadrons yield at mid-rapidity. All particles reveal a smooth increase in the yield. Kaons carry about 90% of the strange quarks produced in a collision, and hence the K/π ratio is often used as a tool to study the strangeness enhancement.

It has been observed that the K^-/π^- ratio rises smoothly with $\sqrt{s_{NN}}$ and K^+/π^- increases sharply at low energies reaching a maximum at $\sqrt{s_{NN}} \sim 10$ GeV before slowly dropping [32]. Comparison to p+p data at $\sqrt{s} = 130$ GeV shows a 50% increase in $\frac{(K^+ + K^-)}{2}$ compared to those of pions.

1.5 Significance of Charm Measurements

Partons traversing the dense QGP lose energy via gluon radiation with a magnitude that depends strongly on the gluon density of the medium ($E_{\text{loss}} \sim dN_g/dy$). Experiments at RHIC show a distinctive suppression of light quarks, which is evidence for the stopping power of the medium with high gluon density. Theoretical calculations predict the energy loss of charm quarks to be less compared to light quarks [22]. Open charm is measured through the reconstruction of its hadronic decay channels or semi-leptonic decay channels.

The hadronic decay channels are:

$$D^0(\bar{D}^0) \rightarrow K^-\pi^+(K^+\pi^-)(B.R.: 3.8\%), \tag{1.8}$$

$$D^{+/-} \rightarrow K\pi\pi(B.R.: 9.2\%). \tag{1.9}$$

The semi-leptonic decay channels are:

$$D^0 \rightarrow e^+ + X(B.R.: 6.9\%), \tag{1.10}$$

$$D^{+/-} \rightarrow e^{+/-} + X(B.R.: 17.2\%). \tag{1.11}$$

The interaction between a charm quark and the medium is reflected by the charm quark elliptic flow (v_2). It can tell us the degree to which charm quarks interact with

other partons, and then provide us with pivotal information on the early thermalization of light flavors. Since charm quarks are mostly produced from the initial fusion of partons, charm cross section in heavy-ion collisions should be scaled by the number of binary collisions [24]. In fact, STAR and PHENIX have observed that the centrality dependence of charm production is consistent with $N_{\rm bin}$ scaling [21]. Charm measurements can also serve as a powerful test for pQCD because of the large Q value (≥ 3 GeV/c) involved in charm production. The measurement of charm quark energy loss through non-photonic electrons resulted in new findings that were contrary to expectation. In the following sections, I will discuss (1) the energy loss of charm quarks in the medium and (2) charm quark collectivity measurements. The total charm cross-section measurements are important references for charmonium production, whose enhancement or suppression in central AuAu collisions is thought to be a robust signal of the QGP.

1.5.1 Charm Quark Energy Loss Puzzle

The radiative energy loss of charm quarks is predicted to be less than that of lighter quarks. This is because gluon radiation in the vacuum is modified by the mass of the parent quark: radiation for angles $\theta < \frac{M_q}{E_q}$ is suppressed, an effect known as the "dead-cone" effect [22]. When an energetic charm quark traverses through the dense medium, it interacts with surrounding partons and loses energy (manifested by suppression of nuclear modification factor, R_{AA}). But the dead-cone effect predicts that the suppression of R_{AA} for charm quarks in central nucleus-nucleus (A+A) collisions is smaller than that for light quarks. Numerical estimates indicate that the quenching of charm quarks may be approximately about half that of light quarks. However, measurement of R_{AA} through non-photonic channels by STAR and

PHENIX shows a suppression similar to light quarks as seen in Fig. 1.15 [21][38]. The dead-cone effect is especially true for the bottom quark due to its heavier mass. Since the non-photonic R_{AA} includes contributions from bottom and charm, the energy loss was expected to be even reduced when considering the bottom contributions.

Because of the mass of the heavy quarks, we can use perturbative calculations here. The comparison of data with the pQCD estimations illustrates that the suppression of electrons from charm decay may reach as low as that of light hadrons. This significant reduction at high p_T suggests sizable heavy quark energy loss.

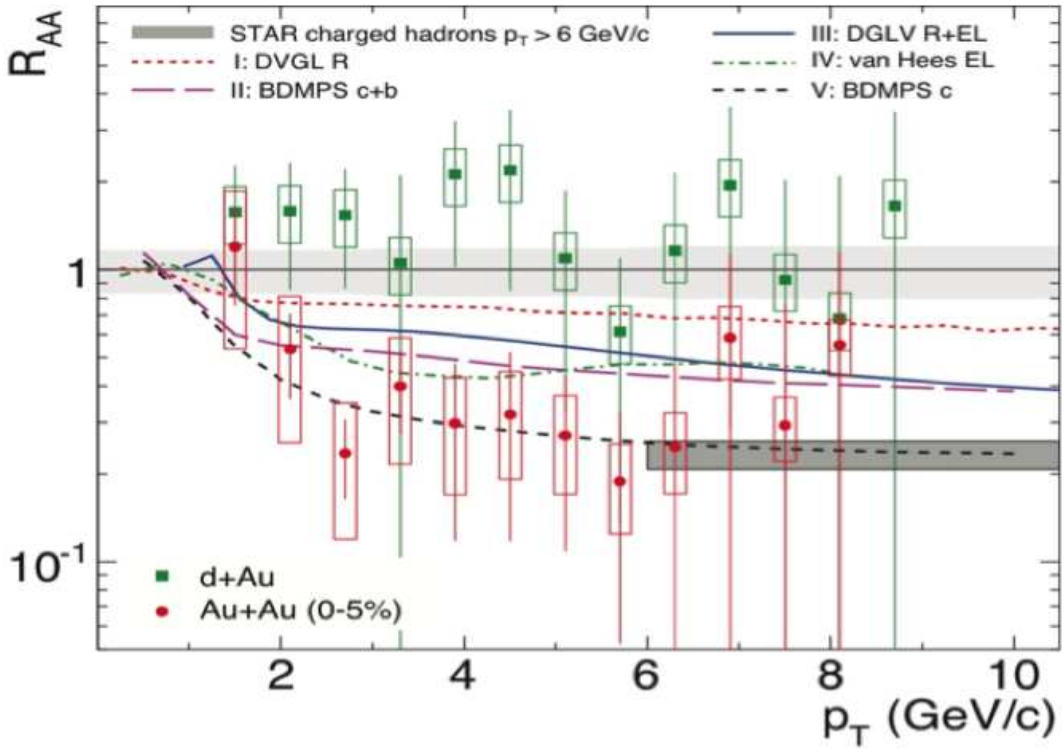

Figure 1.15: Measurements on non-photonic electron R_{AA}

Recent studies show that for a range of parameters relevant for RHIC, collisional energy loss also plays a significant role in addition to radiative energy loss, and that

they are comparable to each other [33-36]. If we consider that only the charm quark contributes to the non-photonic electron (NPE) distribution, it would explain the observed energy loss within present experimental and theoretical uncertainities. There are three important medium effects that control the radiative energy loss at RHIC: (i) Ter-Mikayelian effect [39], (ii) transition radiation [40] and (iii) energy loss due to interaction with the medium [41]. Gluon radiation is the most important energy loss mechanism due to interaction with the medium. Some authors argue that elastic collisional energy loss may play an important role[7] when a charm quark traverses the medium [42]. They computed R_{AA} in the hydrodynamic transport scenario, and it gives a strong suppression as observed. The theoretical calculations with charm+bottom energy loss can explain the data within uncertainities, by counting large elastic collisional energy loss. Further theoretical efforts in this direction are needed. If the data in Fig. 1.15 are confirmed, then, this will bring at least two open issues: (i) if the current radiative energy loss mechanism persists, there is not much room for the bottom's contribution in the non-photonic electron spectrum up to $p_T \sim$ 7 GeV/c. (ii) if the bottom's contribution is as given by generic pQCD predictions (the crossing point is $\sim$ 3-5 GeV/c), there must be other energy loss effects besides gluon radiation. To decouple this issue, one should precisely measure directly reconstructed open charm hadrons instead of electrons. The STAR experiment at RHIC has the capability to detect charm and can reconstruct open charm mesons through their hadronic decay channels. The single electron distributions are very sensitive to the rapidity window, and at high rapidity, non-perturbative effects may become important [43].

[7] Elastic collisional energy loss becomes important when $\beta\gamma \sim 1$

1.5.2 Charm Quark Elliptic Flow

Elliptic flow is interesting because it has no mass dependence, no flavor dependence and it scales with the number of constituent quarks (NCQ). Charm quark flow is extremely interesting because of the high mass of the c-quark (m = 1.5 GeV/c^2). How their final spectra deviate from the initial ones depends on their interactions in the initial partonic matter, and the mechanism that converts them to hadrons, as well as their subsequent interactions in the hadronic matter. Should the c-quarks flow, there must have been enough interactions to thermalize light quarks easily. Preliminary results from both STAR and PHENIX indicate a non-zero non-photonic electron v_2 [44][45]. Figure 1.16 shows the elliptic flow results of non-photonic electron measurement from the STAR and PHENIX collaborations as a function of transverse momentum. The left plot on Fig. 1.16 is the latest STAR measurement using the

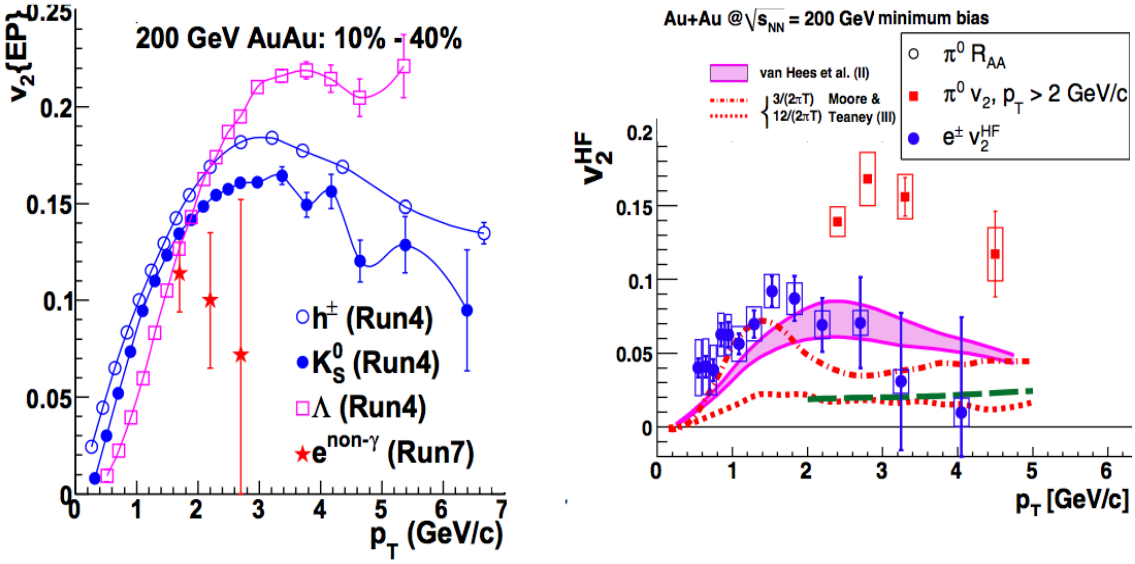

Figure 1.16: Results of non-photonic v_2 measured

azimuthal correlation of v_2 with the event plane [46]. With the large statistical

uncertainities, the non-photonic electron v_2 is found to be systematically lower than that of hadrons. The right plot is the measurement from PHENIX and the data points below 2 GeV/c favors large charm quark v_2. At p_T beyond 3 GeV/c, there are large uncertainties on the experimental data points and also contribution from bottom quark. There are uncertainties in the electron v_2 arising from the electron background due to γ-conversions and π^0-Dalitz decays. Shown in Fig. 1.17 are v_2 results obtained from the AMPT model. The AMPT model is a hybrid model that

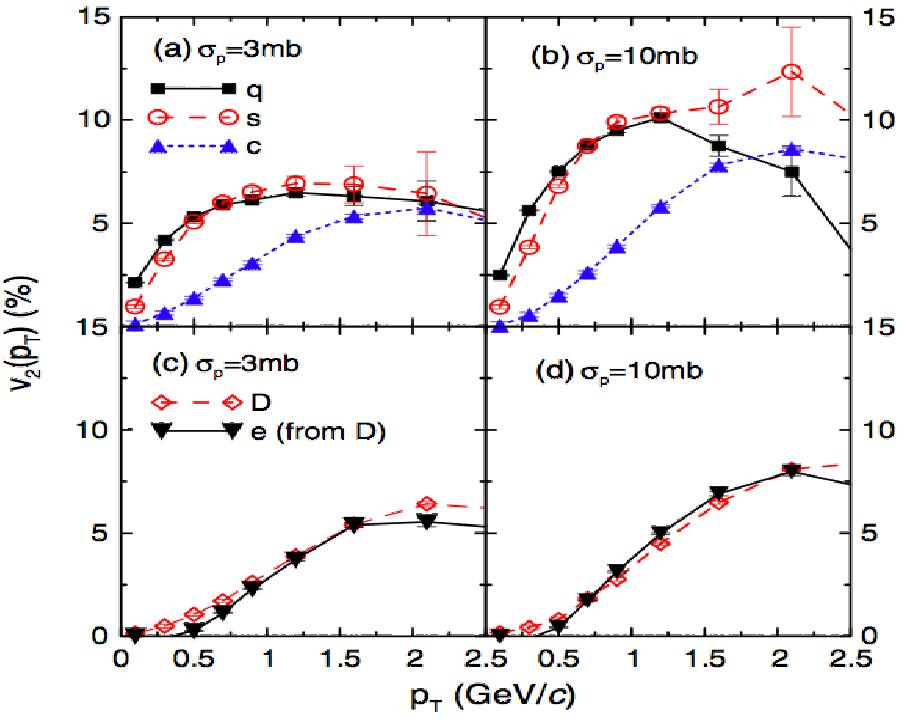

Figure 1.17: AMPT Model of the Elliptic Flow of Charm

uses minijet partons from hard processes and strings from soft processes in the heavy-ion jet interaction generator (HIJING) model as the initial conditions for modeling heavy-ion collisions at ultra-relativistic energies. From the lower panels of Fig. 1.17, it is seen that the D-meson elliptic flow follows closely the corresponding charm quark

elliptic flow shown in the upper panels, although they are slightly shifted to higher p_T and have slightly higher values relative to those of charm quarks in the upper panel. Also shown in the lower panels are elliptic flow of electrons from D-meson decays (solid triangles) and they also follow closely the corresponding D-meson ones [47]. The upper panels shows that the v_2 of charm quarks is smaller compared to the light quarks. Although RHIC results have helped us enormously to understand the strong interaction thermodynamics, there are some open issues to be solved in order to completely understand the physics of the hadron-QGP phase transition.

1.6 Planned Measurements in the Heavy Quark Sector

A significant complication of the heavy quark measurement through the semi-leptonic decay channel is that the relative yield of charm and bottom is highly uncertain. Estimates indicate that bottom decay leptons may dominate electrons from charm for $p_T > 3$ GeV/c in p+p collisions as seen in Fig. 1.18. Also, jet quenching further amplifies the bottom contribution to the lepton spectrum and it strongly limits the nuclear modification factor of electrons in Au+Au collisions [18]. As seen on the right panel of Fig. 1.18, even with extreme opacities, with gluon rapidity densities up to 3500, the smaller b-quark energy loss limits the nuclear modification factor, $R_{AA} \sim 0.5-0.6$. If the bottom contribution to the R_{AA} is what is given by the pQCD calculations, then there are other energy loss mechanisms we need to find out about. Further measurements of non-photonic electrons cannot solve this problem. We should make an unambiguous measurement of the open charm suppression by measuring D-mesons as a function of p_T in d-Au and Au-Au through direct methods. This would allow a complete reconstruction of the final state. It will shed light on the mechanism of energy loss and early thermalization.

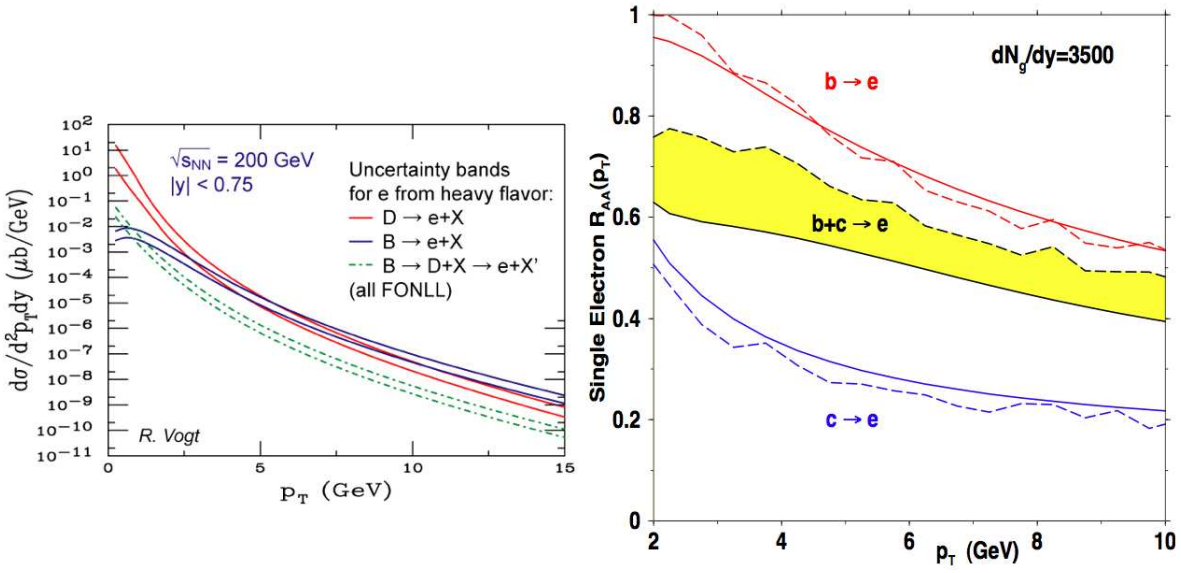

Figure 1.18: Estimate of the charm and bottom contributions to the NPE measurement, and their uncertainities.

The need for a precise direct reconstruction of open charm calls for upgrades to the existing detector systems. The $c\tau$ of charm is $\sim$ 123 μm and that of bottom is $\sim$ 400-500 μm. The resolution of existing silicon vertex detectors is $\sim$ 250μm in STAR. The Heavy Flavor Tracker (HFT) of STAR, is designed for charm measurement. HFT can measure neutral and charged particles that decay 100μm or less from the primary vertex. In addition, HFT will measure non-photonic electrons decaying from charm and bottom hadrons [49].

1.7 Structure of this Dissertation

In this dissertation, I present direct reconstruction of neutral D-mesons using a microvertexing method through the decay channel, $D^0(\bar{D}^0) \longrightarrow K^{\mp}\pi^{\pm}$ in the STAR experiment at RHIC using the 2007 Au+Au collisions at $\sqrt{s_{NN}}$=200 GeV. The method uses a kinematically constrained fit for secondary vertex reconstruction. The dataset

was collected with Silicon Drift and Silicon Strip detectors (vertex trackers) and their pointing capabilities are crucial for this analysis. Preliminary results from 24 million minimum bias Au+Au events at $\sqrt{s_{NN}}$ =200 GeV gives a neutral D-meson signal of significance $\sim 10\sigma$. The results also indicate a stable $\bar{D^0}/D^0$ ratio close to unity, indicating vanishing baryonic chemical potential (μ_B) at RHIC. The method developed here is baseline for analysis involving the future inner tracker upgrade of STAR, the Heavy Flavor Tracker (HFT). In the Chapter 2 I will discuss RHIC and STAR and the various subsystems of STAR. Chapter 3 is devoted to data analysis details including discussions of cut studies. This chapter also includes details about the secondary vertexing method we used. The final two chapters summarize the results obtained and provide relevant physics discussions.

Chapter 2

The Experiment

After a gestation period of about 17 years, RHIC, the Relativistic Heavy Ion Collider began its operation in 2000 and opened a new frontier in the nuclear physics research. The data taken at RHIC have enabled us to learn about the unexplored landscapes of matter under extreme energy densities. RHIC started operation with four detectors: BRAHMS, PHENIX, PHOBOS and STAR, out of which BRAHMS and PHOBOS are decommissioned now. This chapter is devoted to the design of RHIC and the various experiments in the RHIC complex. Special emphasis is given to the description of the STAR experiment. The various subsystems of STAR including the vertex detectors (SSD and SVT) will be discussed. The chapter concludes with details on the design of a future upgrade to STAR, the HFT (Heavy Flavor Tracker) to which the analysis technique developed and described in this dissertation is the baseline.

2.1 RHIC

The Relativistic Heavy Ion Collider (RHIC) at Brookhaven National Laboratory (BNL) is the first machine in the world capable of colliding heavy ions as heavy as gold at relativistic speeds. RHIC mainly uses gold ion beams, which are the nuclei of gold atoms whose electron cloud is fully stripped off. Gold is one of the heaviest common elements; its nucleus is densely packed with particles. At RHIC, two beams of ions travel in opposite directions around its 2.4-mile ring and they cross at six

intersections. RHIC construction began during 1991 and was completed in 1999. It started taking physics data in June 2000 using Au+Au beams at center of mass energy 130 GeV. It is designed to operate with high luminosity over a wide range of beam energy and with particle species ranging from polarized protons to heavy ions. It can handle asymmetric collisions (such as deuterons on gold). To date, RHIC has used p+p, d+Au, Cu+Cu and Au+Au beams for collisions with energies ranging from 7.7 GeV to 500 GeV for p+p collisions. It is the first facility to collide heavy ion beams. The top center of mass energy for heavy nuclei is 200 GeV per nucleon pair, which is about 10 times greater than the highest energy reached by previous fixed target experiments. By having two beams colliding at the center of mass, more energy is provided to the collision rather than the translation of the entire system. It is at these high energies that the predictions of QCD come into play. RHIC can deliver polarized

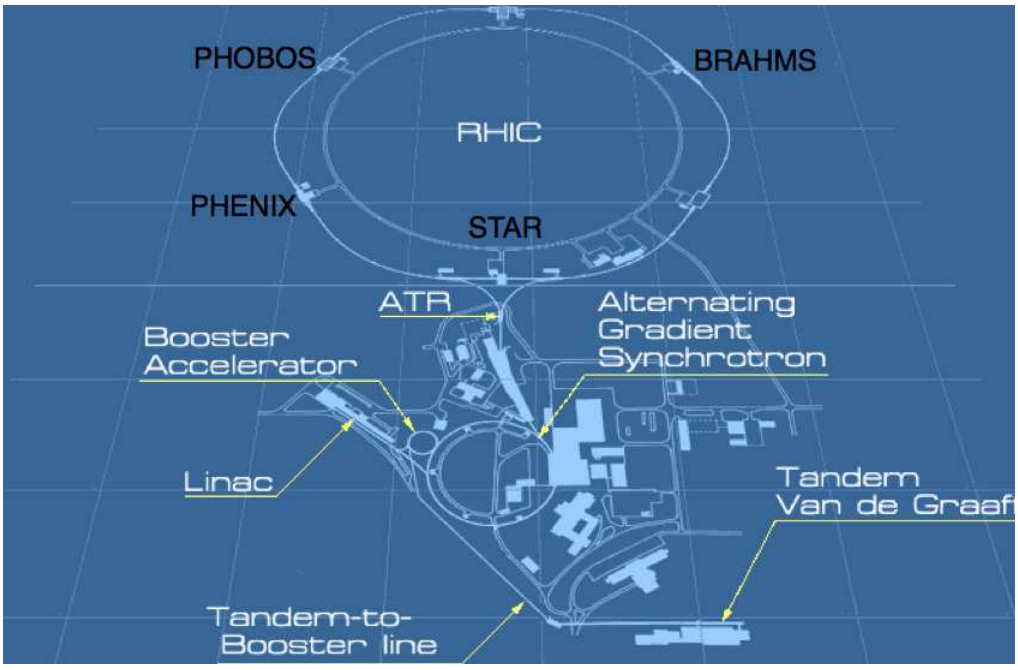

Figure 2.1: Overview of RHIC complex

proton beams of center of mass energy up to 500 GeV to carry out the proton spin program. The RHIC accelerator complex (Fig. 2.1) is made up of a Van de Graaff facility (TVDG), a linear proton accelerator, the booster synchrotron, Alternative Gradient Synchrotron (AGS) and the RHIC ring. For the Au beam, gold atoms are produced in the Pulsed Sputter Ion Source, located in the TVDG facility, where they are ionized to a charge of $-1e$. These negatively charged ions are accelerated through the Van de Graaff facility to about 1 MeV per nucleon. The ions are then passed through a thin sheet of gold foil, further ionizing the Au atoms to a net +32 e charge. The ions are then injected into the booster synchrotron and accelerated to an energy of 95 MeV per nucleon. After exiting from the booster synchrotron, they are further stripped to a net +77 e charge and transferred into the AGS, where they are accelerated to 8.86 GeV per nucleon and stored into four final bunches. Finally the ions are injected into RHIC and are stripped to bare charge +79 e during the transfer. The procedure is similar for Cu+Cu beams. However, in the case of p+p, protons are injected from the 200 MeV Linac into the booster, followed by acceleration in the AGS and injected into the RHIC ring [50].

RHIC has two beam lines in which ions travel in opposite directions and they intersect at six locations. The detectors are located at these intersections. The two larger detectors are, STAR and PHENIX, which are detectors of quite different and complementary designs. STAR focuses on large solid angle detection of hadrons, while PHENIX is designed for detection of leptons and photons as well as hadrons over limited ranges of solid angle. Two smaller detectors, PHOBOS and BRAHMS, were also approved and mounted with a relatively short construction period. STAR

and PHENIX are currently operating but PHOBOS and BRAHMS finished data taking and their detectors were decommissioned. STAR is at the six o' clock position (see Fig. 2.1). RHIC can collide beams of spin polarized protons using the helical dipoles (Siberian snakes and spin rotators, which allow acceleration and storage of protons with both longitudinal and transverse spin polarization at the collision points). RHIC uses radio Frequency (RF) cavities and collimators to improve the beam quality further. These RF cavities create sinusoidal electric fields with the phase set to accelerate both the beams and to maintain bunches. It operates at 28.15 MHz and accelerates the beams to their final collision energy. There are 1740 superconducting magnets that are used to steer the ion beams around the ring.

2.1.1 The BRAHMS Detector

The BRAHMS (Broad Range Hadron Magnetic Spectrometer) experiment was designed to measure charged hadrons over a large range of rapidity and transverse momentum. It covers the widest possible range in polar angle relative to the beam direction with good particle identification (PID). As we approach the more forward angles, the lab momenta of particles increases to 25-30GeV/c around 2° compared to a few hundred MeV/c around 90° [51] . Here we shall use two variables to describe the phase space of the observed particles: Transverse momentum (p_T) and rapidity (y)[1] (see page.86).

A perspective view of the BRAHMS detector is shown in Fig. 2.2 The Forward Spectrometer (FS) is positioned to the right of, and near the beam pipe at 2.3° and the Mid-Rapidity Spectrometer (MRS) is positioned to the left of the beam pipe near 90°

[1]At relativistic energies, it is customary to use kinematic variables that have simple properties under Lorentz transformation along the beam direction rather than polar angle and momentum.

from the perspective of beam particles travelling around RHIC ring in the clockwise direction. The rapidity coverage of the entire spectrometer is from $y \approx 0$ to $y \approx 4$.

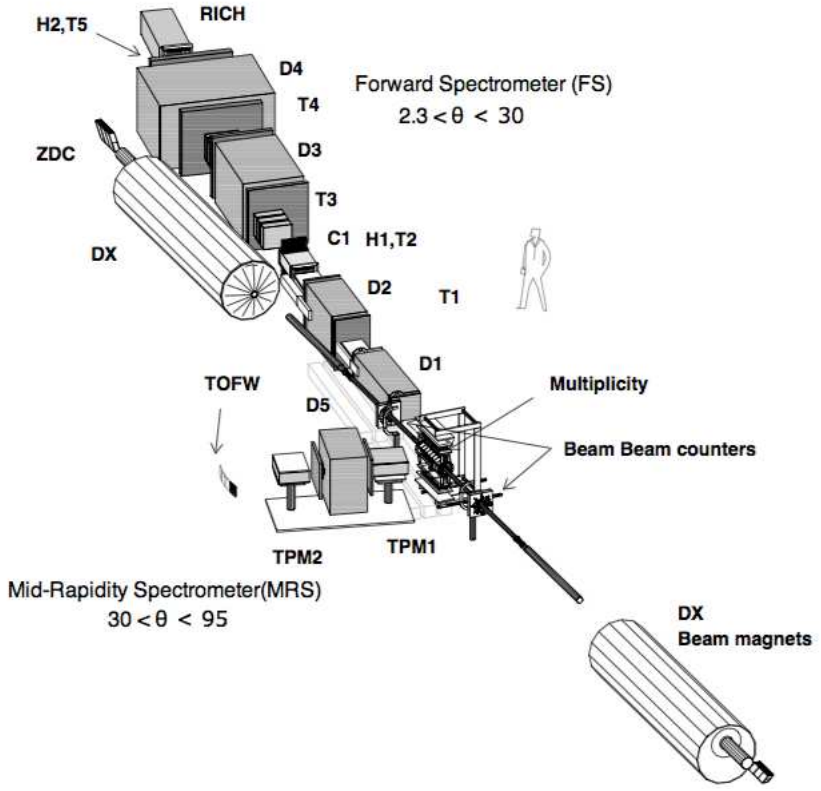

Figure 2.2: Perspective view of the BRAHMS experiment

The other RHIC experiments are limited to $|y| < 2$ for particle spectroscopy with good PID. The particle identification (PID) is achieved with time of flight (TOF), threshold and ring-imaging Cherenkov detectors and tracking devices like Drift Chamber (DC) and Time-Projection Chamber (TPC).

2.1.2 The PHOBOS Detector

The PHOBOS experiment is capable of detecting charged particles over the full solid angle using a multiplicity detector and measuring identified charged particles

near mid-rapidity ($|y| < 0.5$) in two spectrometer arms with opposite magnetic fields. Detection of charged particles with very low transverse momentum is the unique fea-

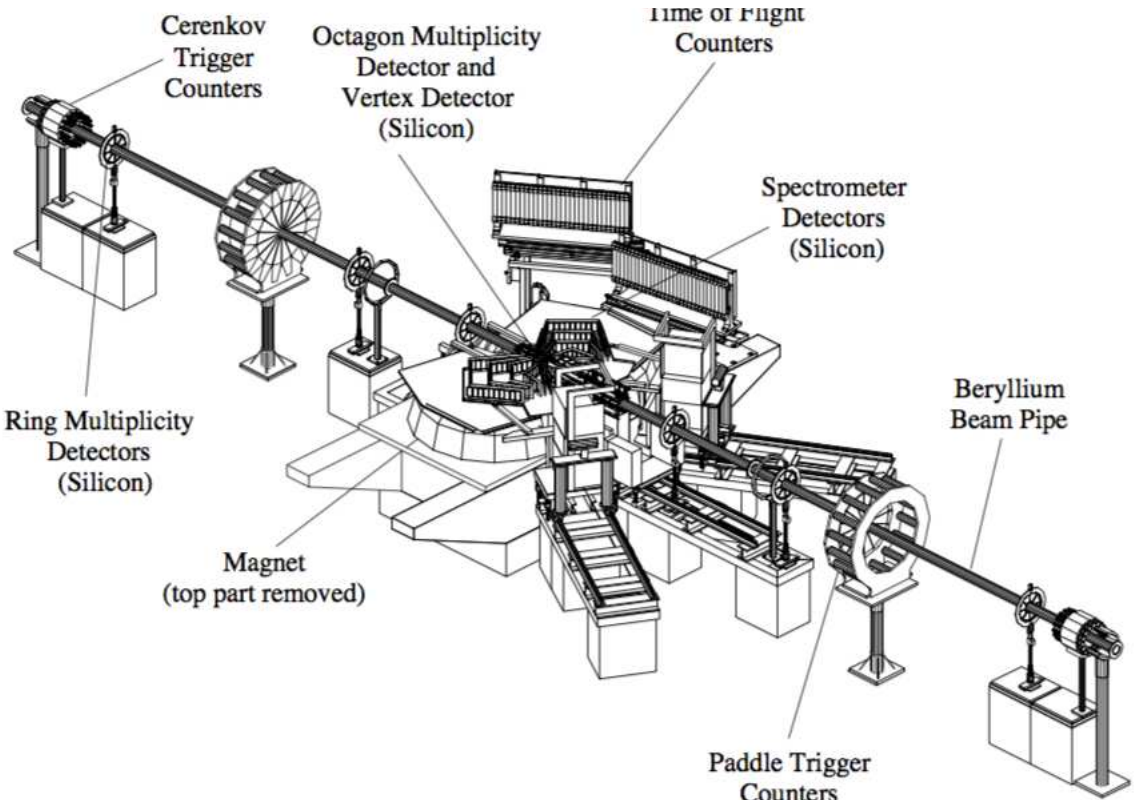

Figure 2.3: Schematic layout of the PHOBOS detector

ture of the PHOBOS experiment. This is achieved by minimizing the of material between the collision vertex and the first layers of silicon detectors. Silicon pad layers are used for charged particle detection. The PHOBOS detector has four subsystems: a multiplicity array, a vertex detector, a two-arm magnetic spectrometer including a TOF wall and several trigger detectors, which also determine the centrality of collisions. Shown in Fig. 2.3 is a schematic layout of the PHOBOS detector. The PHOBOS detector can measure the multiplicity of charged particles over the pseudo-rapidity interval $-5.4 < \eta < 5.4$. The array of silicon pad detectors in an octagonal

barrel geometry covers the mid-rapidity region $|\eta| < 3.2$. It is complemented by six ring detectors that extend the pseudorapidity range to $|\eta| < 5.4$ [52].

2.1.3 The PHENIX Detector

The PHENIX (Pioneering High ENergy Interaction eXperiment) detector is designed specifically to measure electrons, muons and protons, which are considered as direct probes of the collisions. Three large steel magnets produce high magnetic fields

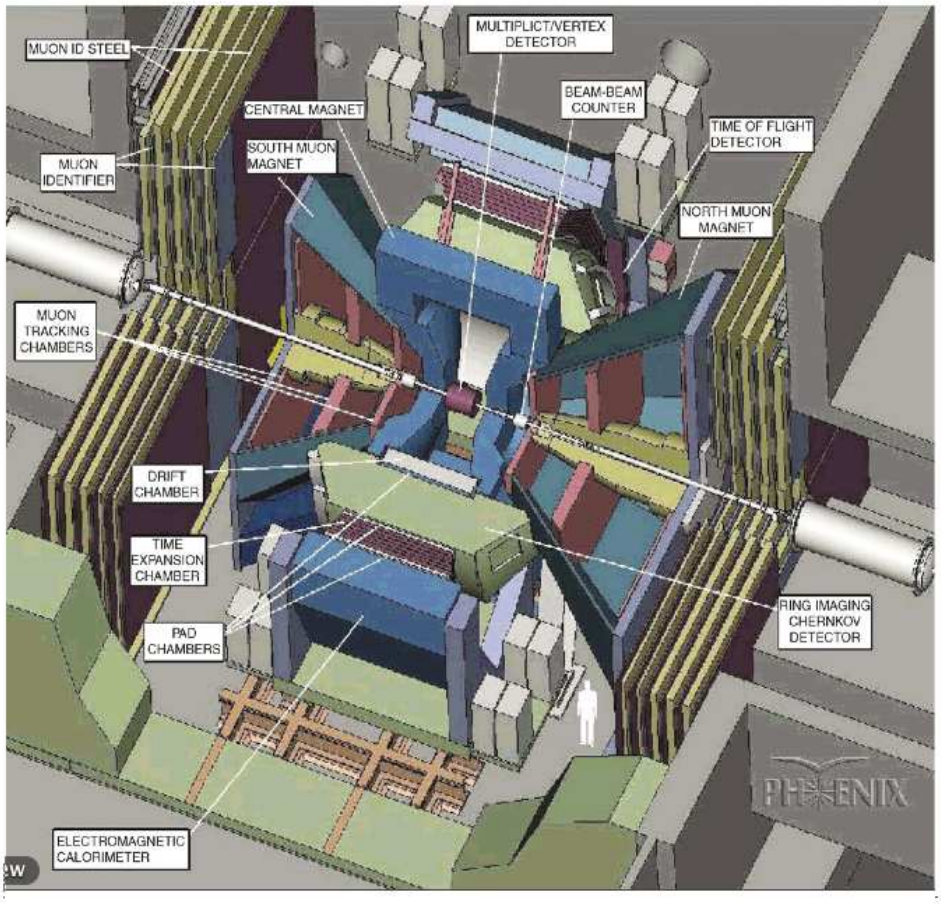

Figure 2.4: Cutaway view of the PHENIX detector detector.

to bend charged particles along curved paths. PHENIX has a dozen detector subsystems. These subsystems are part of Central Arm Detectors, Muon arm Detectors and Event Characterization Detectors. The tracking chambers record hits along the flight path to measure the curvature and thus determine each particle's momentum. Other detectors identify the particle type and or measure the particle's energy. Event characterization detectors determine the centrality of each collision.

The PHENIX tracking system consists of drift chambers (DC), pad chambers (PC) and the time expansion chamber (TEC). These units link the track segments that traverse the RICH (ring-imaging cherenkov) and extend to the electromagnetic Calorimeter (EMCal). The drift chambers measure charged particle trajectories in the $r-\phi$ direction to determine p_T of the particles and the invariant mass of particle pairs. The pad chambers perform 3D spatial point measurements. The TEC tracks particles passing through the region between the RICH and the EMCal. Particle identification is done through RICH and TOF systems in the central arm. The EMCal is used to measure the spatial coordinates and energy of electrons and photons produced in heavy ion collisions. The PHENIX Muon Arms detect muons at rapidities $1.2 < |y| < 2.2$ with full azimuthal acceptance. The timing, location and particle multiplicity of a PHENIX collision are determined by the Beam-Beam Counters (BBC), the Multiplicity/Vertex Detector (MVD) and the Zero-Degree Calorimeters (ZDC). The BBCs provide both the time of interaction and position of a collision. The MVD provides a measure of event particle multiplicity, collision vertex position and fluctuations in charged particle distributions. The ZDCs provide information on the most grazing collisions [53].

2.2 The STAR Detector

The STAR (Solenoidal Tracker At RHIC) detector is one of two large detector systems constructed at RHIC at BNL. STAR was constructed primarily to study the behavior of strongly interacting matter at high energy density and also to look for the production of Quark-Gluon Plasma (QGP). The STAR collaboration consists of 562 collaborators from 55 institutions in 12 countries. In RHIC collisions, a huge number of particles is produced (approximately 1000 per unit pseudorapidity). The average transverse momentum per particle is about 500 MeV. STAR measures many

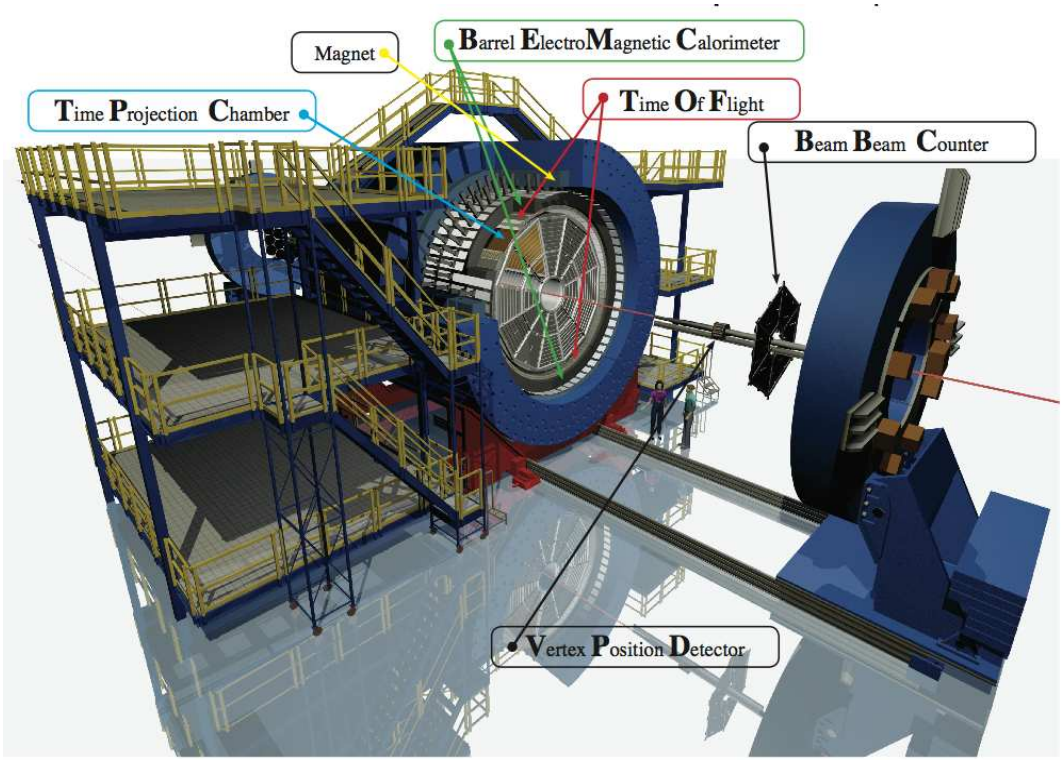

Figure 2.5: Layout of STAR Experiment

observables simultaneously to look for signatures of the QGP phase transition and to understand the space-time evolution of the collision process. Shown in Fig. 2.5

is a schematic of the STAR detector. The STAR experiment has excellent capacity to measure hadron production over large solid angles. The large acceptance of STAR makes it particularly well suited for event-by-event charactarizations of heavy ion collisions and for the detection of hadron jets. It has various detector systems for precise tracking, momentum analysis and particle identification at center-of-mass rapidity. Momentum measurements are made at midrapidity over a large pseudo-rapidity range ($|\eta| < 2$) with full azimuthal coverage. The centerpiece of STAR is the

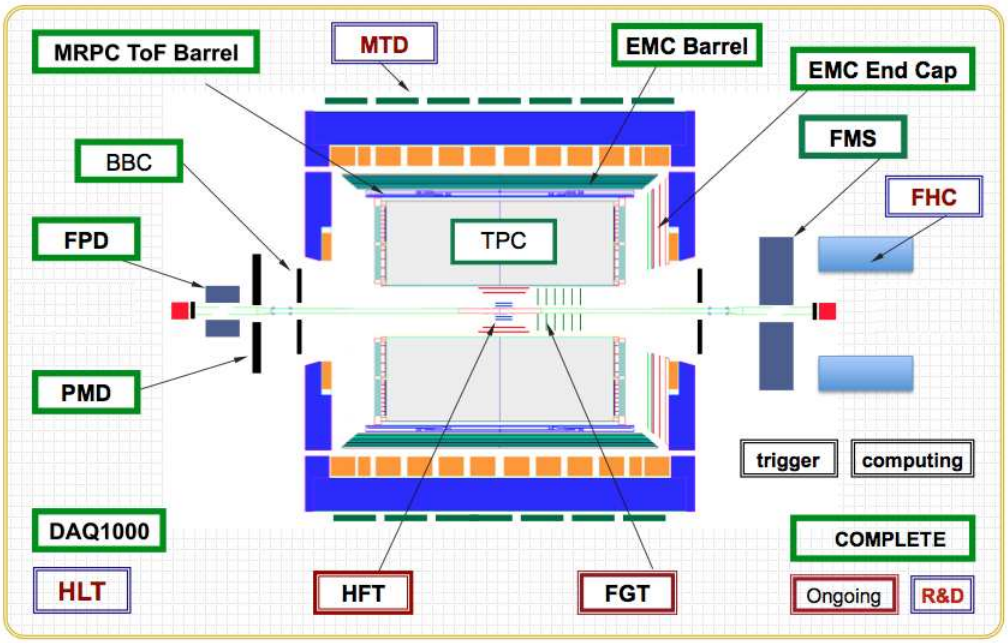

Figure 2.6: STAR detector subsystems

large TPC (Time Projection Chamber). In this analysis, besides TPC, we mainly use the Silicon Vertex Tracker (SVT), for particle tracking close to the interaction region and a Silicon Strip Detector (SSD), for extrapolating the TPC tracks through SVT hits. These detectors and their role will be discussed in detail in the next sections.

Figure 2.6 shows the various subsystems of STAR. The development of some of them is still ongoing.

2.2.1 Time Projection Chamber (TPC)

The TPC is the central element among the detectors that surround the interaction vertex in STAR. The TPC provides complete coverage around the beam line, and provides complete tracking for charged particles within ± 1.8 units of pseudo-rapidity at the center-of-mass frame. Its range of coordinates covers -210 cm $< z <$ 210 cm, 50 cm $< r <$ 200 cm and $0 < \phi < 2\pi$, making it the largest TPC in the world [54] until the ALICE TPC was built in 2010. It is divided into two halves by a central membrane at $z = 0$ with the electric fields in each half pointing in opposite directions. The TPC records an image of all charged particle tracks passing through the detector. Charged particles with momenta greater than 100 MeV can be recorded. In addition to the primary particles, each collision produces a high flux of secondary particles due to the interaction of primary particles with the material in the detector and the decay of the short lived primary particles. These secondary particles also need to be tracked and identified. The TPC can handle multiplicities reaching up to 3000 tracks per event [54]. A schematic representation of the STAR TPC is shown in Fig. 2.7.

The TPC is the primary tracking device of STAR; it identifies particles by measuring their ionization energy loss (dE/dx). The TPC is filled with P10 gas (10% methane, 90% argon) regulated at 2 mbar above atmospheric pressure. A charged particle traveling through the detector ionizes the gas along its trajectory. The primary attribute of P10 gas is the fast drift velocity, which peaks at a low electric field. Operating on the peak of the velocity curve makes the drift velocity stable and insensitive to small variations in temperature and pressure. The TPC records the

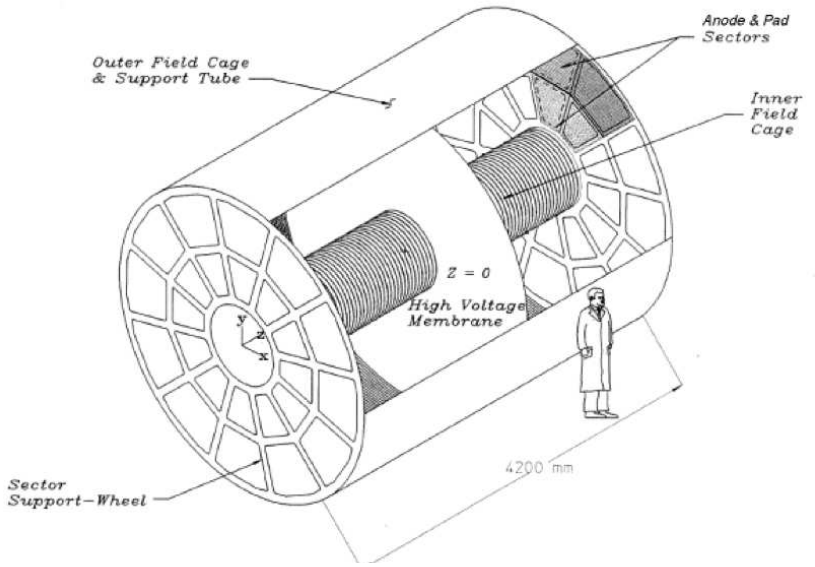

Figure 2.7: Schematic representation of the STAR TPC

tracks of particles and measures their momenta. Particles are identified over a momentum range from 100MeV/c to greater than 1 GeV/c, and momenta are measured over a range of 100 MeV/c to 30 GeV/c. The TPC sits in a homogeneous magnetic field along the z-axis generated by a large solenoidal magnet operating at 0.5 T. The central membrane, the end caps and the inner and outer cylinder of the TPC form an electrostatic field cage and it maintains a well-defined, uniform electric field of $\sim$ 135 V/cm between the high voltage membrane at the center of the TPC and each endcap. Consequently the E-field and the B field are parallel inside the TPC. The central membrane is operated at 28 kV. The end caps are at ground potential. The field cage cylinders provide a series of equipotential rings that divide the space between the central membrane and the anode planes into 182 equally spaced segments. The central ring is common to both ends and it is attached to the central membrane. The path of primary ionizing particles passing through the gas volume are reconstructed

with high precision from the released secondary electrons drifting to the end caps at the ends of the chamber. The uniform electric field maintained inside the TPC drifts the secondary electrons coming from the primary tracks to the anode endcap. Diffusion of the drifting electrons and their limited number defines the position resolution. Ionization fluctuations and finite track length limit the dE/dx particle identification. The anode endcaps are organized into 12 inner and outer sectors as can be seen from Fig. 2.7. The readout section consists of three layers: the gating grid, the Frisch grid and the anode grid. Figure 2.8 represents the electron drift and signal amplification in the TPC endcap. The gating grid is transparent to the drift of electrons while

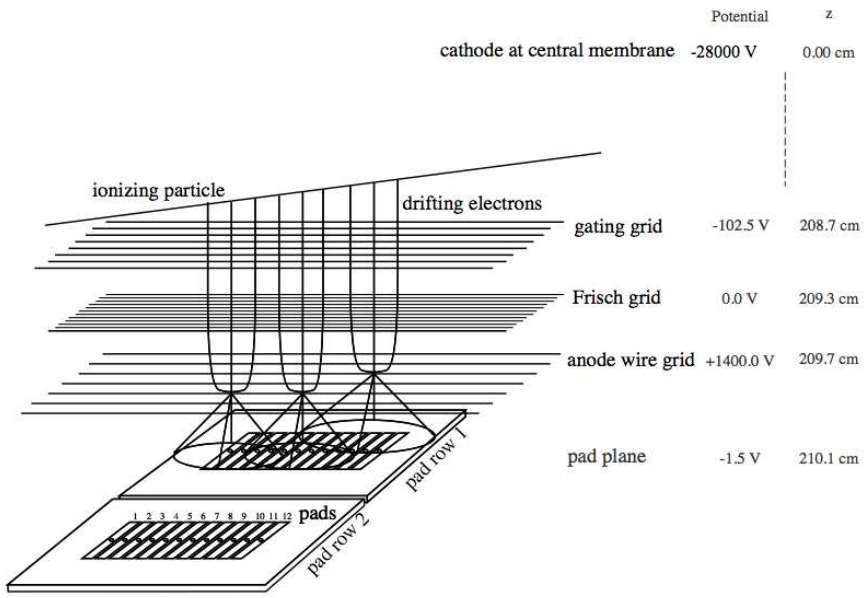

Figure 2.8: Principle of electron drift and signal amplification in TPC

an event is being read out. After read out, it closes to prevent the drift of positive ions from the amplification region into the TPC drift volume. The Frisch grid separates the homogeneous drift field from the strongly inhomogeneous amplification field

surrounding the anode wires. The strong inhomogeneous electric field around the anode wires accelerates electrons and generates an electron avalanche. In this way, the signal is amplified several thousand times while still being proportional to the initial number of drifting electrons.

The charged tracks induce a signal in the cylindrical pad rows surrounding the beam pipe. The pads are positioned approximately perpendicular to the tracks. The hit information from adjacent pads is used to determine the two-dimensional point where the particle ionized the gas. The third coordinate is determined from the drift time of the electron cloud. The drift velocity of ~ 5.4 cm/μs and the sampling rate of $\sim$10 MHz divide the maximum drift length of 2.09 m into 512 time buckets. The read-out electronics assigns a 10-bit ADC value, proportional to the charge deposited in each time bucket. The resulting pixel image of the TPC constitutes the raw data, which is further processed afterwards.

The pad plane is divided into inner and outer sectors for optimized momentum and dE/dx resolution, as shown in Fig. 2.9. The inner subsector is optimized for good two-track resolution. The inner pads are small and they are widely separated to reduce the electronic channels. The track density is smaller in the outer sectors. Here the pads are densely packed in order to improve dE/dx resolution.

The process of reconstructing the three-dimensional positions of ionization points during the offline analysis is called cluster finding. The cluster-finding algorithm is applied to the TPC raw data. For each ionization point, the three-dimensional coordinate and the total amount of charge is determined. To achieve better spatial resolution without an exceedingly high number of electronic channels, the pads should be approximately of the size of a typical electron cloud. After all ionization points

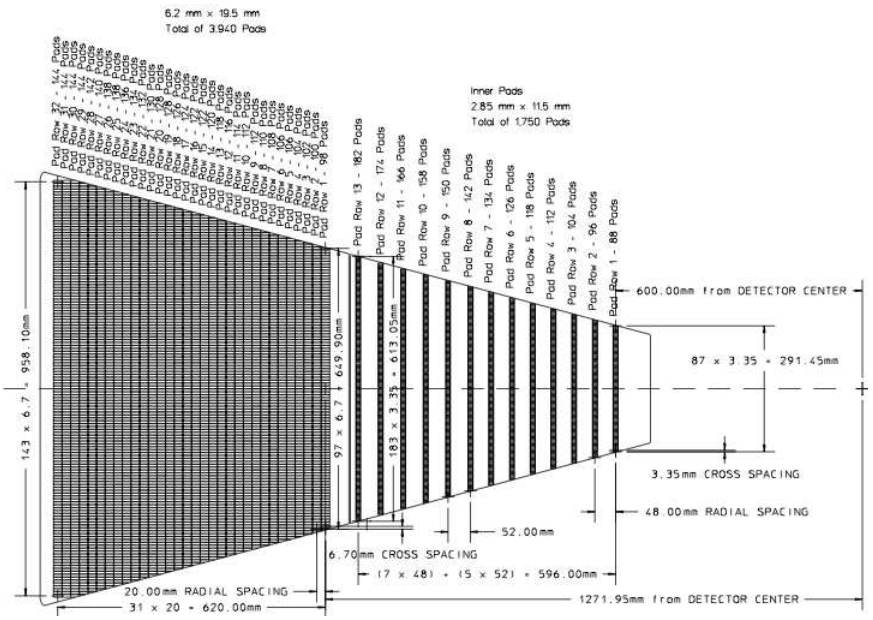

Figure 2.9: Pad plane layout of the TPC sectors.

are localized by the cluster finder, a tracking algorithm is applied to reconstruct the particle trajectory.

2.2.2 Forward Time Projection Chamber (FTPC)

Two cylindrical forward TPC detectors (FTPC) were constructed to extend the acceptance of the STAR experiment. They cover the pseudorapidity range $2.5 < |\eta| < 4.0$ and measure momenta and production rates of positively and negatively charged particles as well as neutral strange particles. The increased acceptance improves the general event characterization in STAR and allows the study of asymmetric systems like p+A collisions[55].

2.2.3 Laser System for the STAR TPC

Experiments with accelerators of high-energy heavy ion beams, where particle multiplicity could reach 2000-5000 and has high fluxes of tracks per unit time, will have distortions due to charge accumulation in the sensitive volume. In order to monitor these distortions laser tracks are required[2]. To determine spatial distortions, calibrate and monitor the TPC, a laser calibration system has been built. Repeated measurements of narrow ultraviolet laser beams, which create straight tracks, provide precise calibration. Laser tracks have no multiple scattering and are not sensitive to magnetic fields.

The physics goals of STAR impose a 10% momentum resolution for a particle with a p_T of 10 GeV/c. The errors on the z (drift) -coordinate must be well under 1 mm. The following are some sources of uncertainty in track coordinate measurements.

(1) Variation in drift velocity caused by gas mixture, temperature, pressure and electric field variation.

(2) TPC misalignment in the magnet and existence of the global $E \times B$ effect.

(3) Radial inhomogenities of magnetic and electric field.

(4) Space charge buildup due to high multiplicity in Au+Au collisions.

(5) TPC endcap wheel displacement and inclination.

In order to see all spatial variations throughout the TPC volume, the STAR laser system requires $\sim$ 100-400 laser tracks in each half of the TPC and laser beams should populate the TPC volume uniformly. Electron density along the laser beam at any point is required to be higher than ionization from relativistic particles. Laser beams

[2]A very high luminosity and low multiplicity reduces the distortion

should provide $\sim 0.01\%$ accuracy in drift velocity measurements. This requires synchronization of the time laser beams appear in the TPC volume to the RHIC clock within ~ 5 ns [56].

The laser calibration system constructed uses a novel design of small mirror bundles to produce a large number of narrow laser beams by splitting a wide laser beam. These beams produces straight tracks to monitor and correct TPC spatial distortions at the 200 μm level. This new approach is significantly simpler and provides higher TPC coverage at less cost. This system was expanded to calibrate and monitor Forward Time Projection Chambers.

2.2.4 STAR Magnet System

The charged particle tracks passing through the detector consist of finely spaced ionization clusters that drift under nearly uniform electric field to planes of electronics located at each end of the cylinder. The accuracy of the space point reconstruction from which the particle's momenta and trajectories are determined, depends on a detailed knowledge of the electric and magnetic fields. Homogeneity of field restriction comes from the momentum measurements of high-energy electron tracks that are nearly straight and also for position reconstruction accuracy, which depends on uncertainties in the field. There is a uniform magnetic field of $\pm$ 0.5 Tesla inside the TPC parallel to the beam line, generated by the solenoidal magnets surrounding the TPC.

2.2.5 Silicon Vertex Tracker (SVT)

In order to enhance the physics capabilities of the STAR TPC, a microvertex detector Silicon Vertex Tracker (SVT) is placed inside the TPC around the beam line.

It improves the primary vertexing, the two-track separation resolution and the dE/dx measurement for particle identification. It enables the reconstruction of very short lived particles, primarily strange and multi-strange baryons and D mesons through secondary vertexing close to the interaction region[3]. It also expands the acceptance for the low momentum primary tracks that do not reach the active volume of the TPC due to the applied magnetic field. Information from the SVT is advantageous both in high and low multiplicity environments; in the low multiplicity case, it can be an efficient primary vertex finder, and can rectify for the problem arising due to the wide distribution of collision vertices along the beam direction. On the other hand, the highly pixelated nature of the SVT ensures good two-track resolution in high multiplicity Au-Au events.

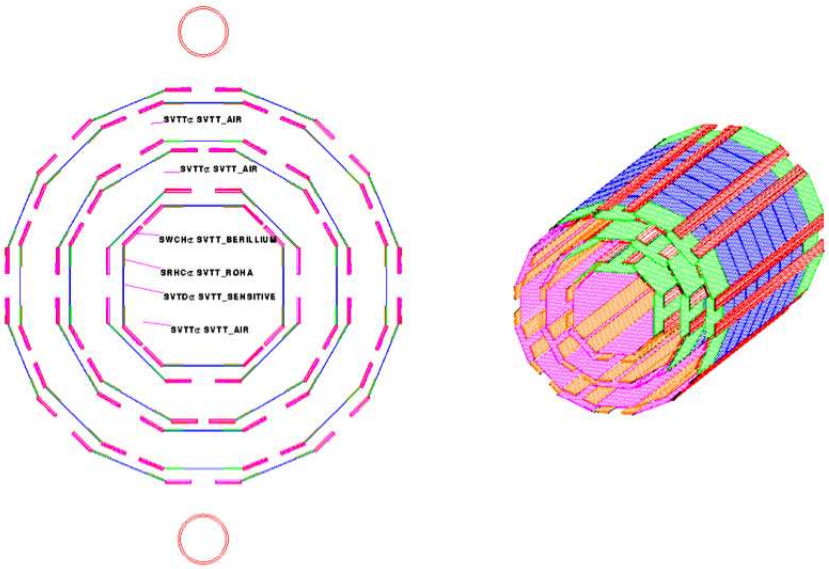

Figure 2.10: SVT detector configuration

[3]Historically, the SVT was designed for strange particle physics

The STAR SVT is based upon Silicon Drift Detector (SDD) technology. The SVT consists of three concentric barrels around the beam interaction region at radii of approximately 6.9, 10.8 and 14.5cm as shown in Fig. 2.10. These three barrels consist of eight, 12 and 16 ladders, respectively. Ladders are structures used to support the SDDs of the SVT. Each ladder is comprised of four, six and seven wafers respectively in each of the three barrels. The active silicon length in the beam direction is 25.2 cm for the inner barrel, 37.8 cm for the middle barrel and 44.4 cm for the outer barrel. The whole detector consists of 216 wafers arranged on 36 ladders to give complete azimuthal coverage in $|\eta| < 1$. The total average radiation length of the SVT is a little below 6% for all three layers or 1.89% per layer.

A silicon drift detector (SDD) may be envisioned as a solid-state time projection chamber. It is a charged particle position measuring device with a position resolution of 20 μm in each coordinate. The SDDs are made of highly homogeneous neutron transmutation doped (NTD) 4-inch n-type silicon wafers. Each SDD has a thickness of 280 μm and are 63 mm $\times$ 63 mm. It consists of a drift region and a focussing region. A charged particle crossing the detector creates electron-hole pairs. The holes are immediately absorbed by cathodes on the surface of the detector. Electrons converge to the middle of the bulk and drift at a constant speed under the influence of an applied uniform electric field towards the readout anodes. The current signal is then read through appropriate preamplifier electronics. The hit anodes determine the y coordinate and the drift time from the initial particle hit to read-out of the signal determines the x coordinate. The SVT consists of two half-detectors separated by the dividing central cathode that receives the maximum voltage bias. Electrons in the half detectors drift in opposite directions from one another. This design limits the

maximum drift voltage by limiting the maximum drift distance. The SDD's response is sensitive to certain environmental conditions such as the drift electrical field, the temperature, and the external magnetic field. The challenge is maintaining a highly linear drift velocity across the detector, which depends on the above said quantities. Typical position resolution values obtained across the detector are 2 and 25μm in the anode and drift directions, respectively. In addition to the position measurement the detector also yields an energy loss measurement on the basis of charged particle energy loss in each layer. It is estimated that the dE/dx resolution of the SVT is about 7%. Figure 2.11 shows the final SVT before installation of the second half shell.

Figure 2.11: The half SVT on the cone support structure, just before installation of the second half-shell

Each ladder of the SVT is mounted in two edge locations onto the SVT beryllium end rings. It enhances the tracking capabilities of the STAR experiment by accurately measuring the two-dimensional hit position and energy loss of charged particles [58]. The full SVT was completed and was installed in STAR during the 2001 run. It is now retired from STAR and will be replaced by the vertex detector upgrade HFT (Heavy Flavor Tracker).

2.2.6 Alignment and calibration of the SVT

The need for a direct charm meson measurement put stringent requirements on alignment and calibration of the SVT. This is because the initial design goal of the SVT was to reconstruct secondary vertices from multi-strange particles with higher $c\tau$ values and not the short $c\tau$ D decays. This, combined with a tracking environment of thousands of 'background' tracks, makes the task difficult. The multiple Coulomb scattering (MCS) of tracks from the detector layers limits the goals of the alignment and calibration efforts, but the combined uncertainties should be kept to a minimum.

This calibration involved a silicon strip detector (SSD) (a fourth layer of silicon detector, discussed in the next section) in the alignment. The goal is to reduce backgrounds to enhance the charm signal by a factor of $\sim$ 3-5, compared to the $\sim 4\sigma$ D^0 signal observed in Run 5 (Cu+Cu) with initial recalibration and alignment. The pointing accuracies are used as the figure of merit. These accuracies are reported as distance of closest approach (DCA) resolutions. The reconstruction process involves extrapolation of track candidates towards the event vertex. The distance of tracks from the collision vertex at the point of their closest approach is termed DCA. Thus to realize the physics goals, detector resolutions (including alignment) should achieve $\sigma_{\mathrm{DCA}_{XY}} < 80\mu$m (transverse) and $\sigma_{\mathrm{DCA}_{Z}} < 80\mu$m (longitudinal) at 1GeV/c.

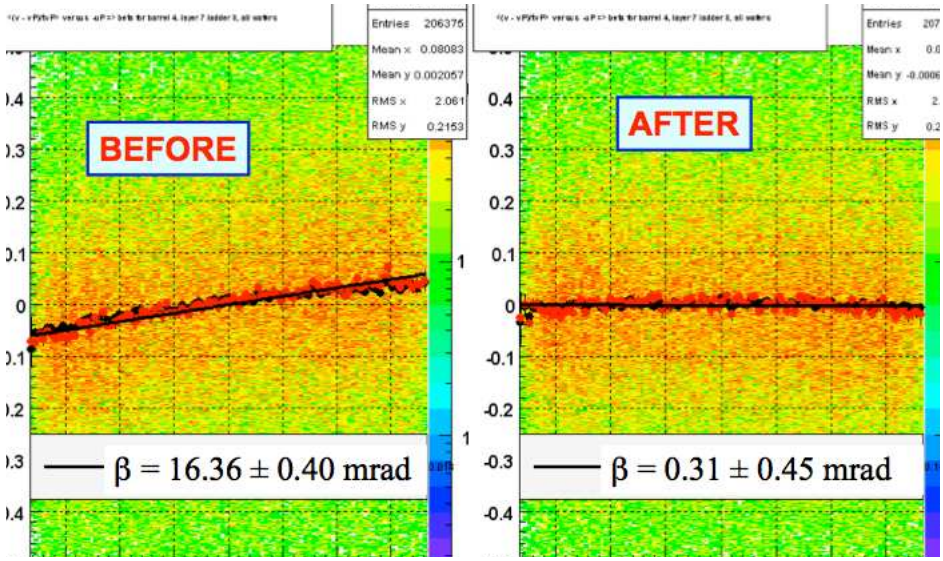

Figure 2.12: An example of alignment correction

The procedure involves: (1) global alignment, (2) SVT drift velocity calibration and (3) SVT self alignment. During the global alignment step, first the SSD sectors were aligned using TPC track information only, i.e., the SSD/SVT hit information on the track was not included. An iterative, global parameter minimization approach was used. After the SSD sectors and SVT shells were positioned inside the TPC track footprint, fine tuning of the individual SSD ladder positions was performed. After this step, the SSD geometry was frozen and the combined tracking of both TPC+SSD was used to fine tune the SVT ladders in the non-drifting z-direction and also to calibrate the SVT drift velocities. At the end, the SVT ladders were retuned using the whole tracking information (TPC+SSD+SVT). Only primary tracks were used throughout this alignment process. The SVT and SSD hit uncertainities after this calibration/alignment procedure were estimated using a hit pull analysis on track fits: the spatial resolution was determined by the requirement that the standard deviation

of pulls should be equal to one. The results were also averaged over three data samples from STAR during Run 5 Cu+Cu collisions. The results demonstrate an SVT resolution of $\sigma_{\rho\phi} = 49 \pm 5\mu$m and $\sigma_Z = 30 \pm 7\mu$m. The SSD resolution is $\sigma_{\rho\phi} = 30\mu$m. Figure 2.12 shows an example of correcting the misalignment. Misalignment parameters are determined as slopes of straight line fits to histograms of the most probable deviations versus the corresponding derivative matrix [90]. The lines represent results of linear fits whose slope parameters (β) correspond to the measured misalignment. Shown in text are slopes β measured before and after applying corrections.

2.2.7 Silicon Strip Detector (SSD)

The Silicon Strip Detector (SSD) constitutes the fourth layer of the inner tracking system. It is located inside the TPC and outside the SVT. It provides two-dimensional hit position and energy loss measurements for charged particles, improving the extrapolation of TPC tracks through SVT hits. The SSD is placed at 23 cm from the beam axis and covers a pseudorapidity range of $|\eta| < 1.2$.

Its design is based on two clamshells each containing 10 carbon-fiber ladders. Each ladder is composed of 16 detection modules along the beam axis, two pairs of ADC board and C2D2 board located at the ends of the ladder. A low mass carbon fiber beam supports the modules, electronic boards and additional mechanical pieces which are used to attach the ladders and air cooling tubes. The 20 carbon fiber ladders are tilted 5° with respect to their long axis, allowing the overlap of the detectors in the transverse plane for better performance. The 16 detection modules on each ladder use a double-sided silicon strip technology with 768 strips per side and these modules are glued on the carbon ladder. Each ladder is 1060 mm long with a triangular cross section of 40 mm base. The ladders are made of carbon fiber which gives good rigidity

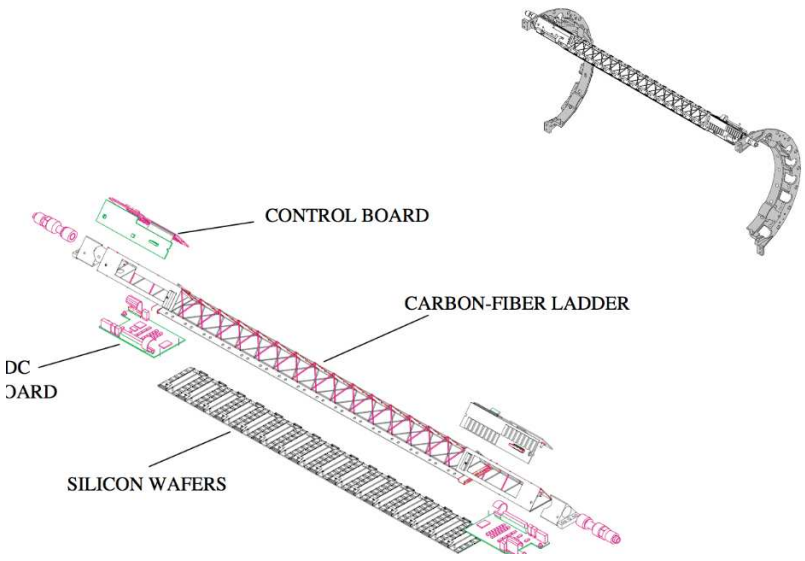

Figure 2.13: Exploded view of an equipped ladder and a half barrel support structure with one ladder

and allows low material budget. The wafers are 75 mm by 42 mm sized and 300 μm thick. The clamshell structure allows the SSD to be installed or dismounted easily. The cooling system is based on an air-flow through the ladder.

Tape automated bonding (TAB) technology was used to connect the detectors to their front-end electronics. TAB technology was used for the first time in a vertex detector [60].

2.2.8 Electromagnetic Calorimeter (EMC)

STAR utilizes electromagnetic calorimeters as a barrel (BEMC) and an endcap (EEMC) calorimeter enclosing the TPC. BEMC is located inside the aluminum coil of the STAR solenoid and covers $|\eta| < 1.0$ and 2π in azimuth, thus matching the acceptance for full TPC tracking. The EEMC covers the pseudorapidity range $1.086 \leq \eta \leq 2.0$.

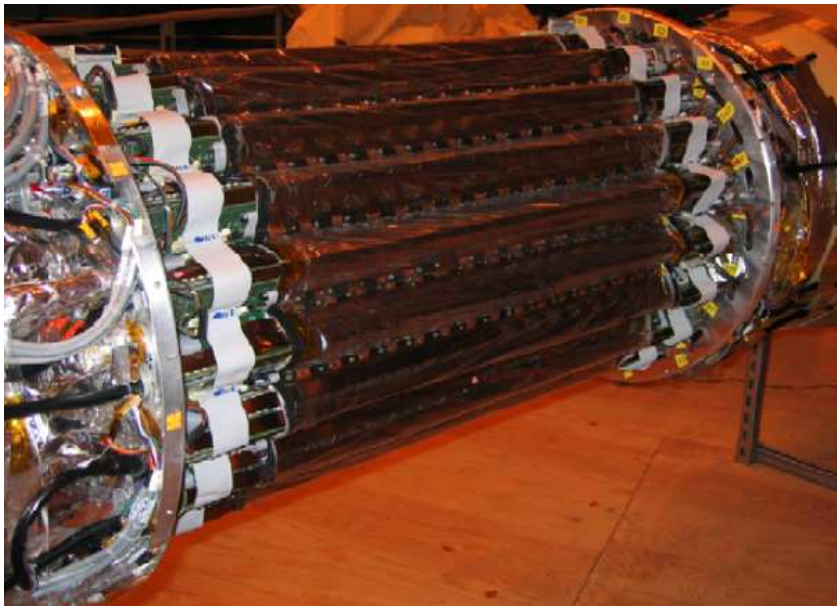

Figure 2.14: The SSD barrel installed on the cone support structure

The BEMC will help to trigger on and study rare, high p_T processes (jets, leading hadrons, direct photons, heavy quarks) and provide large acceptance for photons, electrons, π^0 and η mesons. The BEMC is an important tool in the study of vector meson production and identification of electrons by rejection of hadron background. The BEMC can identify electrons particularly in the low energy regime, where the most challenging hadronic background exists. It is central to STAR's spin physics program as well. The design of the BEMC includes a total of 120 calorimeter modules, each subtending 6° in $\Delta\phi$ and 1.0 unit in $\Delta\eta$. The modules are segmented into 40 towers. The full barrel calorimeter is thus segmented into 4800 towers, each of which is projective, pointing back to the center of the interaction vertex. The core of each module consists of a lead scintillator stack and shower maximum detectors placed approximately 5 radiation lengths from the front of the stack. There are 20 layers of lead/scintillator. The shower maximum detectors lie within the lead/scintillator stack

and they provide high spatial resolution of the electromagnetic shower reconstruction in two mutually orthogonal transverse dimensions. It is challenging to distinguish between π^0s and γs at high p_T ($\sim$ 25 GeV/c) even with the best electromagnetic shower resolution. Therefore, another preshower detector readout of each tower is provided. At the depth of the preshower detector, there is substantial difference in energy deposition between charged hadrons and electrons. This can aid in both π^0/γ and electron/hadron discrimination. A typical electron exhibits substantially higher ionization dE/dx, than hadrons, even before initiation of electromagnetic showers. On top of this, $\sim$ 63% of electrons will shower before entering the active volume of preshower and $\sim$ 84% by the middle of the preshower detector. This should be compared with a corresponding interaction probability of hadrons of approximately 3% and 6% [61].

EEMC provides full azimuthal coverage for high p_T photons, electrons and electromagnetically decaying mesons over pseudorapidity $1.086 \leq \eta \leq 2.00$. It aids in distinguishing between electrons and charged hadrons in higher pseudorapidities and offers triggering capabilities and coverage that are crucial for much of the spin physics program to be carried out in polarized proton-proton collisions. It includes a scintillating-strip shower-maximum detector to provide π^0/γ discrimination and preshower and postshower layers to aid in distinguishing between electrons and charged hadrons [62].

The main STAR operating calorimeters are the BEMC, the EEMC (EEMC) and the Forward Meson Spectrometer (FMS). Taken together they provide nearly complete EM coverage for pseudorapidity $-1 \leq \eta \leq +4$. There are other smaller calorimeters at STAR, notably the Zero Degree Calorimeters (ZDC), used for monitoring collider luminosity and Forward Pion Spectrometer (FPD). The FPD can reconstruct

forward π^0s, it is used to measure the transverse spin asymmetry arising from transversely polarized proton beam collisions at the STAR interaction region. The FMS was proposed to enlarge acceptance for gluon distribution studies.

2.2.9 Time Of Flight detector (TOF)

The latest detector system upgrade measures Time Of Flight, based on multi-gap resistive plate chamber (MRPC) technology. This full acceptance detector is essential to STAR's particle identification capabilities. It allows precision soft physics studies out to transverse momenta of approximately 2-3 GeV/c (depending on particle species) [28]. With TPC only, the PID capabilities of STAR limits the hadron (K and π) identification to 0.7 GeV/c, thus approximately 30% of the total number of charged hadrons in any given event cannot be identified. A TOF system with a total timing resolution of 100 ps in the STAR geometry, and with the tracking resolution of the STAR TPC, would allow π:K:p direct identification up to momenta near 1.7-1.9 GeV/c and (π + K):p identification up to 2.9-3.1 GeV/c. Combining the particle identification capabilities of the TOF with those from dE/dx in the TPC allows high efficiency particle identification capabilities over 98% of the hadron spectra, as well as cross-checks between the different PID techniques in the momentum regions where there is overlap. Over the last several RHIC runs, prototypes of the TOF systems were operating and a fully developed TOF system was installed for year 2010 data taking [63].

2.2.10 Ring imaging Cerenkov detector (RICH)

With a relatively small acceptance, this device increased the ability of STAR to identify particles at high momenta. The RICH detector covered 2% of the TPC acceptance covering $\Delta\eta < 0.3$ and $\Delta\phi = 20^\circ$ in the central rapidity region. RICH extended PID of kaons to 3 GeV/c and of protons to 5 GeV/c. The detector represented the first use in a collider experiment of a proximity-focusing RICH detector, with a MultiWire Proportional Chamber (MWPC) pad cathode coated with CsI. It was removed from STAR in the year

2.2.11 Photon Multiplicity Detector (PMD)

This detector is designed to measure photon multiplicity in the forward region where high particle density precludes the use of a calorimeter. The PMD, covering the pseudorapidity region $2.3 \leq \eta \leq 3.5$ with full azimuthal acceptance and placed behind the FTPC, is used to study fluctuation, flow and chiral symmetry restoration through a measurement of the spatial distribution of photons.

2.3 STAR Triggering System

The read-out time of most of these detectors (100 Hz) is much lower than the bunch crossing frequency (10 MHz) at RHIC. Also there is a need to differentiate between real collision events and detector noise. Therefore STAR has installed a triggering system, which operates at much higher frequency and which can improve operational efficiency by allowing only data to be written and digitalized. Interaction rates approach the RHIC crossing rates for the highest luminosity beams. Therefore, fast detectors, which can reduce the rate by almost 5 orders of magnitude, must be used. The STAR triggers are divided into Levels 0, 1, 2 and 3. Levels 0, 1 and 2 use

information from STAR's fast detectors (with readout times of $\sim 1\mu$ s) while the Level 3 trigger uses data from the slow detectors (with readout times of $\sim$ 10ms). The fast detectors include the Central Trigger Barrel (CTB), the Beam-Beam Counter (BBC), and the Zero-Degree Calorimeter (ZDC). The BBC is used to cover the high η region necessary for normalizing event rates in the p-p program. Level 3 is a software trigger, which uses data of the slower detectors TPC, SVT and FTPC. The level 0 system consists of the Central Trigger Barrel (CTB) and Zero-Degree Calorimeter (ZDC) and is responsible for delivering a signal to the slow detectors to start readout. Level-0 detectors (CTB and ZDC) will be discussed in the following section. Level 1 can abort an event during the readout (40μs for the TPC). After the readout, the data is digitalized on the detector front-end electronics, which takes $\sim$ 10 ms for the TPC. During this time the Level 2 can abort an event before the data are transmitted to the Data Acquisition (DAQ) system. An additional trigger layer L3 is introduced. Level 3 receives additional information from other subdetectors (TPC, SVT, FTPC etc.) and contains cluster finder and track finder, which permits it to select the events to be stored [64][65]. With the upgraded DAQ 1000 STAR has a rate of reading about 1000 Au-Au collisions per second (about 800 Hz - 1 kHz in 2010).

2.3.1 The Central Trigger Barrel (CTB)

The Central Trigger Barrel (CTB) was one of the primary trigger detectors for STAR. It covered the outer shell of the TPC spanning 1/2 units of pseudorapidity and records charged particle tracks. The CTB was removed when the TOF detector was installed for RHIC run 2009. TOF uses the vacated space from the removal of the CTB trays. CTB consisted of 240 scintillator slats arranged in four cylindrical bands. Each slat consisted of a radiator, light guide and photomultiplier tube (PMT).

The slats were placed on aluminum trays to ease handling and mounting on STAR, with two slats end-to-end in each tray. When charged particles travel through these scintillators, they energize the electrons to higher energies. When these excited electrons decay, electromagnetic radiation is given off and it is guided into the PMT by the light guide. Inside the PMT the light is incident on photocathodes, creating an electron shower and it is amplified to be strong enough for the read-out by the trigger detectors. The CTB gave stronger signal for more central collisions since such events produce more particles at midrapidity.

2.3.2 The Zero-Degree Calorimeter (ZDC)

All RHIC experiments have a pair of Zero Degree Calorimeter detectors. ZDCs are used for beam monitoring, triggering, and locating interaction vertices. Each ZDC consists of three modules. Each module consists of a series of tungsten plates alternating with layers of wavelength shifting fibers that route Cerenkov light to a PMT. They are placed along the beam lines on either side of the interaction regions. The ZDCs detect neutron fragments generated in the collision. The hadronic minimum bias trigger requires a coincidence between the east and west ZDCs. The ZDC signal is small for the highest multiplicity (central) collisions and it is strongest for peripheral events. This is because peripheral events have larger numbers of neutron fragments.

The geometry of the collision is based on the neutrons detected in the ZDCs and on charged particles detected in the CTB. The correlation between these signals is shown in Fig. 2.15. The figure shows a region of strong forward neutron production for which there are only few charged particles in the CTB. It also shows a region of high charged multiplicity with low neutron signal. Most central collisions correspond

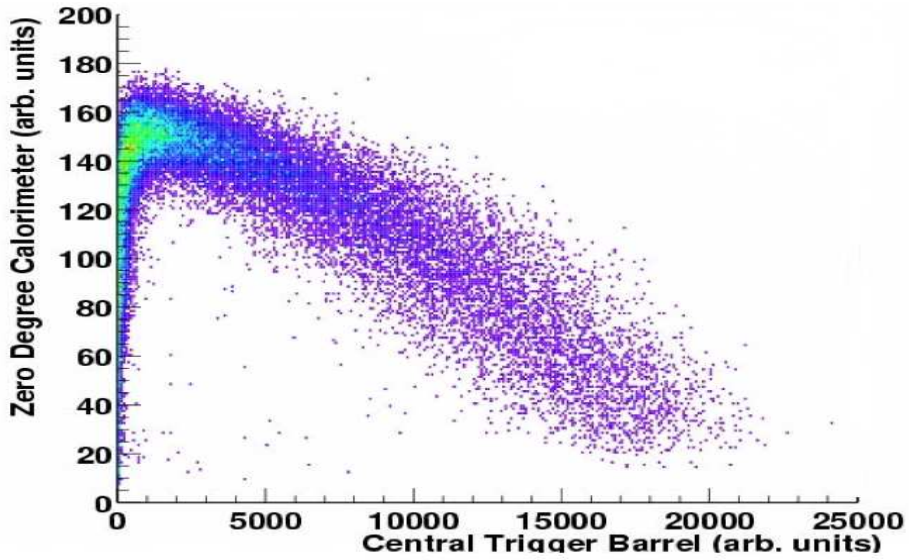

Figure 2.15: Correlation between ZDC and CTB signals

to high CTB multiplicity and small number of forward spectator neutrons. The centrality is closely related to the multiplicity of particles and can be calculated through the Glauber model for choosing a certain impact parameter range [71].

2.3.3 Vertex Position Detector (VPD)

Primary vertex finding is an important part of accurately reconstructing events at STAR. The STAR Vertex Position Detector (VPD) can be used to measure the location of the vertex. There are two VPDs located on the east and west side of the interaction region. The VPD can determine the z location of a vertex by measuring the time difference between the signals that arrive from the East vs West. The Level-3 trigger receives data from the VPD. Figure 2.16 shows the position of the STAR VPD with respect to the TPC.

There are 19 detector channels on each side. The inner radius of the detector is

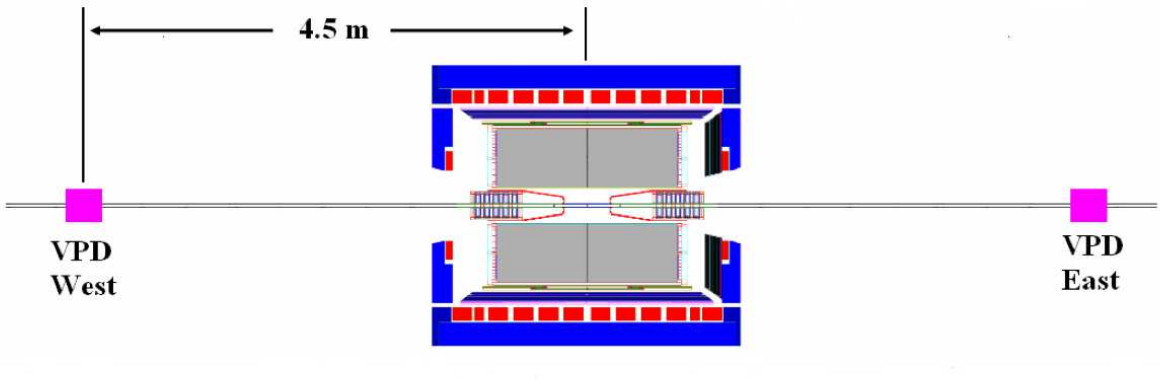

Figure 2.16: Position of the STAR VPD with respect to the TPC.

6.98 cm and outer radius is 16.51 cm. Since the VPDs are placed at forward rapidities they have good time resolution, $\sim$ 150 ps (forward particles are typically very fast). Thus the z- vertex resolution of the VPD is $\sim$ 3 cm. In p+p collisions the VPD found a vertex in 25% of events with a vertex resolution of $\sim$5 cm [66].

2.4 Heavy Flavor Tracker (HFT) - the future upgrade to STAR

In order to improve the measuring capabilities, STAR is upgrading its central silicon detector. The Heavy Flavor Tracker(HFT) is a microvertexing detector using active pixel sensors and silicon strip technology. The HFT can do a precise measurement of heavy flavor by direct topological reconstruction of D mesons and can disentangle the charm and bottom contributions to the observed spectra. The HFT will be able to measure neutral and charged particles with displaced vertices of 100 μm or less from the primary vertex. The HFT will replace the decommissioned SVT (using drift technology) with active pixel technology. The Silicon Vertex Tracker (SVT) of STAR was too thick to provide event-by-event charm identification because

of multiple scattering.

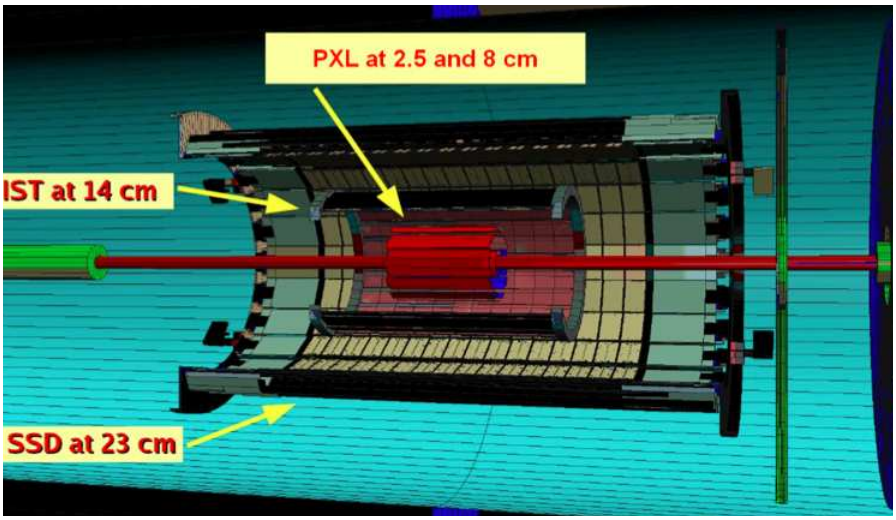

Figure 2.17: The STAR - Heavy Flavor Tracker (HFT)

The HFT consists of two subdetectors: a silicon pixel detector (PIXEL) and an intermediate silicon tracker (IST). Both these detectors lie inside the radial location of the SSD. The SSD-IST-PIXEL detector serves the purpose of graded resolution from the TPC to the interaction point and has an excellent capacity to resolve secondary particles and displaced decay vertices. The PIXEL is composed of two layers of monolithic CMOS active pixel sensors placed at 2.5 cm and at 8 cm from the beam axis, which can measure with great accuracy the position of a particle within a few centimeters of the interaction region. The very thin layers minimize the multiple coulomb scattering. The IST layer placed at 14 cm and the SSD placed at 23 cm can link tracks from the TPC to the PIXEL [49]. Figure 2.17shows a cross-sectional view of the HFT with various layers. Table 2.1 gives a summary of the characteristics of the HFT layers.

Detector	Radius (cm)	Technology	Si thickness (μm)	Hit resolution R/ϕ - Z (μm)
SSD	23	double sided strips	300	30-857
IST	14	Si Strip Pad sensors	300	170-1700
PIXEL	2.5, 8	Active Pixels	50	8.6 - 8.6

Table 2.1: Characteristics of each silicon layer of the HFT.

Chapter 3

Data Analysis

In this chapter, I discuss the analysis method we use for the direct measurement of charm. The method uses a microvertexing technique, which utilizes track information from TPC, SSD and SVT for the topological reconstruction of $D^0(\bar{D}^0)$, through the decay channel, $D^0(\bar{D}^0) \longrightarrow K^-\pi^+(K^+\pi^-)$. Microvertexing is the process of reconstructing the secondary vertex through a fit to the D^0 daughter tracks. The program uses various quality cuts to select good events and track candidates which might come from the decay of a $D^0(\bar{D}^0)$. These cuts were first imposed on simulated data files to optimize signal retention and then later they were applied to real data. This chapter includes details about the datasets, cut variables and the cut sets used for our analysis.

3.1 Introduction

Direct reconstruction of heavy flavor through hadronic decays is done through $D^0(\bar{D}^0) \longrightarrow K^{\mp}\pi^{\pm}$ (with a branching ratio of 3.8%) and $D^{\pm} \longrightarrow K\pi\pi$ (B.R. = 9.2%). In addition, STAR measures the charm-strange yield, $D_s^{\pm}$ decaying into ϕ+$\pi^{\pm}$, with $\phi \rightarrow K^+K^-$ (B.R. = 2.18%). Direct reconstruction of D mesons presents the cleanest probe to investigate heavy quarks in relativistic heavy ion collisions, but the small branching ratio and the lack of dedicated detector triggers require large statistics for the analysis. The D^0 meson is a neutral particle and has a mass of 1864.84 MeV/c^2. It decays through a weak interaction processes and have a life time of 123 μm. Its short

life-time imposes many hurdles in the signal extraction, given the current detector capabilities.

Particles containing heavy quarks can decay semi-leptonically in a manner analogous to nuclear β-decay. Figure 3.1 shows Feynman diagrams for decays of D^0 mesons, both semi-leptonically and hadronically.

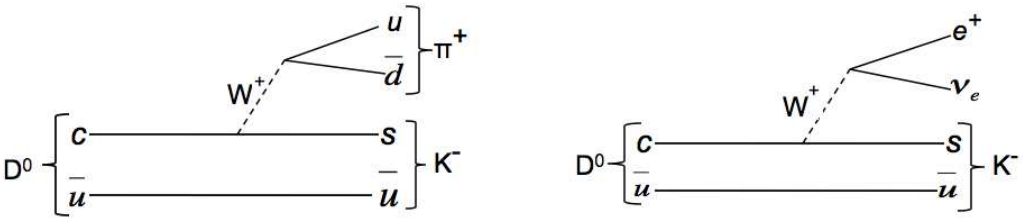

Figure 3.1: Feynman diagrams of D^0 decays through hadronic (left) and semileptonic channels (right)

Since the branching fractions of semileptonic mode are larger, these modes are much more accessible experimentally. Extensive measurement of heavy quarks is done through semileptonic modes at STAR. However, due to smeared kinematics and unknown contributions from charm and bottom to the non-photonic electron (NPE) spectra, a full topological reconstruction of D^0 through its hadronic decay mode is required. Moreover, there is a huge photonic background in the NPE method, arising largely from photon conversions in the detector material. So a direct measurement of charm is needed through its hadronic decay channel. In this analysis, we try to do this through identification of the kaon ($K^{\mp}$) and pion ($\pi^{\pm}$) tracks. Once the

good track candidates are selected by using appropriate cut values, the decay vertex reconstructed using a secondary vertex fit method. Topological reconstruction of decay vertices significantly reduce the combinatorial background mainly of particles coming from the collision vertex. The cuts are discussed in the sections that follow in this chapter.

3.2 Data Sample

We used three different data sets: pure D^0 events, D^0 mixed with Au+Au HIJING events, and real data from run VII Au+Au collisions at $\sqrt{s_{NN}} = 200$ GeV. HIJING is a Monte Carlo event generator for simulating particle production in high energy hadronic and nuclear collisions based on QCD-inspired models for multiple jet production. Embedding data was used to do corrections for acceptance, efficiency etc. These corrections are discussed in Chapter 4 (see Section 4.4).

3.2.1 Monte Carlo data

In order to learn how the signal parameters behave, we used a sample of simulated 'pure D^0 events' where D^0s were generated with transverse momentum of the following functional form in unit rapidity:

$$\frac{d^2N}{dp_T dy} = A[1 + \frac{p_T}{p_0}]^n \tag{3.1}$$

where p_0 and n are two parameters, which are related to the mean transverse momenta by the relation: $\langle p_T \rangle = \frac{2p_0}{(n-3)}$. The value of $\langle p_T \rangle$ is selected to be 1 GeV/c. This power law function was used to match the p_T distribution with the anticipated data spectrum [67]. Figure 3.2 shows the generated p_T distribution for various n values along with the real data distribution itself.

We sample random values of this distribution for the transverse momentum of D^0

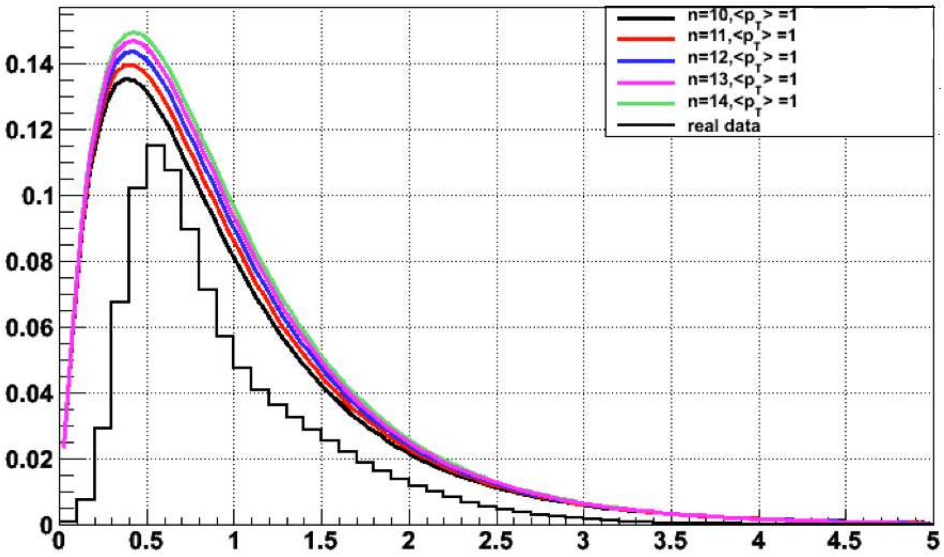

Figure 3.2: Power law p_T distribution of simulated D^0 mesons

candidates. The parameters chosen are $n = 10$ and $\langle p_T \rangle = 1$ GeV/c. The phase space characteristics of the D^0s generated are: transverse momentum, $0 < p_T < 5$ GeV/c, rapidity, |y| <1 and flat distribution in azimuth, $0 < \phi < 2\pi$.

For background events we used central Au+Au HIJING events, with impact parameter[1], $b = 0 - 4.5$ fm. HIJING doesn't normally produce charm mesons, therefore it is an ideal environment to study combinatorial background. The geometry used for running the 'Big Full Chain (BFC)[2] was y2007g, which was the closest to the detector set up in run-7. y2007g geometry uses the GEANT[3] [68] configuration with

[1]It is the distance between the centers of the colliding ions. See Appendix C.

[2]A program for reconstruction of raw digitized detector data into detector hits, energies, particle trajectories, momenta and identification of particle species. This results in the production of data summary files consisting of a list of reconstructed particles and their properties (DAQ files gets through BFC and creates Event.root files).

[3]GEANT is a detector description and simulation tool. It can track elementary particles through the experimental setup for simulation of detector response and files have the tag .geant.root

the TPC, SVT, SSD etc.[68], which are the main subsystems we utilized in order to get the pointing accuracy for the microvertexing method used here. This geometry also takes into account the dead material[4] in the SVT. To study the signal in the presence of background, the D^0 particles generated with power law p_T distribution are mixed with HIJING events. Figure 3.3 shows the simulation phase-space settings for the D^0s generated.

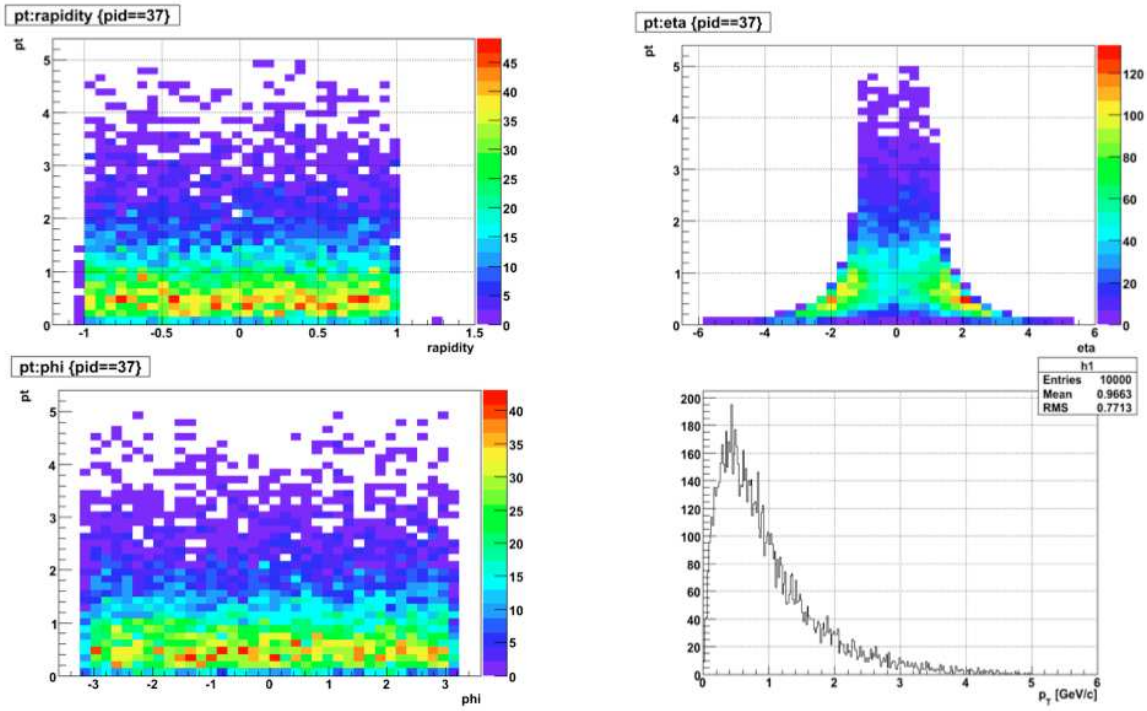

Figure 3.3: Phase space settings of the simulated D^0 mesons

3.2.2 Real Data

The data used for this analysis is from year 2007 RHIC run (Run-7). Au+Au beams were collided at center-of-mass energy 200 GeV per nucleon. Run-7 included

[4]Support structures such as ladders, not the dead wafers.

the inner tracking detectors, SVT and SSD. This run had an additional change from previous years, which was the addition of the VPD detector to trigger on vertices less than 5 cm from the center of the detector along the z axis. This ensured the inclusion of vertices in the acceptance of SVT+SSD. The main production trigger setup names of this production are 2007 Production2, which contains mostly minimum bias but also rarer triggers, and 2007 ProductionMinBias, which contains minimum bias events (mb-vpd)[5]. Run 7 recorded 81 million events, out of which 62 million were ProductionMinBias events. Table 3.1 shows the data sample we selected:

Stream	Contents	Trigger Name	Detectors	Events
	Prod2, ProdMinBias			81M
Physics	Prod2, ProdMinBias	mb-vpd($\|V_z\| < 5$cm)	TPC	74M
	Prod2, ProdMinBias	mb-vpd	TPC+SVT+SSD	69M

Table 3.1: The data sample in year 2007 Au-Au run.

3.3 Analysis Procedure

The analysis of data in STAR proceeds in two stages. In the first stage, the raw digitized detector data is processed with the reconstruction program - BFC. This process involves track fitting using different methods (see Appendix A) and the output is stored as .Event.root files. These tracks are organized and sorted to produce data summary tapes with information on detector hits, particle trajectories, momenta, hits and species identity etc as .MuDst.root files. The MuDst files are smaller root files that contain reconstructed particles and their properties. The second stage involves a detailed study of these reconstructed collision events in MuDst files to search for

[5]A minimum-bias trigger is one that accepts any nucleus-nucleus collision. Very peripheral collisions are difficult to trigger on, since very few particles are emitted from such events and there is bias against such events. A minimum-bias trigger tries to keep any bias as small as possible.

physics phenomena. The analysis procedure described in the following section is topological reconstruction of $D^0(\bar{D}^0)$ from MuDst files, using microvertexing code.

3.3.1 Decay topology

Figure 3.4 shows the schematic of the decay of $D^0(\bar{D}^0)$ through their hadronic and semileptonic decay channels. We measure the hadronic decays (shown in the lower

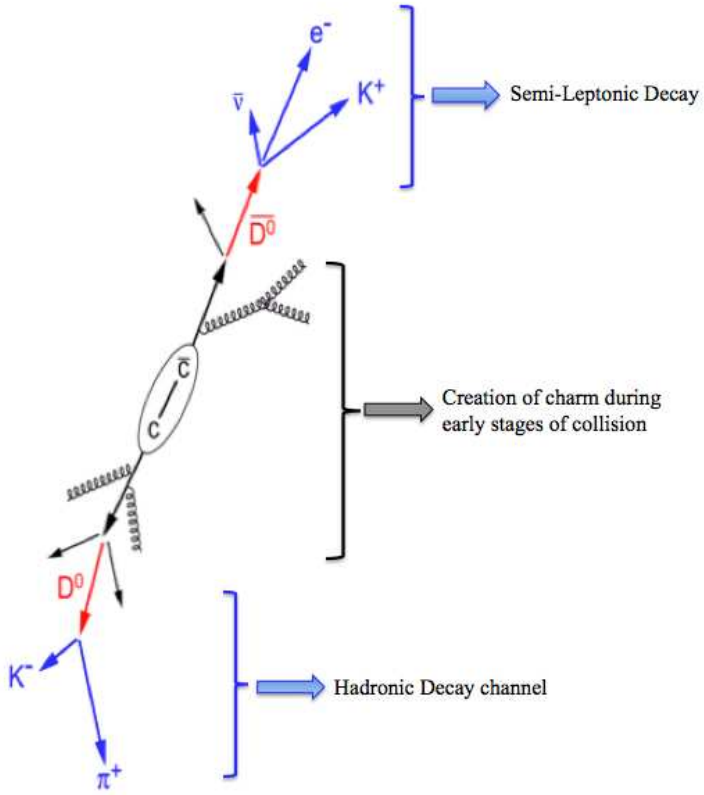

Figure 3.4: $D^0(\bar{D}^0)$ decay diagram

half of the decay diagram). D^0s are very short-lived particles with $c\tau \sim 123$ μm. For a realistic D^0 distribution at mid-rapidity the mean transverse momentum, $p_T \sim 1$

GeV/c and the average decay length is 60-70 μm[6]. However, the current detector resolution is $\sim$ 200 μm at 1 GeV/c at the best. This causes huge background levels and therefore requires efficient background subtraction methods for signal extraction. Figure 3.5 shows the D^0 decay length distribution in the X-Y plane using a simulated data of pure signal events. As can be seen from Fig. 3.5 the distribution has a mean value of $\sim$ 65 μm.

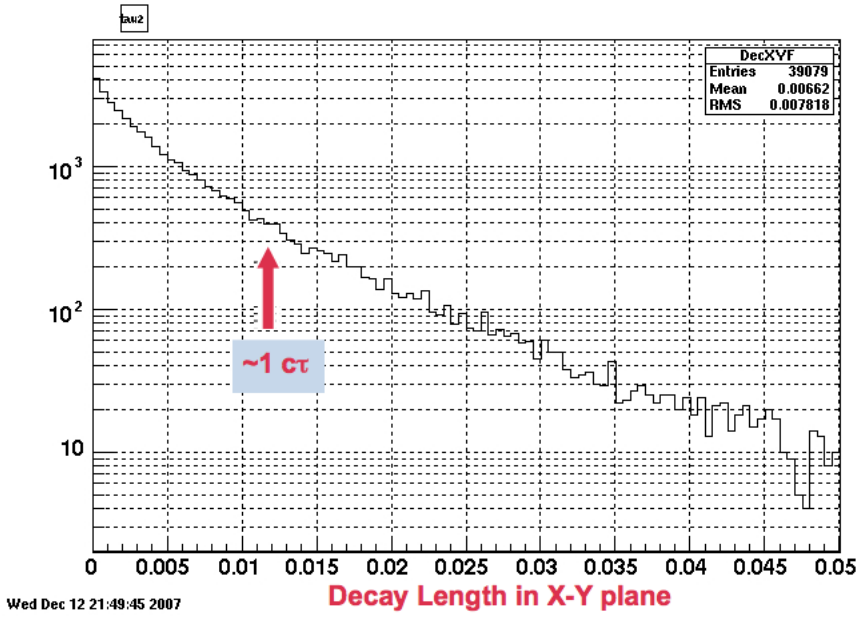

Figure 3.5: Decay length distribution of D^0 in the X-Y plane

To reconstruct a $D^0(\bar{D}^0)$ candidate, oppositely charged K and π tracks are paired. The invariant mass of a D^0 candidate can be determined from the measured momenta of the tracks and assuming the mass of the daughters using the formula,

$$M_{\rm inv}^2 = M_+^2 + M_-^2 + 2(E_+E_- - \mathbf{p}_+ \cdot \mathbf{p}_-) \tag{3.2}$$

[6]A D^0 particle with mean momentum 1 GeV/c has $\beta\gamma = 0.5311$. This means that the D^0 are 'unboosted' in a collider, i.e, relativistic effects are almost negligible.

where the positive and negative subscripts refer to the positively and negatively charged daughter tracks (K and π) and c is taken as 1.

3.3.2 Topological Reconstruction with μvertex Code

The macro uses several loops to associate daughter tracks in the events stored in the data summary files (.MuDst.root files). While it iterates through the event structure, the code uses several quality cuts, both to reduce background and to speed up the run process. The first loop is over the events and the second loop is over all the vertices in that event. We select the best vertex assigned to that event during reconstruction (saved in .MuDst.root files) by a cut on vertex index = 0. Cuts on the vertex position and position resolution along the z-axis are also used. A third and a fourth loop within the third, are over the primary tracks to select K, π candidates. The loop over tracks makes no distinction between K and π tracks nor a distinction on the charge of the tracks. This is to accept both D^0 and $\bar{D}^0$ particles. The particle identification is obtained from the TPC dE/dx measurements, which will be discussed later. The primary tracks should correspond to the primary vertex index zero, or else it is rejected. In the next step, the global track corresponding to the primary track is selected and subjected to quality cuts and secondary vertexing. (Details on primary and global track are included in Appendix A.) In summary, the μvertex code proceeds in the following way:

1. Loop over event - select trigger

2. Loop over the primary vertices in the selected event and pick the vertex corresponding to index l = 0, apply vertex-level cuts to select good events.

3. First loop over primary tracks (index k). If the primary vertex index of the

track doesn't match with l, it is rejected. For each primary track selected, the global track associated to it is used - track-level quality cuts are applied.

4. Second loop over primary tracks, select a track different from the first. If the primary vertex index of the track doesn't match with l, it is rejected. The global track associated to the primary track is used - track-level quality cuts are applied.

5. Track pairs are subjected to secondary vertexing.

6. Apply cut on standard deviation of dE/dx bands to identify K and π tracks.

7. The D^0 candidate is built by combining K and π tracks that pass the cuts. For this, the momentum components are obtained from the global tracks and a TVector3 class is used to save the momenta of the tracks. In the next step, we use TLorentzVector class and save the momentum and energy of the track.

```
p4[0][0].SetVectMag(p[0],amK);
p4[1][0].SetVectMag(p[1],amPi);
```

where amK is the mass of K and amPi is the mass of the π. p[0] and p[1] are the three-vector momenta (TVector3) of the K and π tracks. The D^0 candidate can be built by summing the above two Lorentz vectors.

```
PP[0] = p4[0][0];
PP[0] += p4[1][0];
```

We can now get access to the D^0 candidate momentum components; PP[0].X(), PP[0].Y(), PP[0].Z(). PP[0] is the TLorentzVector of the D^0 particle.

3.3.3 Event-Level Cuts

We selected minimum bias events with conditions for a coincidence triggering of the ZDC detector and for triggering on vertices with z-position (V_z) < 5 cm by the mb-vpd trigger. This ensured to constrain the vertex into the acceptance of SVT+SSD.

Events can have several vertices with different positions and resolution. Ranks were assigned to the vertex positions determined, based on the likelihood and number of matching extrapolated tracks. We selected the highest ranked vertex with index = 0. This cut removed events with low multiplicity and could improve resolution. A vertex position cut, $|V_z| < 10$cm is used to select events that were were reconstructed well and in the region around $V_z = 0$. The cut on V_z helped to select tracks that did not cross a lot of detector support material and that were in the heart of SVT acceptance region. Another cut used is on the vertex position resolution, $\sigma_{ZVrtx} <$ 200 μm along the z-axis. Table 3.2 summarizes the cuts applied at the event level.

DataSet	Cut	Value
AuAu Run-VI	Trigger Id	200001, 200003, 200013
	vertex index (rank)	0 (highest rank)
	|ZVrtx|	$< 10cm$
	$\|\sigma ZVrtx\|$	$< 200\mu m$

Table 3.2: Cuts applied at the event level in Run-7 AuAu data.

Figure 3.6 shows the distribution of vertex position (top row) and position resolution (bottom row) in the X-Y plane as we apply the vertex level cuts. The vertex level cuts helps in cleaning up the sample and selecting the best vertices. Figure 3.7 shows the primary vertex position and resolution along the z-axis before and after the z-vertex cuts. By limiting to vertices close to (0,0) we can choose events in the

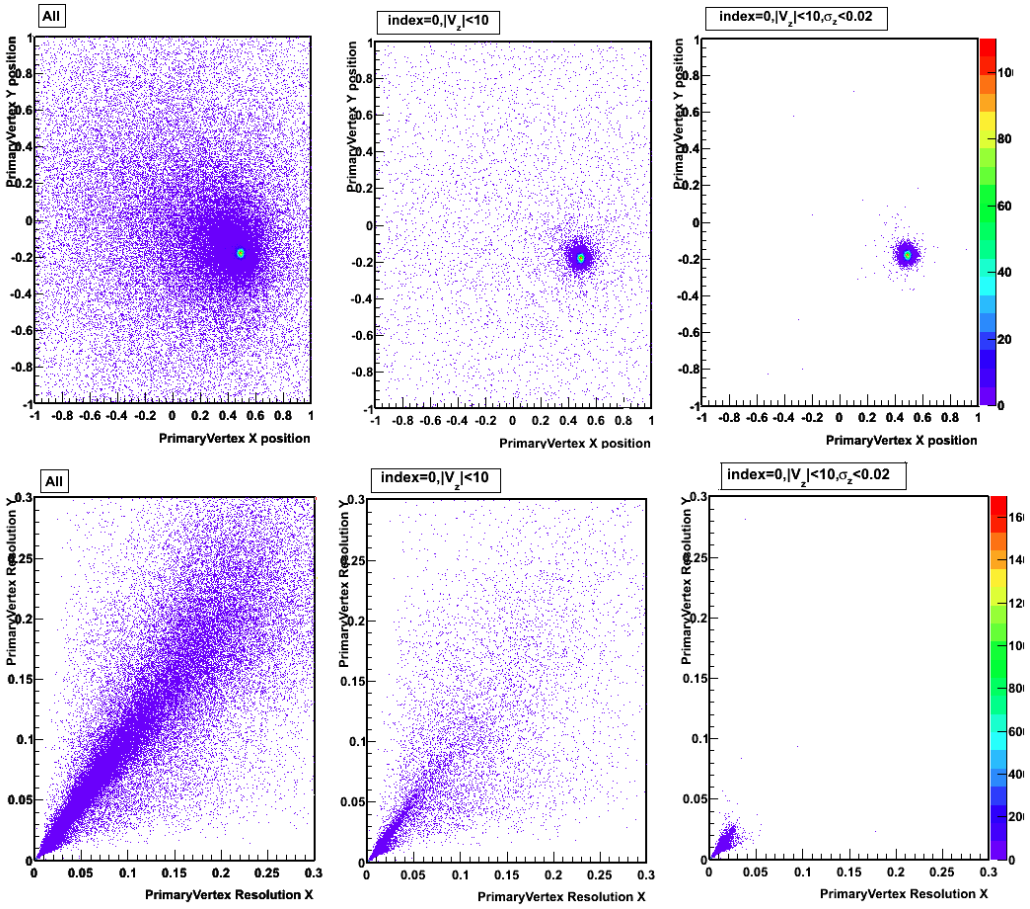

Figure 3.6: Primary vertex position and vertex resolution in the X-Y plane.

acceptance of the silicon detectors. Silicon detector information is crucial for the pointing accuracy of secondary vertex reconstruction.

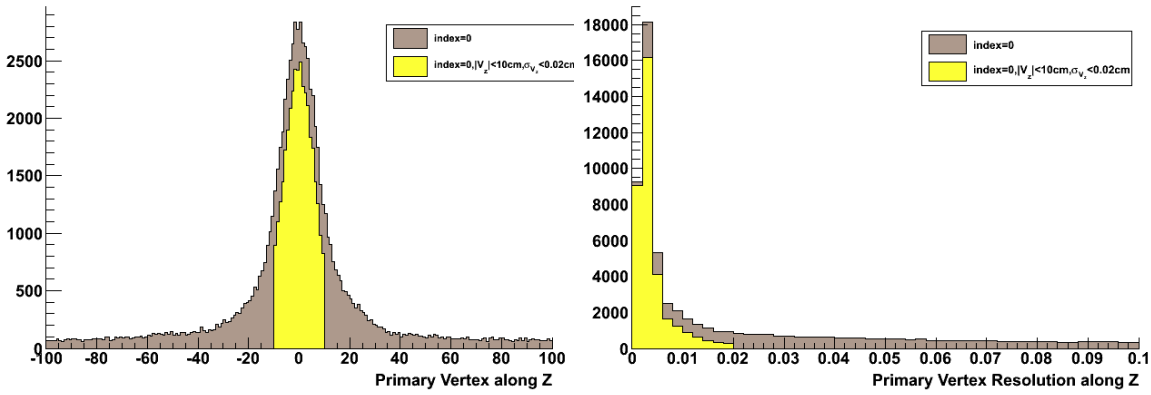

Figure 3.7: Primary vertex position and resolution along the z-axis.

The approximate number of charged particles at mid-rapidity ($|\eta|$ <0.5) per nuclear collisions, is called the 'reference multiplicity' in STAR. A cut on reference multiplicity is used later as an offline cut to select different centralities. The inclusion of inner tracking for Run-7 Au-Au data required a modification in the calculation of reference multiplicity. The proposed new variable (gRefMult) counts global tracks under $|\eta| < 0.5$, $|\mathrm{DCA_{global}}| < 3$ cm and number of Hits Fitted ≥ 10. This was because the reconstruction efficiency seem to depend on the primary vertex position in $|V_z| <$ 30 cm region. However, this dependence was generally absent for TPC-only tracking. There was loss of primary tracks for events under SVT/SSD. It was determined that the reconstruction efficiency of gRefMult was stable as a function of z-vertex position. A Monte Carlo Glauber simulation (Appendix C) is used to define the centrality of events as given in Table 3.3. We use an offline cut on gRefMult to study charm signal for various centralities.

3.3.4 Track-Level Cuts

A detailed study of cut variables is the most essential part of data analysis, especially for signals in the presence of a large background. This needs to be done for

Centrality	gRefMult
0-5%	≥ 485
0-10%	≥ 399
0-20%	≥ 269
0-30%	≥ 178
0-40%	≥ 114
0-50%	≥ 69
0-60%	≥ 39
0-70%	≥ 21
0-80%	≥ 10

Table 3.3: gRefMult and corresponding centrality in Run-VI Au-Au data [69]

both signal and background. Resolution of the reconstructed variables also plays an important role when setting the cut values. The cuts applied at the track level to select $K^{\mp}$ and $\pi^{\pm}$ before they are subjected to the secondary vertexing are discussed below.

Momentum Cut: At low momentum, due to multiple Coulomb scattering (MCS) the resolution of tracks is degraded. These are poorly reconstructed tracks. Also there is a huge pion background at low momentum. Therefore, a lower cut on momentum is sometimes necessary. Since $\langle p_T \rangle$ of D^0 is ~ 1 GeV/c, this could affect the kinematics depending on the cut value. In order to keep the kinematics unaffected while reducing the low p_T background, we tried a cut on the sum of the momentum of the tracks. The cut is $P_K + P_\pi > 1.5$ GeV/c. This removes some uncorrelated tracks without affecting the decay kinematics. The left plot on Fig. 3.8 shows the momentum of tracks and the right plot shows the sum of momentum of track candidates in 2007 Au-Au ProductionMinBias data.

Rapidity and Pseudorapidity: Longitudinal distributions of secondary particles from high energy reactions are usually studied in rapidity (y) or pseudorapidity

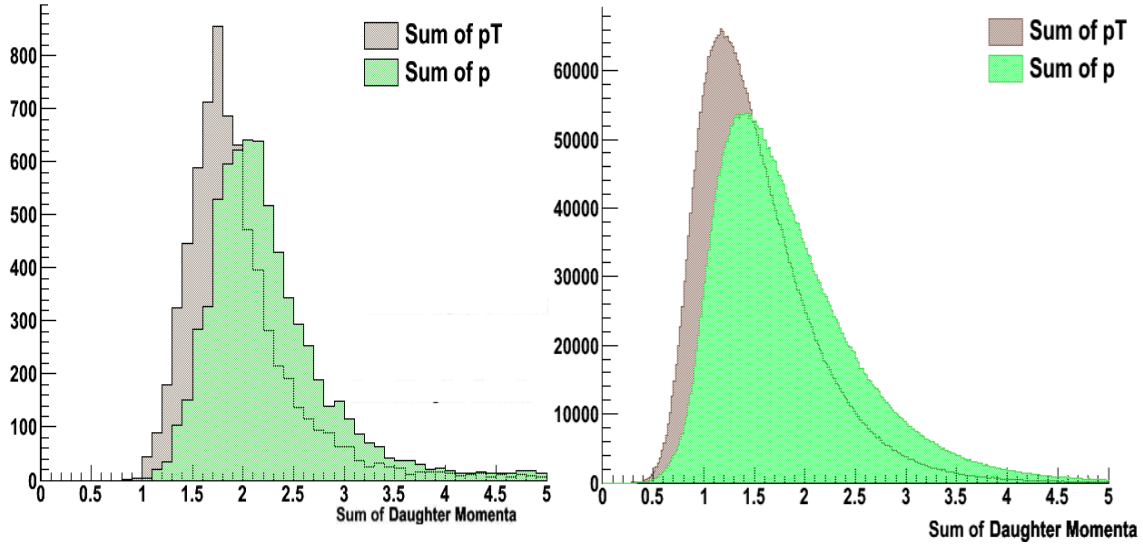

Figure 3.8: Track momenta distributions in pure D^0 (left) and Run-7 Au-Au (right) data

(η) variables. The rapidity is defined as

$$y = \frac{1}{2}\ln\left(\frac{E + p_z}{E - p_z}\right), \tag{3.3}$$

where p_z is the parallel component of momentum along the beam direction. Rapidity is additive under Lorentz transformations: $y\prime = y + a$, where $y\prime$ is the rapidity in the lab frame, y is the rapidity in the center-of-mass frame. This means that the shape of the rapidity distribution is invariant under Lorentz transformations (see Appendix B). For ultrarelativistic particles, $\beta \approx 1$ and $E \approx p$ and rapidity can be approximated by pseudorapidity,

$$\eta = -\ln\tan(\frac{\theta}{2}) \tag{3.4}$$

where $\theta = p_z/p$. We applied a cut on the pseudorapidity of the charged daughter tracks to be < 1.2, which is the pseudorapidity coverage of the silicon vertex detectors.

A cut on rapidity, $|y| < 0.5$, was applied later when calculating the yield and p_T spectra, so as to avoid another term in the calculation of $d^2N/dydp_T$.

Number of TPC hits: The tracks selected are required to satisfy the condition

$$\frac{nHitsFit}{nHitsPossible} > 0.51. \tag{3.5}$$

The numerator is the number of TPC hits fitted with a helix approximation and the denominator refers to the TPC hits possible. A track can have a maximum of 45 TPC hits. As the fitted points increase, the momentum resolution of the track gets better since more fit points implies a greater track length. The cut on the ratio of fitted points to hit points helps to avoid split tracks, a situation where the reconstruction software takes hits from one track and generates two separate ones. Figure 3.9 shows this variable from real data.

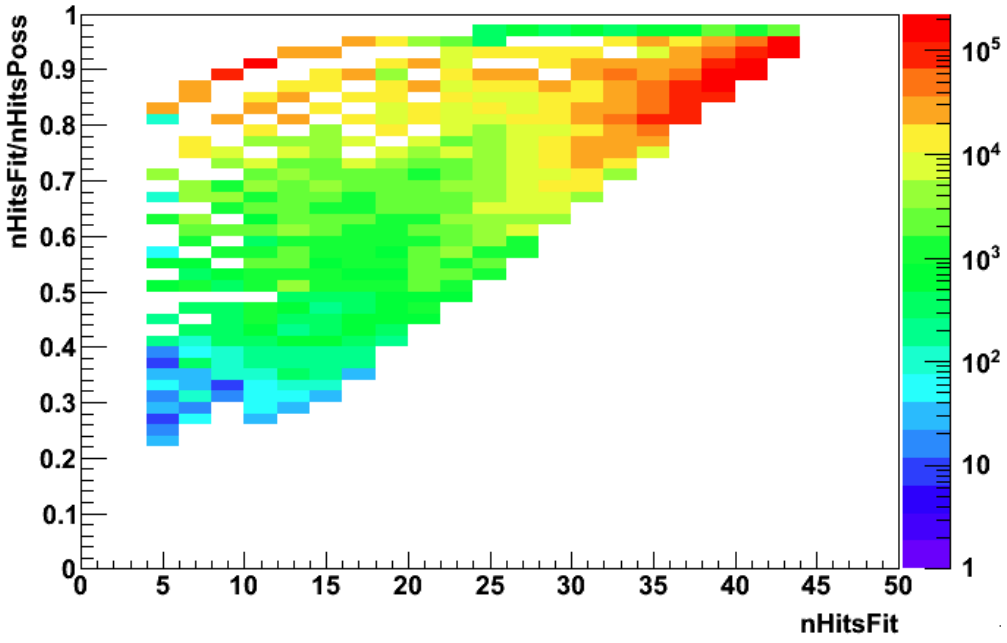

Figure 3.9: Ratio of TpcHits fitted to TpcHits possible

dE/dx **TrackLength**: This is the track length in the TPC that is used for the dE/dx calculation. We use a cut of dE/dx track length > 40 cm in our analysis. A lower cut on this variable ensures a better fitting on the track, and also ensures that the tracks reach the TPC.

Silicon (SVT+SSD) Hits: Silicon hit information is an important cut variable used for the pointing resolution. A requirement on the number of silicon hits (SiHits) as well as the radius of the first hit is crucial for this analysis. These will be discussed in detail in Sec 3.3.5.

Kaon decay angle in the D^0 rest frame: The variable θ^* refers to the angle made by the kaon in the CM frame to the lab D^0. In the CM frame the D^0 is at rest and the daughters decay back-to-back. Figure 3.10 shows a schematic of the decay of D^0 in the lab frame and in the CM frame.

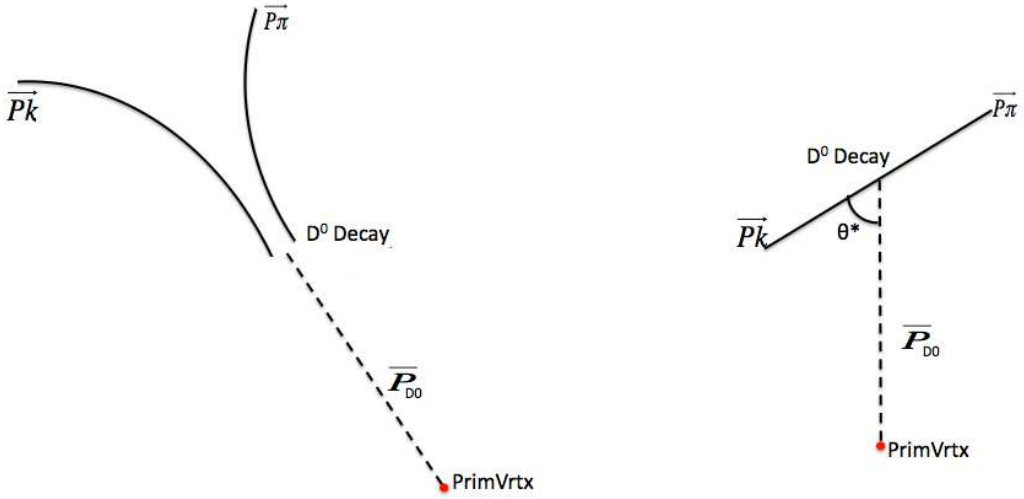

Figure 3.10: Schematic diagram of D^0 decay in the lab and CM frames

I will discuss the motivation behind this cut variable by considering the cases

where $\cos(\theta^*)$ has the extreme values $\sim \pm 1$. When $\cos(\theta^*)$ is close to -1, the angle θ^* takes values close to 180°. This means the K is decaying in a direction opposite to the parent D^0. These kaons will be even slower after the 'boost' in the opposite direction. The track reconstruction efficiency has a steep slope at low momenta and therefore these soft Ks are unlikely to be reconstructed well. When $\cos(\theta^*)$ is close to $+1$, the angle θ^* takes values close to 0, therefore the kaon is emitted parallel to the parent D^0. This leads to the production of soft pions.

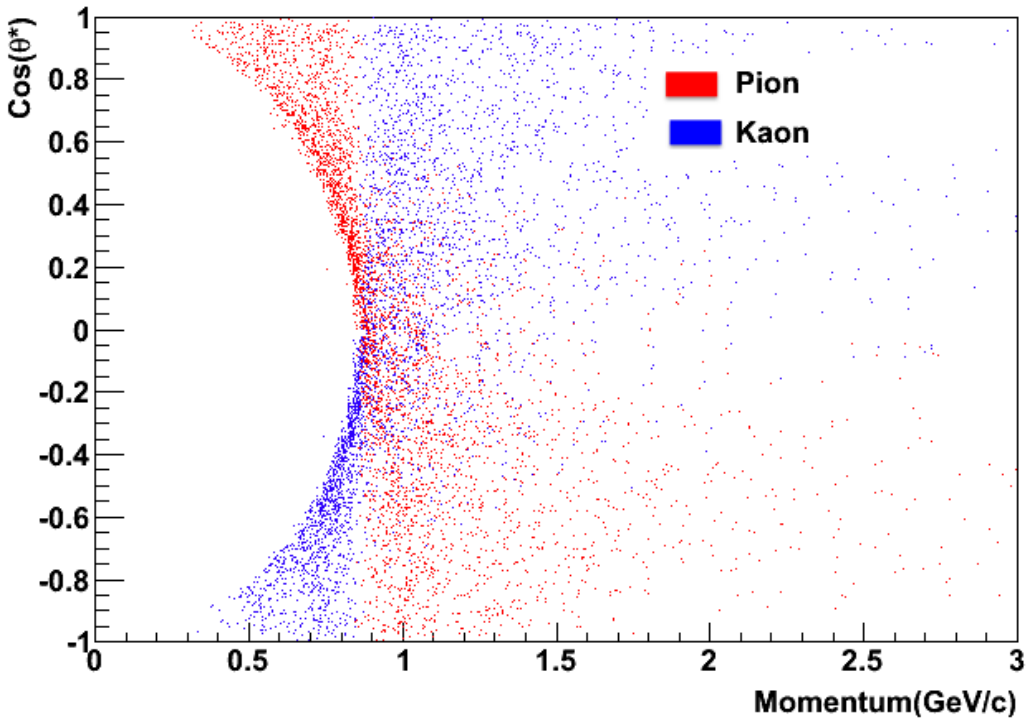

Figure 3.11: Kaon decay angle versus daughter momentum in CM frame

So a cut on $|\cos(\theta^*)| < 0.8$ removes the very soft kaon and pion tracks and therefore is used while running the microvertexing code. Figure 3.11 shows the dependence of kaon decay angle and track momentum for kaons and pions for pure D^0 signal events.

3.3.5 Role of Silicon Detectors (SVT+SSD)

Since D^0 mesons are short-lived particles, track information close to the interaction vertex is needed for its reconstruction. Run - 7 used the silicon vertex detector, 3-layer SVT and a 1-layer SSD during data taking. We use the track hit information from the silicon detector together with the TPC for the pointing resolution. Pointing resolution refers to the impact parameter resolution of primary tracks to the primary vertex, it is the heart of the microvertexing method. Since silicon hits give us track information close to the beam pipe it gives better resolution. Thus track hits in silicon layers are very important for our analysis.

As a first step in the reconstruction process, the daughter tracks are extrapolated towards the primary vertex. This allows us to find a point where the distance of the track to the primary vertex is minimal, the distance of closest approach (DCA). The figure of merit used is the pointing resolution of this variable for reconstructed tracks ($\sigma_{\mathrm{DCA_{XY}}}, \sigma_{\mathrm{DCA_Z}}$). The DCA resolution gets better as the number of track hits in the silicon layers increases.

Figure 3.12 (left plot) shows the distribution of transverse DCA with increasing silicon hits. The right plot is the transverse DCA resolution versus $1/p_T$ as a function of silicon hits. At 1 GeV, the pointing resolution to the interaction point is $\sim$ 220 μm with track hits on all four silicon layers. Requiring hits on all layers of the SVT and SSD improves the DCA resolution by a factor of 15 compared to tracking only by the TPC. Figure 3.4 gives DCA resolution with increasing SiliconHit requirement.

We used a cut on on the number of silicon hits based on their hit position. We required silicon hits (SSD+SVT) of selected tracks to be ≥ 2. When the number of silicon hits is two then the first hit should be on the first layer of SVT, in other cases

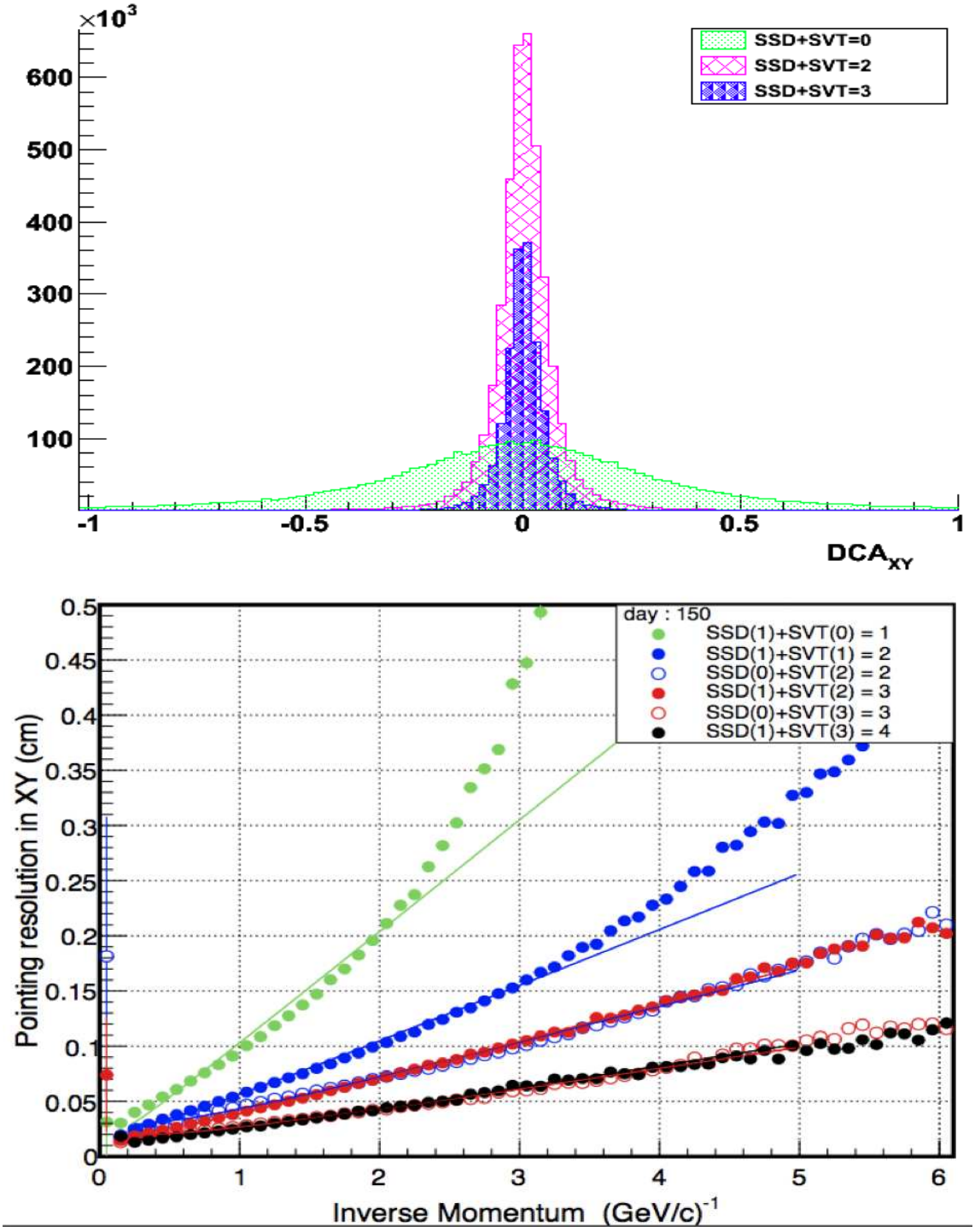

Figure 3.12: Transverse DCA and DCA resolution with increasing silicon hits

SiliconHits	σ_{XY} at 1Gev/c (μm)	σ_Z at 1Gev/c (μm)
0 - (TPC only)	3327	2918
1 - (TPC+SSD)	957	1528
2 - (TPC+SSD+SVT)	382	540
3 - (TPC+SSD+SVT)	296	383
4 - (TPC+SSD+SVT)	280	344

Table 3.4: Transverse DCA resolution with number of silicon points fitted to track. Values are taken from [70]

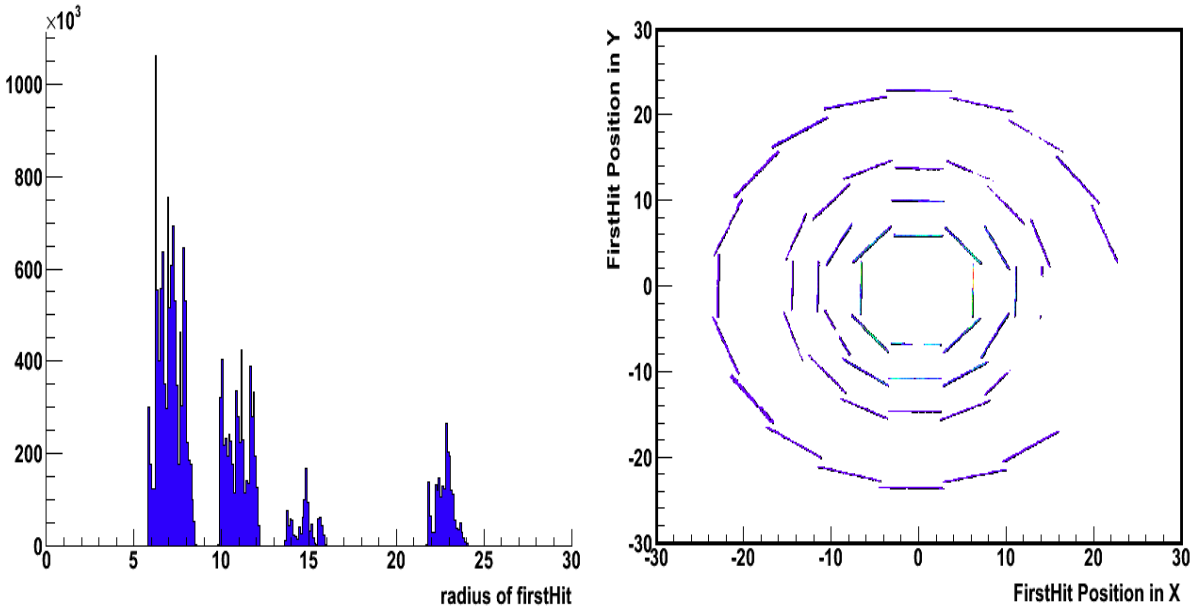

Figure 3.13: Radius of first hit of tracks

(SiHits > 2) the first hit can be on the first or second layer of SVT. By requiring the first hit to be on the first layer of SVT, tracks with two silicon hits will get the necessary resolution. In the latter case (for SiHits >2) the hit position cut helps to avoid counting hits on overlapping layers. In Fig. 3.13 the left plot shows the distribution of the radius of the first hit and the right plot shows the first hit in the transverse plane of the global tracks. The plots clearly reflect the three SVT layers and the SSD layer and their dead ladders.

3.3.6 Particle Identification

Particle identification in STAR is achieved via measurements of energy loss due to specific ionization of charged particles passing the TPC gas. The dE/dx when plotted versus rigidity ($p.q$), which is the product of momentum (p) and charge (q) of the tracks, separates the tracks into several bands, depending on the particle mass. The energy loss for a given charged-particle track is calculated using the "truncated mean" method. Hits with the top 30% values are discarded and an average of dE/dx value from the rest of the hits is derived for that track. STAR uses the Bichsel parametrization [71] for dE/dx approximation for all momentum ranges. The Bichsel parametrization takes into account the path length of the given particle and it provides a reasonable description of the band center and the spread of dE/dx points. Cuts are applied on the standard deviation (Nσ) from the centroid of the band:

$$N_\sigma = ln\Big[\frac{dE/dx_{\text{measured}}}{dE/dx_{\text{expected}}}\Big]\frac{\sqrt{N}}{A}$$

where N is the number of dE/dx points and A is known as the fractional resolution for tracks with a single dE/dx point. For a sample of pions, the distribution of N_σ is gaussian, and the area between $\pm N_\sigma$ corresponds to 68.3% of the total integral and

$\pm 2N_\sigma$ corresponds to 95.4% etc.

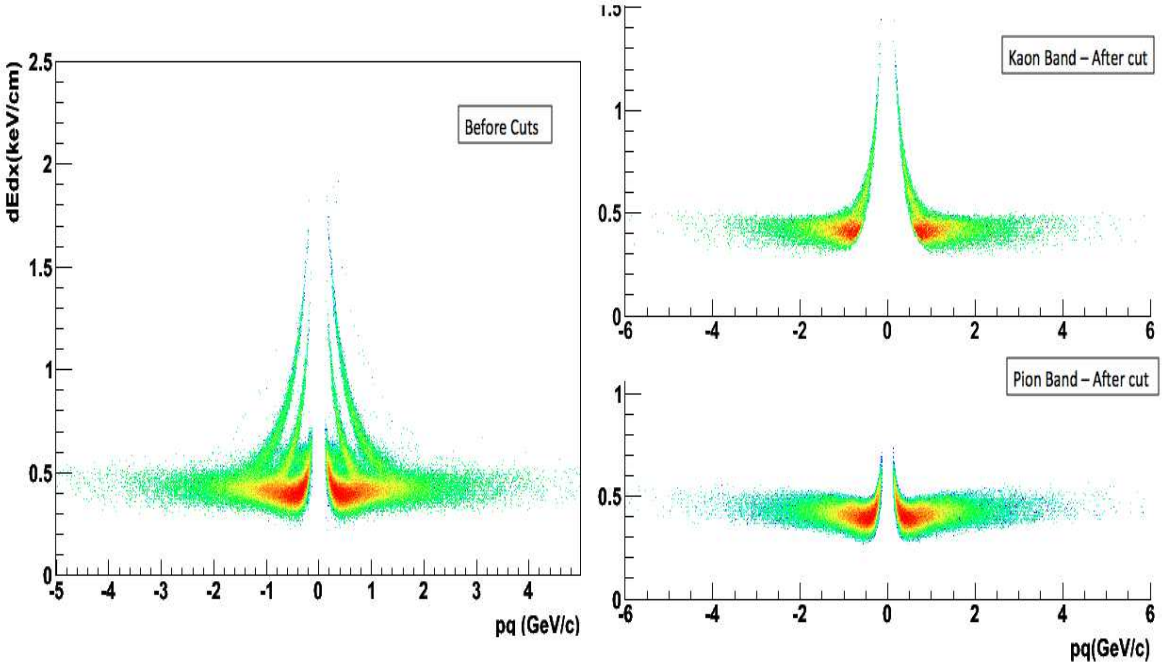

Figure 3.14: dE/dx Vs rigidity $(p.q)$ before and after the cuts

Figure 3.14 is the $dEdx$ vs $p.q$ in Run - 7 Au-Au data. The left plot is without any cuts and the right plots are after a cut of $|N\sigma| < 2.5$ is applied. Above $\sim$ 0.7 GeV/c the kaon-pion bands overlap. This leads to misidentification of kaon and pion tracks where a kaon could be identified as a pion and vice versa. In other words, at intermediate momenta a K^- can be misidentified as a π^- and a π^+ can be misidentified as a K^+. Therefore a $D^0(K^-\pi^+)$ can be identified as a $\bar{D^0}(K^+\pi^-)$. This is termed as $D^0/\bar{D^0}$ cross-feed. In above mentioned scenario, a D^0 can contribute to the $\bar{D^0}$ mass window and can cause a pseudo-enhancement of the signal and vice versa for $\bar{D^0}$. The cross-feed can be reduced with a tighter cut on $|N\sigma|$ of the PID band. Cross-feed reduces with increase in $p_T^{D^0}$. It has a strong dependence on the

kaon opening angle, cos($\theta*$).

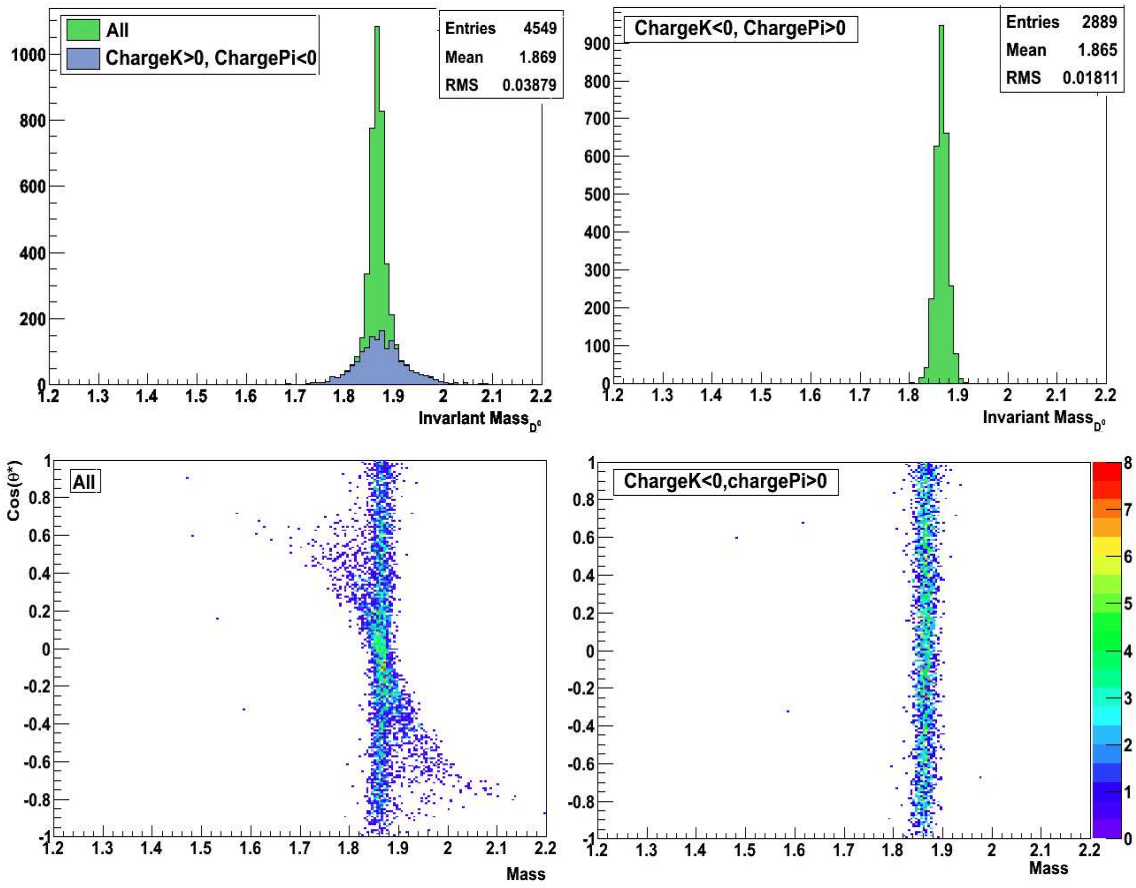

Figure 3.15: $D^0/\bar{D}^0$ cross-feed and its dependence on kaon opening angle

Figure 3.15 upper plots show the invariant mass of reconstructed pureD^0 sample. The contamination from cross-feed is estimated by requiring the charge of kaon to be positive and charge of the pion to be negative. This gives a nonzero contribution of $\bar{D}^0$ particles after reconstruction. The overall contribution from cross-feed in our analysis is estimated to be $\sim 35\%$. The cross-feed accounts for a broadening of the invariant mass peak due to the wrong kinematics from random pairs. By requiring the charge of the kaon to be negative and that of the pion to be positive we get

the plots shown on the right. After selecting the correct signs, the invariant mass resolution improves from $\sim 2\%$ to $\sim 1\%$. Cross-feed has a strong dependence on the kaon opening angle in the CM frame, $\cos(\theta*)$. The bottom plots show the invariant mass plotted vs $\cos(\theta^*)$. As before, by applying a cut on the charge of the tracks we get rid of the tails due to wrong mass values. The pseudo-enhancement and $D^0/\bar{D}^0$ cross-talk will be accepted into systematics.

3.4 Secondary Vertex Reconstruction

Secondary vertex reconstruction is the most crucial part of the analysis. Since the decay of D^0 ($c\tau \sim 123\mu$m) occurs before the tracking detectors, it has to be done using the identified daughter tracks (K and π). As explained in Sec. 3.3.5, with the

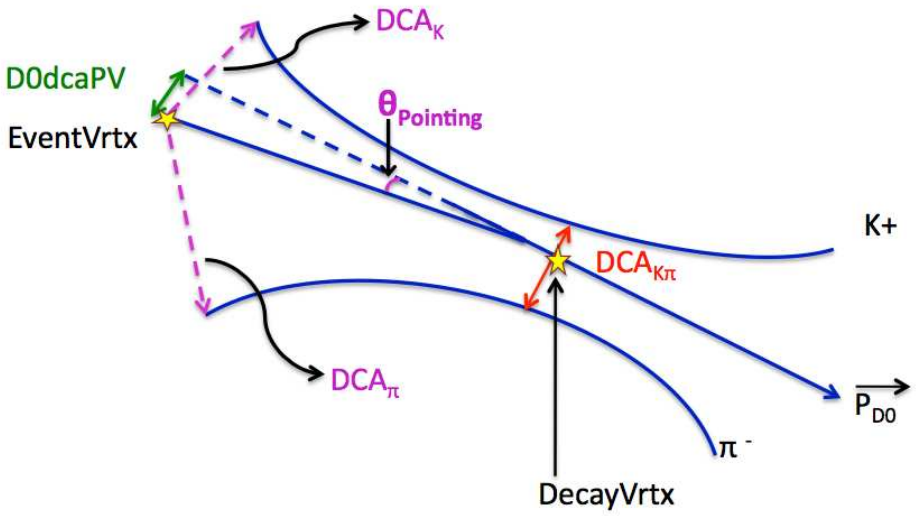

Figure 3.16: D^0 decay topology with TcFit.

increased pointing resolution attained with silicon detectors, the DCA of daughter

tracks to the primary vertex (DCA_K and DCA_π in Fig. 3.16) is known. We do a selection by cutting on this variable. A cut on transverse DCA (DCA_{XY}) < 0.2 cm is used in the macro as a clean-up cut, which allows us to remove some uncorrelated track pairs. The next step involves locating the decay vertex. To do this, the point of closest approach of the track pairs has to be found. The distance between track pairs at their point of closest approach is marked as $DCA_{K\pi}$ in Fig. 3.16. The center point of this distance ($DCA_{K\pi}$) is considered as the decay vertex of the D^0 particle. With the information of decay vertex, we can calculate the various decay parameters associated with the particle and build the D^0 candidate.

In order to have a precision secondary vertexing we need full track information with covariance/error matrix and track information very close to the interaction vertex. Starting from Run-7 the MuDst files have track information inside the beam pipe saved in the StDcaGeometry structure.

3.4.1 StDcaGeometry

At the level of global tracks we have no information about the event vertex. The "traditional" tracking involved extrapolation of global tracks to the DCA of the first hit. But a "new" tracking method involves finding the global tracks and moving them through all material to the beam pipe center $(x,y)= (0,0)$, to obtain full track information. This full track/error information is saved as DcaGeometry. While moving the tracks, in order to account for all the dead materials from the inner field cage (IFC), SSD, SVT, beam pipe etc., a Kalman Filter machinery (see Appendix A) is run with StTracks. It can account for the multiple Coulomb scattering (MCS) as the tracks pass through the detector layers. It also ensures that helix manipulation is correct. A geometrical representation of the tracking with StDcaGeometry is shown

in the left plot of Figure 3.17, whereas the right plot shows the difference between the p_T measured at the first hit and p_T obtained using StDcaGeometry of the global track for various track hit requirements.

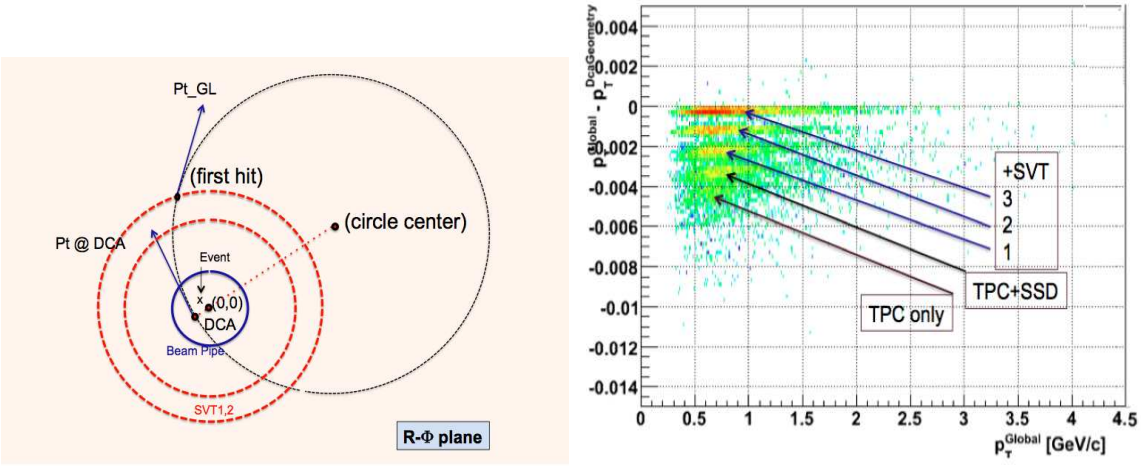

Figure 3.17: Schematic of DcaGeometry tracking (left) and performance (right) showing the difference in p_T measured between global and DcaGeometry as a function of p_T and silicon hits.

The plot on the right shows that there is a finite difference between the p_T measured at the first hit and in the DcaGeometry, especially at the lower momenta. The "new" tracking reduces the errors of low p_T tracks. As seen from the figure, an increase in the number of silicon hits improves the p_T measured at the hits and therefore the difference gets smaller. One should keep in mind that an accurate measurement of p_T is important since the invariant mass of the parent is calculated from knowledge of the p_T of the tracks and thus, can improve the mass resolution.

We investigated three methods for secondary vertex reconstruction. The first method uses the global track information from the first measured hit position, finds the vertex and does a fit with the associated primary track. The second and third

methods use DcaGeometry for secondary vertex searches. The three approaches are described below:

1. A linear fit approach. Using global track information, two tracks and parent are fitted with a linear fit function.

2. A helix swimming method to the DCA of the two track helices (like V0 finder). This can be done with global track parameters as well as DcaGeometry to reconstruct the helices.

3. A full helix fit by using the information from the second method and using the DcaGeometry full track/error information.

The first method does not take into account the B field and hence it fits straight lines to the two daughter tracks and to the parent. This leads to a poor approximation, especially if the first hit is in the outer layers of the TPC. The vertex position found in this case could be too far from real vertex. This method was abandoned. The second and third methods were investigated more using Monte Carlo data. The third method gives a better estimate and it was used in this analysis for secondary vertex finding.

3.4.2 Helix Swimming Methods

This method uses a V0-like tracking [72], where oppositely charged identified particle tracks are paired and they are projected towards the primary collision vertex[7]. If the two trajectories cross at some point before the primary vertex, they are considered as daughter candidates of the D^0 decay. During this initial process, loose cuts

[7]To find the crossing point, the tangent of each helix is taken, and the intersection of these two lines are found, since the helices cannot cross each other

are applied to reduce the background. For example, we cut on the distance of closest approach (DCA) of the V0-parent to the primary vertex. This can help remove fake V0 candidates that do not point back to the primary vertex. The helix swimming method was tested with global tracks as well as DcaGeometry. A performance comparison of the approaches is given in Fig. 3.18.

3.4.3 Full Fit to the Decay Chain with Kalman Filter (TCFIT)

The third method combines the information from helix swimming method to a full D^0 vertex fit (TCFIT). This method was used in our analysis. Figure 3.16 shows the D^0 decay topology with constrained TCFIT. The method uses a least squares fit of the decay vertex [73]. We used the track parameters and information from DcaGeometry saved in the MuDst files. The V0-like helix swimming methods gives an initial estimate of the decay vertex position. This track information and knowledge from helix swimming methods permits a fit to kaon and pion tracks, with the constraint that they are coming from a common point. In other words, the reconstructed momentum of the D^0 ($\mathbf{P_{D^0}}$) should point back to the event vertex. The solution to the fit is the value that minimizes the total χ^2. For a measurement constraint F, the χ^2 takes the form,

$$\chi^2 = \sum (y_{i0} - y_i(x^*))^T V^{-1} (y_{i0} - y_i(x^*)) + F, \tag{3.6}$$

where the y_{i0} are the measured track parameters (e.g., helix parameters), y_i are the track parameters after refit with knowledge of secondary vertex. V is the covariance matrix of the measured track parameters. The constraint F ($\propto f\Lambda$) is added to the total χ^2 via the Lagrange multiplier λ. The minimum of χ^2 is then calculated with respect to fit parameters with the condition $\delta\chi^2/\delta\lambda = 0$, imposed for minimization.

The fit method calculates and updates the initial estimates of decay length and its uncertainty obtained using the helix swimming method. The probability and χ^2 of the fit is also saved in the output.

3.4.4 Comparison of Secondary Vertexing Methods

Figure 3.18 shows a comparison of the performance of three methods used for secondary vertexing using a pure sample of D^0 events. The plots show the correlation

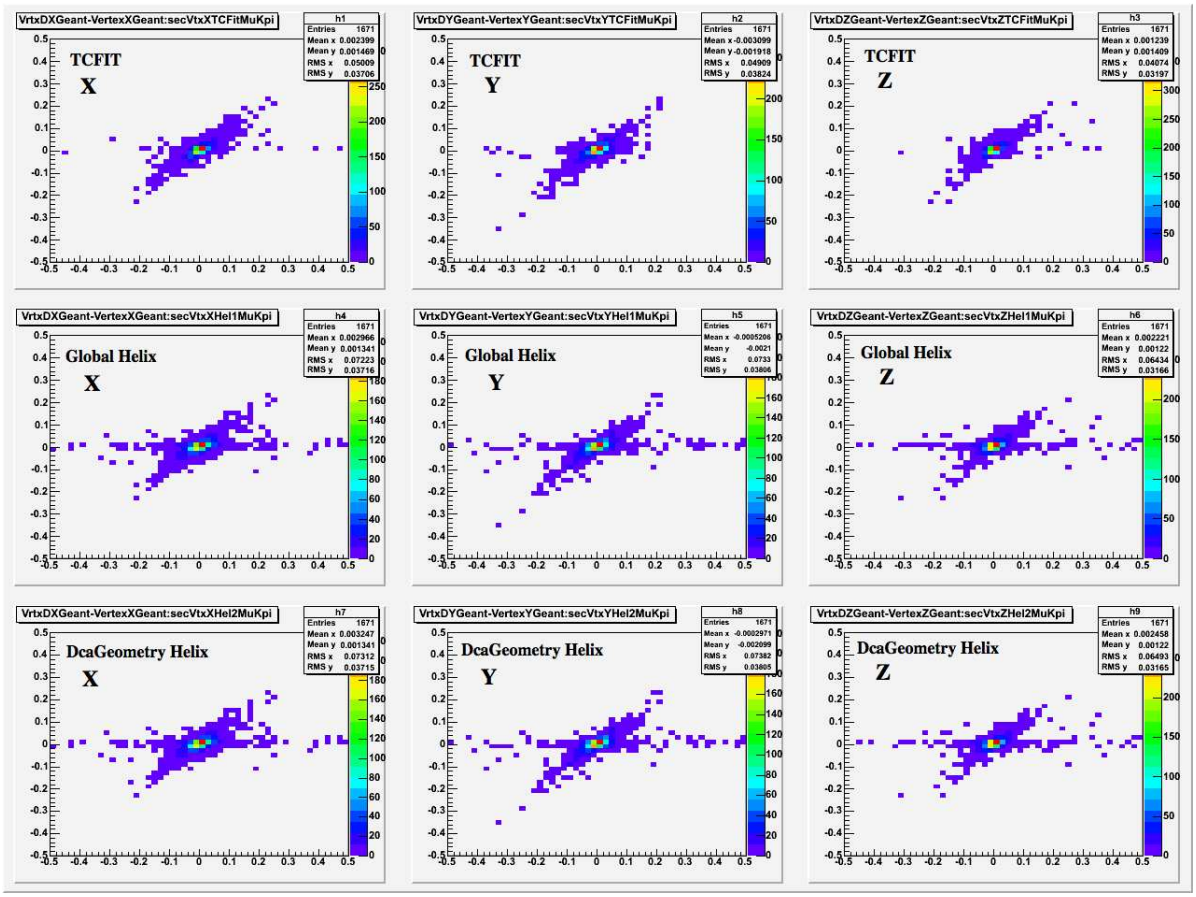

Figure 3.18: Correlation between reconstructed and GEANT decay vertex coordinates shown for the fit method (top row) and Helix swimming method using global track (middle row) and DcaGeometry (bottom row) parameters.

of the reconstructed decay vertex position with the corresponding input value from a

GEANT file for x, y and z coordinates.

As can be seen from the figure, the TCFIT[8] method gives a better correlation. The horizontal band on the plots (more evident for the helix methods) turns out to be the low momentum D^0s. The low momentum D^0 daughters decays back-to-back and the parallelism of the tracks causes poor resolution. We can exploit the back-to-back correlation between daughter tracks to find signals in the low momentum region.

3.5 Reconstructed Parameters

After applying cuts at the event and track levels and particle ID cuts from dE/dx, the D^0 candidate can be built with track candidates that pass the quality cuts. In this section, we will look at the resolution of the microvertex code reconstructed parameters.

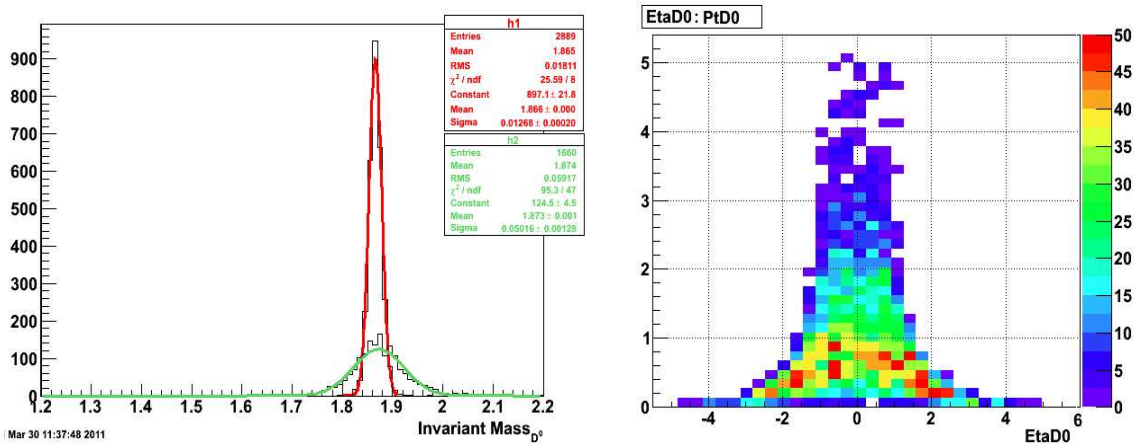

Figure 3.19: Reconstructed D^0 invariant mass shown with cross feed (left) and p_T versus η of the D^0 (right)

Figure 3.19 shows the reconstructed D^0 parameters when using pure D^0 (signal)

[8]TcFit uses numerical derivatives, which takes time. An estimate of the TcFit benchmark - With Tcfit a single file (with 302 events) takes about two hours, while without TcFit it takes less than a minute.

events. The left plot shows reconstructed invariant mass for $D^0(K^-\pi^+)$ with cross-feed separated (green histogram). The true pairs gives a mean value of 1.865 GeV/c^2, corresponding to the D^0 mass, the gaussian fit to this gives a width of ∼13 MeV. The resolution after the fit is ∼ 0.7%. The reconstructed p_T vs η plot shows distributions that are in agreement with the input parameters.

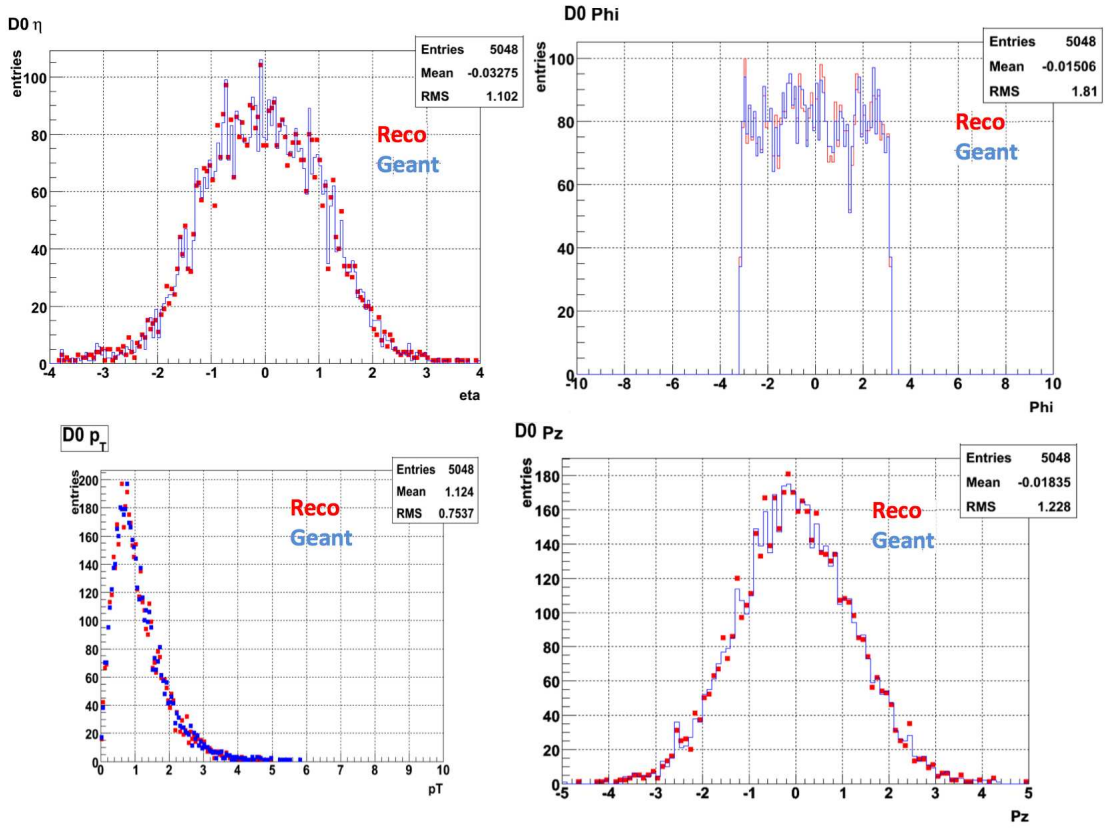

Figure 3.20: Various reconstructed D^0 parameters and corresponding input values

In order to find the resolution of the reconstructed parameters, such as η, ϕ, p_z etc. we used .minimc files[9]. The good D^0 daughter candidates were found from

[9]StAssociation maker is used for association of StMcEvent and StEvent, the resulting files are saved as .minimc.root files. which contain the matched pair information

.minimc.root files using the matched pair information. These good daughters were selected and used to reconstruct the D^0s using the microvertexing code. In the next step, the input (original) D^0 parameters for the same daughter candidates were extracted from the .geant.root files. The distribution from the input geant file is then compared with the reconstructed parameter. Figure 3.20 shows both distributions together.

3.5.1 Microvertexing Variables

Microvertexing involves calculation of the different variables associated with the reconstructed secondary vertex. These variable includes decay length, DCA between daughter tracks, DCA of parent D^0 to the primary vertex etc.

Decay Length: Decay length (dL) is the distance between the primary vertex and decay vertex. It is defined as:

$$dL = \frac{\mathbf{L}.\mathbf{P_{D^0}}}{|\mathbf{P_{D^0}}|} \tag{3.7}$$

where $\mathbf{L}$ is the decay distance measured from primary vertex to decay point and $\mathbf{P_{D^0}}$ is the momentum of the parent D^0. For an ideal decay and detector, $\mathbf{L}.\mathbf{P_{D^0}}$ = LPcos(θ) is a positive number. But the current detector resolution achieved with SVT and SSD is $\sim$ 220-230 μm at 1 GeV (resolution of SSD+SVT). Therefore it is possible that the tracks can meet on the other side of the primary vertex while reconstructing the event. In such cases, the numerator of Eq. (3.7) becomes negative yielding a negative decay length. Figure 3.21 shows a schematic of the two cases.

DCA of D^0 to primary vertex: The distance of closest approach (DCA) of the reconstructed D^0 to the primary vertex ($\mathrm{DCA}^{\mathrm{D}^0}_{\mathrm{PV}}$) is a useful variable. This variable is calculated with the knowledge of the reconstructed momentum of the D^0 particle

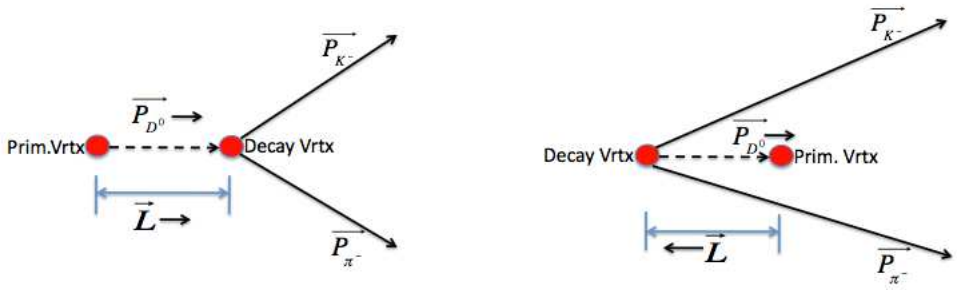

Figure 3.21: Schematic of the signed (positive and negative) decay length scenarios

and the vector connecting the primary vertex and the midpoint of the DCA of tracks obtained from helix swimming. The angle between these two vectors is the pointing angle, θ_{pointing}. For signal events the pointing angle should be ~ 0. As can be seen on Fig. 3.22, the $\text{DCA}^{\text{D}^0}_{\text{PV}}$ variable is calculated using the following relation:

$$\text{DCA}^{\text{D}^0}_{\text{PV}} = \text{dL} * sin(\theta_{\text{pointing}})$$

DCA between daughter tracks: The DCA between tracks ($\text{DCA}_{\text{K}\pi}$) is found by iteration of the track fits and finding the point where they come closest using the TCFIT method. The midpoint of their distance of closest approach is considered to be the decay vertex.

3.5.2 Decay Length and p_T Resolution

The resolution of reconstructed quantities can be studied by using a pure Monte Carlo sample of D^0 events. As described before, we use the matched pair information from minimc files to find the kaon and pion tracks that come from a D^0 particle. There is a tag of these events in the minimc files saved as keys. This key can be used

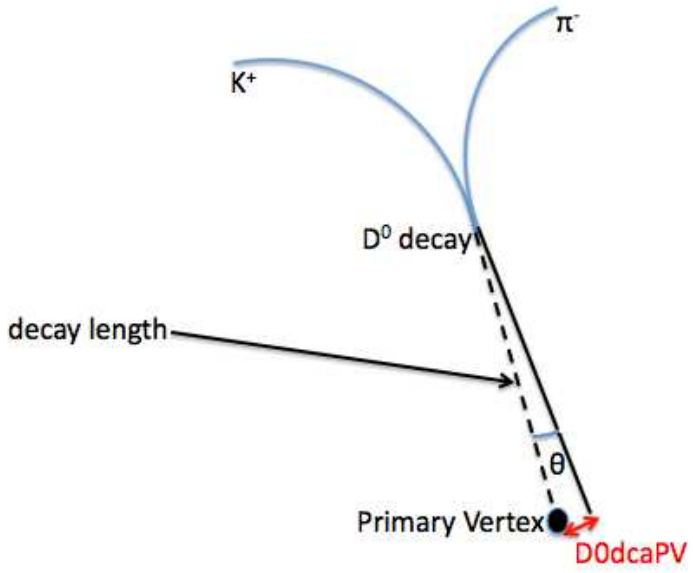

Figure 3.22: D^0 decay showing the DCA of reconstructed D^0 to the primary vertex.

to locate those same events in GEANT and MuDst files. This enables an "apple-to-apple" comparison of the input GEANT values to the code reconstructed value. A plot of the difference between GEANT and reconstructed value of transverse momentum (p_T) shows a sigma of $\sim$ 17.4 MeV. Figure 3.23 shows the difference of p_T between GEANT and reconstructed D^0 as a function of p_T (left), and the p_T resolution plot fitted with a gaussian function (right).

Since D^0 particles decay before they reach the detector layers, a secondary vertex reconstruction method as described in Sec. 3.4.3 is used. It gives a resolution of about 55 μm (x-y direction) in the central region and $\sim$ 25 μm (z direction) when fitted with a double gaussian. The other two methods described in Sec. 3.4.2 (1) using the helix swimming with global track parameters and (2) using the helix swimming with the DcaGeometry give comparably lower resolutions. Figure 3.24 shows the

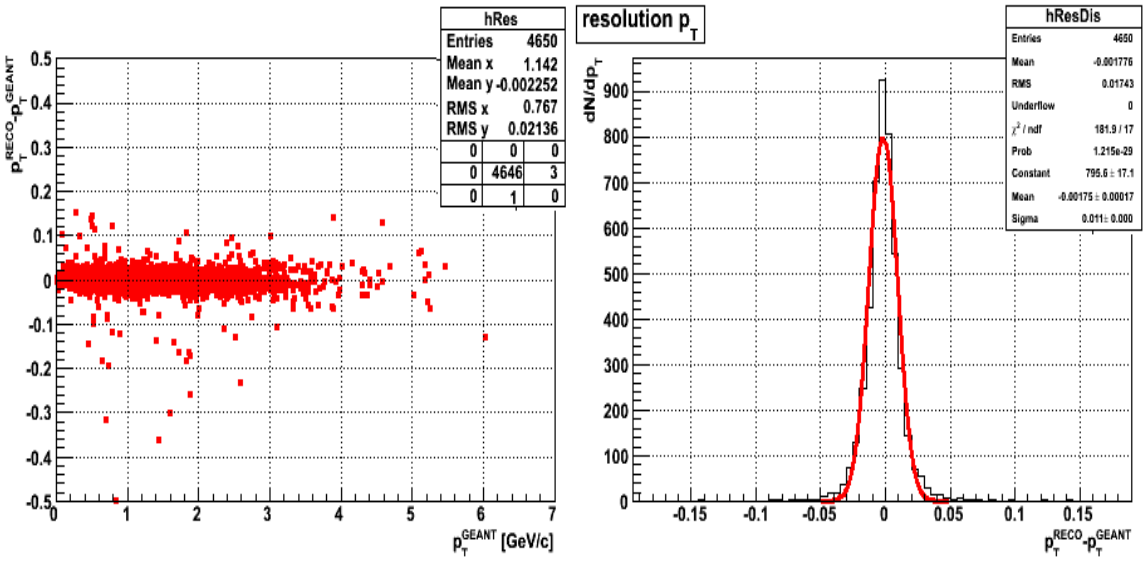

Figure 3.23: Difference between the input p_T from GEANT and reconstructed p_T versus p_T (left). Resolution of reconstructed p_T of the D^0 (right)

decay vertex resolution in the x, y and z directions, of the three secondary vertexing methods we investigated. The plots are fitted with double gaussian functions. The helix swimming methods (middle and bottom rows) gives resolutions of $\sim$ 150 μm (x-y direction) and $\sim$ 135 μm (z direction) respectively by using the helix swimming method with global parameters. When using the DCAGeometry parameters, the values are $\sim$ 140 μm (x-y direction) and $\sim$ 125 μm (z direction) respectively. These values correspond to the gaussian fit of the central region, which corresponds to the high momentum D^0s. Thus, from simulation, more than a factor of two was gained in secondary vertex resolution for the high p_T D^0s with the fit method compared to usual helix swimming methods [76].

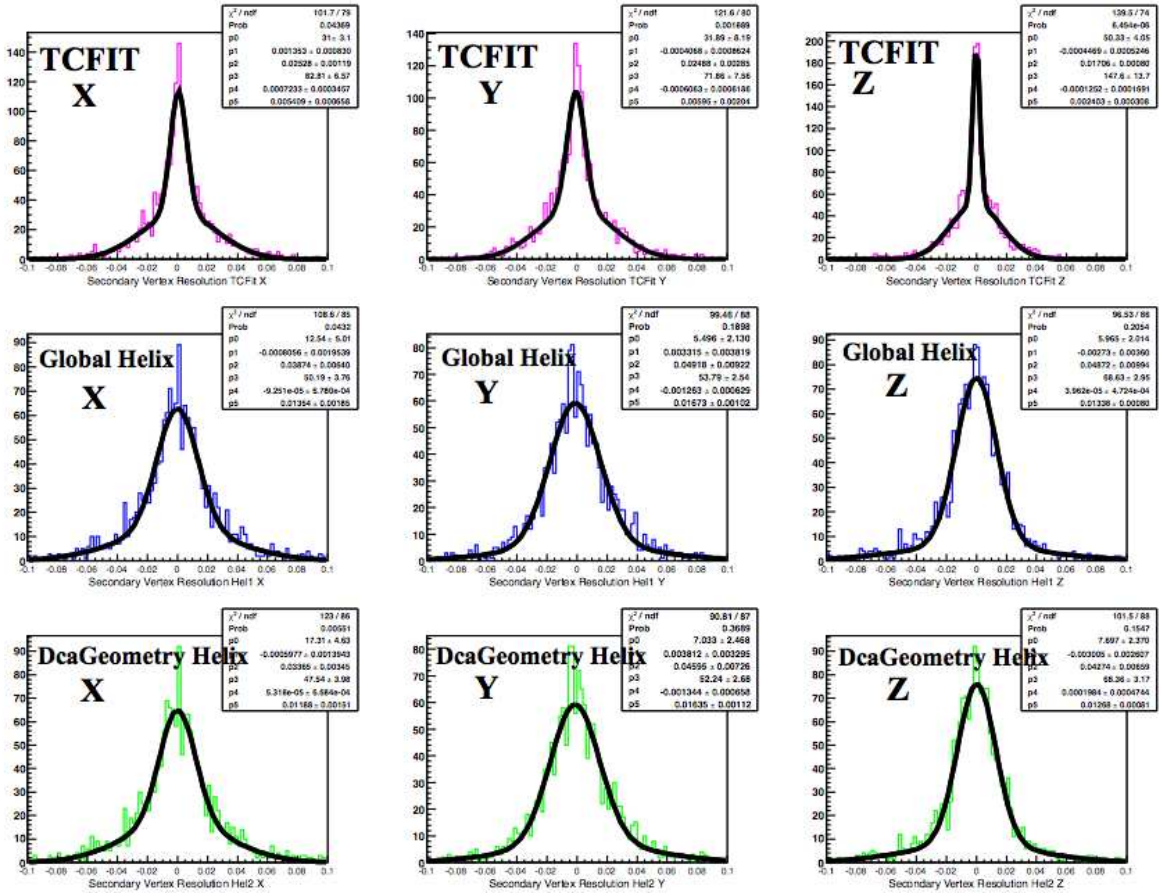

Figure 3.24: Secondary vertex resolution in x, y and z coordinates using the fit method (top row), and helix swimming methods; using global parameters (middle row) and DcaGeometry parameters (bottom row).

3.6 Cut Optimization

Optimization of offline cuts was done using a Monte Carlo sample of D^0s to get the signal behavior and these signal events were mixed with central HIJING Au+Au events to study the background behavior. The various secondary vertex parameters, decay length, DCA between the daughters, parent DCA to primary vertex etc. and correlation of cut variables can be studies and optimized in this way. A proper cut on these variables can improve the effective signal significantly. I will discuss the signal and background behavior of these parameters and possible cut values in the following section.

3.6.1 Signal/Background Distribution

Decay length significance: Decay length significance is the ratio of the decay length (**dL**) to the error (σ_{dL}) associated with it, $\frac{\mathbf{dL}}{\sigma_{dL}}$. A cut on this variable is more appropriate than any hard cuts on the decay length since decay length depends on the momentum. For signal events we expect an excess on the positive side of the decay length distribution compared with the negative side due to the presence of long lived decays.

Figure 3.25 shows the signal (left) and background (right) behavior of the variable. The signal distribution clearly shows an excess on the positive side, whereas the background shows no such bias. This makes it an ideal cut variable. The cut values are be determined by looking at the significance distribution ($S/\sqrt{S+B}$) and selecting the highest significance region.

D^0 DCA to Primary Vertex ($\mathrm{DCA}^{\mathrm{D}^0}_{\mathrm{PV}}$): As described before, this variable is calculated using the trigonometric relation of the decay length to the pointing

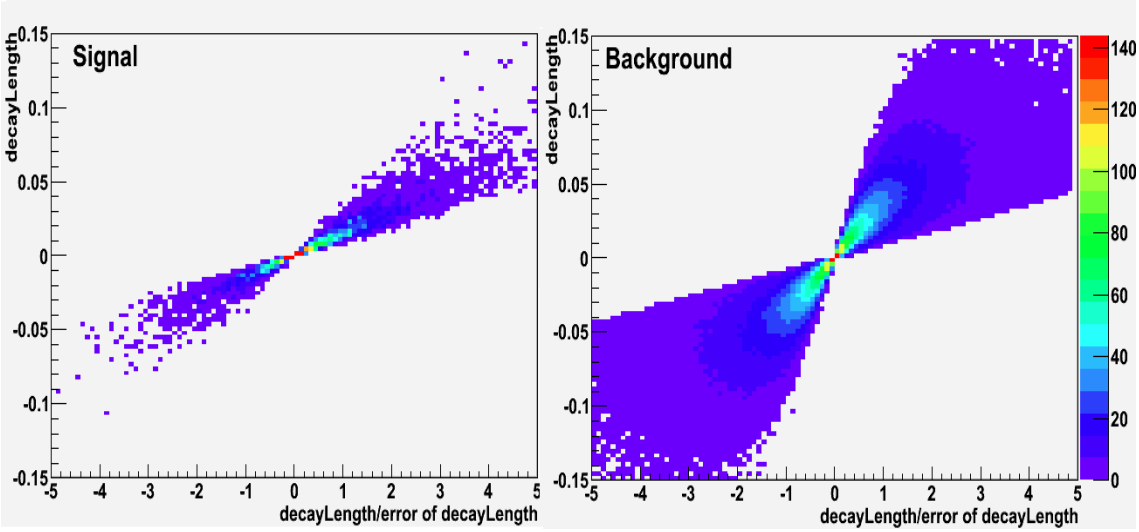

Figure 3.25: Signal and background behavior - decay length (dL) vs $\frac{dL}{\sigma_{dL}}$.

angle. The signal and background distributions are shown in Fig. 3.26. The signal distribution shows a similar trend like decay length - an excess in the positive side. A discussion of the significance distribution and cut selection is in the next section.

Decay Length Significance of Daughter Tracks: The idea of decay length significance as defined above can be extended to the decay of kaon and pion daughter tracks as well. We defined a variable, which is the ratio of decay distance of the daughter tracks from the secondary vertex of the D^0 to the error on this decay distance. A plot of this variable versus p_T of the track is shown in Fig. 3.27 for kaons, both for signal and background events. The pion distribution (not shown here) exhibits a similar trend.

The signal and background plots shows differences in their behavior, the signal shows an excess in the positive side and it becomes more positive as the momentum of the tracks increases.

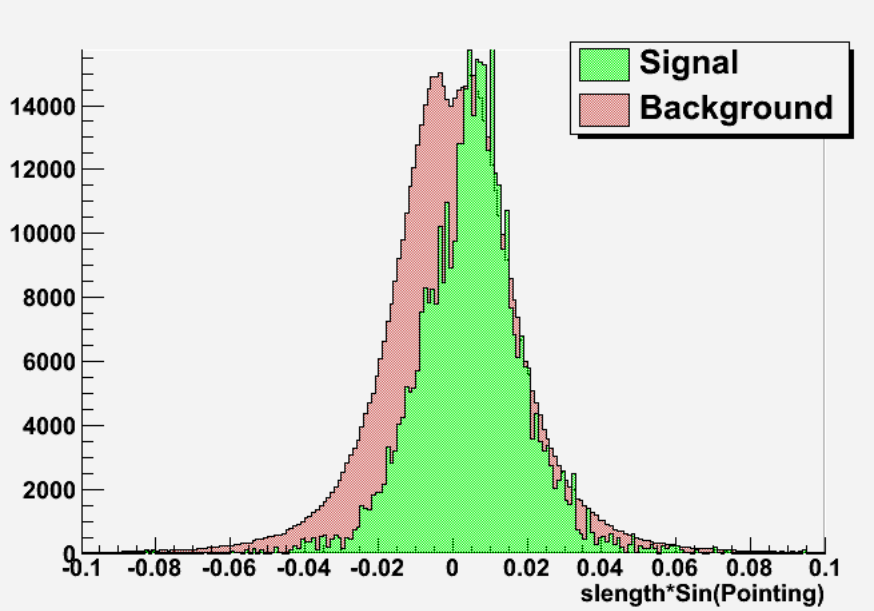

Figure 3.26: Signal and background behavior - DCA of reconstructed D^0 to PV

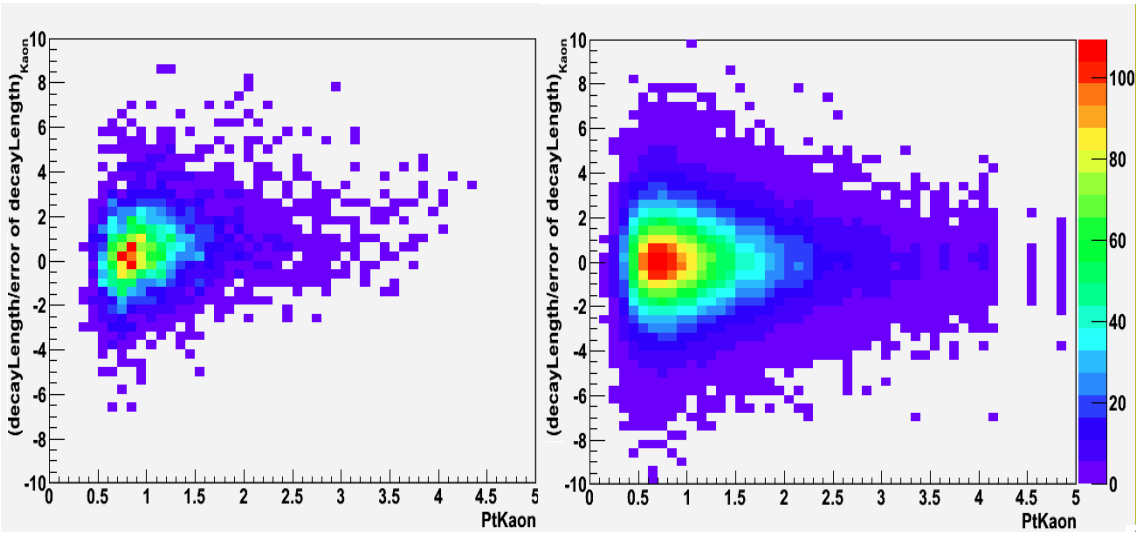

Figure 3.27: Signal and Background Behavior - Kaon decayLength significance

3.6.2 Significance Distribution

The ratio of signal to $\sqrt{B}$ distribution of the above-described variables are shown in Fig. 3.28. A graphical selection of the highest significance region can be tried with the graphical cut class (TCutG) in ROOT. It allows us to see what cut values can yield a better significance of the signal. The plots in Fig. 3.28 were made by taking the ratio of signal to $\sqrt{B}$ distribution.

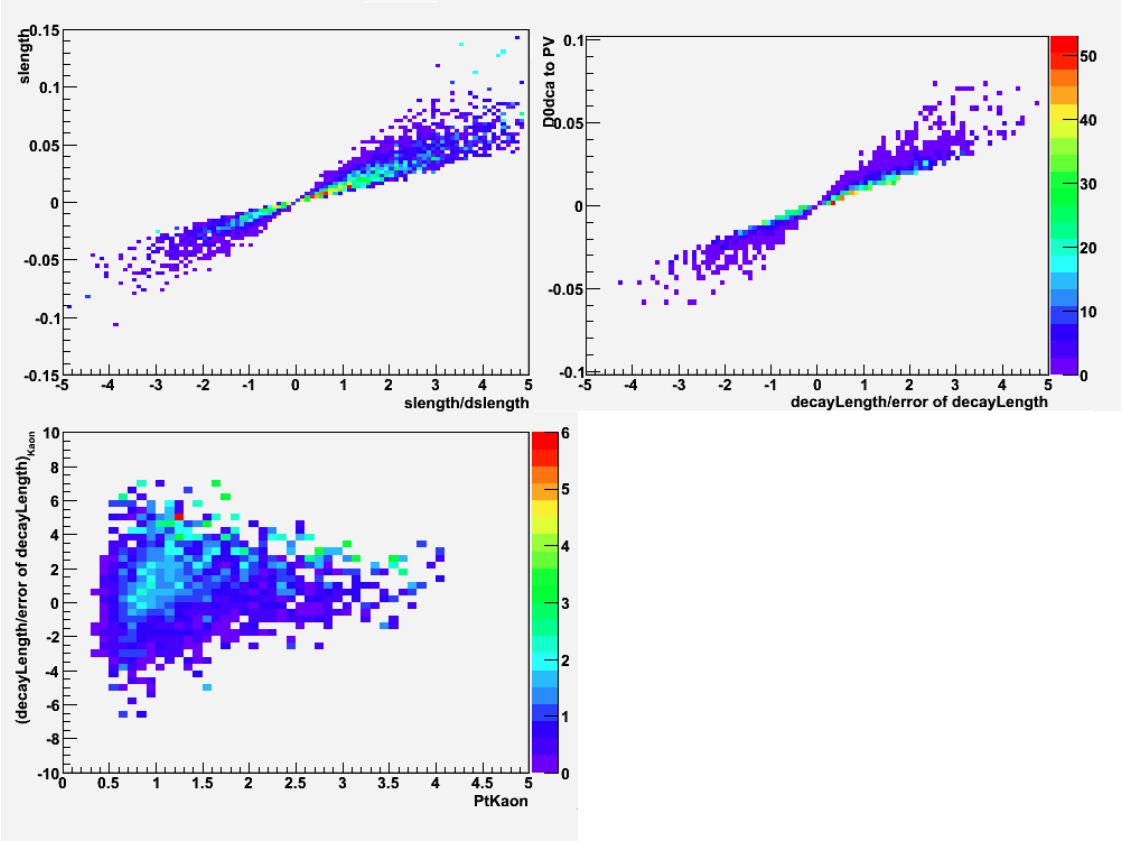

Figure 3.28: Significance distribution of cut variables

3.6.3 Signal Extraction using Multivariate Analysis (TMVA)

When searching for weak/rare signals, it is essential to extract the maximum available information from the data. The Toolkit for MultiVariate Analysis (TMVA) is a

ROOT integrated machine learning technique for the processing and parallel evaluation of multivariate classification and regression techniques. Advanced discrimination methods using all the information for optimal background reduction such as correlation of the input variables in signal and background are available in the TMVA.

Compared to a cut-based selection, a multivariate selection may allow us to have a higher signal efficiency for the same background rejection. It uses various classifiers to discriminate signal from background and it provides a framework for training, testing and performances evaluation of classification methods [74].. The classifiers include but are not limited to: rectangular cut optimization, projective likelihood estimation (PDE approach), linear discriminant analysis (H-matrix, Fisher and linear (LD) discriminants) to more complex nonlinear approximations (boosted/bagged decision trees (BDT), Multi-Layer Perception (MLP) etc.). Training samples for signal and background have to be provided to the TMVA. The training sample we used for signal is pure D^0 using a powerlaw p_T distribution, and background used is HIJING Au+Au central events. Both data sets were processed with the microvertexing macro and the resulting output tree structure is provided as input training samples.

The upper panel of Fig. 3.29, shows the normalized distributions of signal and background training sample variables. The correlation between variables used in the signal sample is given in the lower panel of Fig. 3.29. The correlation matrix shows the dependence of various parameters and it tells us how one cut affects the other. A Correlation of 0 means that the variables are independent, whereas a correlation of 100% means that they are totally correlated and some are anti-correlated.

We tried several different classifiers including, Fisher, BDT and MLP classifiers for training. The classifier output gives a unique value to each $K\pi$ pair. Cutting on

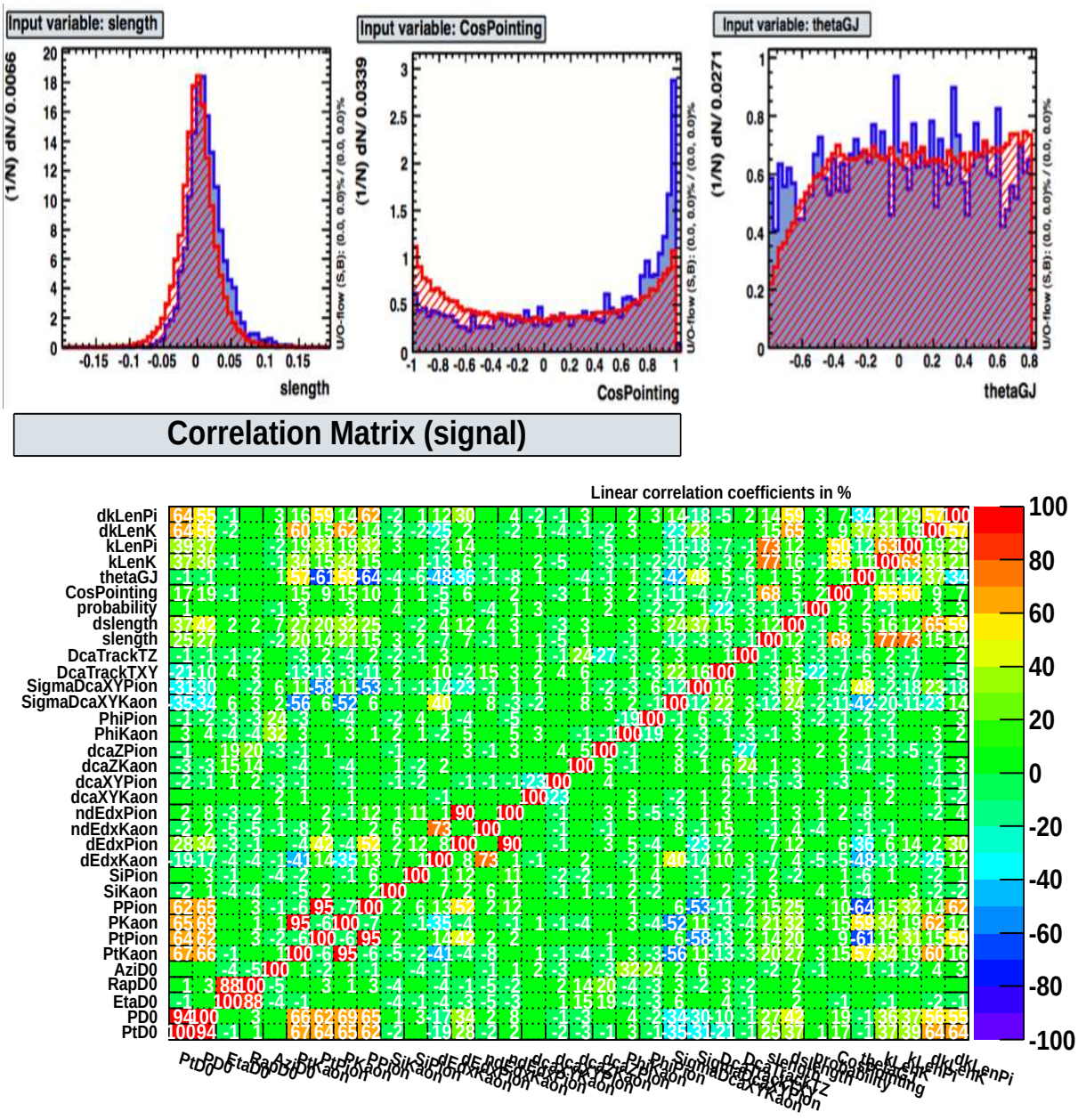

Figure 3.29: Upper panel: normalized distributions of signal/background variables. Lower panel: correlation matrix for signal sample

this classifier value is equivalent to cutting on multiple variables at the same time. Therefore, using such a cut should increase the purity and decrease the background. During the training phase, weight files are created, which contain the normalized distributions of signal and background training samples and the correlation of the variables. After the training phase a testing sample is provided to evaluate the performance of the classifier. Application of the classifier cuts and invariant-mass plots from Monte Carlo embedding and real data is presented in Chapter 4.

3.7 Application to Data

During the initial D^0 reconstruction phase, loose cuts were applied in the microvertexing code to reduce the background while maximizing the signal candidates. Once the candidate pool was assembled, more stringent cuts were applied to maximize the signal to background ratio. Table 3.5 gives the cuts applied in the code for processing the 2007 Au+Au dataset.

3.7.1 Cut Sets

Results from this first production[10] gave us preliminary results on D^0 and $\bar{D^0}$. The good events, which satisfied the vertex position and resolution cuts were about $\sim$ 24 million in real data in first production. The results are presented in Chapter 4. However, the cuts in first production (given in Tab. 3.5) needed optimization and we wanted to save all charge combinations for studying the systematics. Therefore, a second production was done with fine-tuned cuts (given in Tab. 3.6). Moreover, the second production saved event plane information and azimuthal angle of the D^0 candidate for calculation of elliptic flow (v_2). Thus, the second production presents

[10]production here stands for running the code over the dataset

Cut Level	Cut Parameter	Cut Value
Event Level	Trigger Ids	200001, 200003, 200013
	$\|V_z\|$	< 10 cm
	$\|\sigma V_z\|$	$< 200\mu$ m
Track Level	Number of Silicon Hits (SSD+SVT)	> 2
	Momentum of tracks (p)	> 0.5 GeV/c
	Pseudorapidity, $\|\eta\|$	< 1.0
	Number of fitted TpcHits	> 20
	dE/dx TrackLength	> 40 cm
	DCA to Primary Vertex (DCA_{XY})	< 0.1 cm
	ChargeKaon*ChargePion	< 0
Decay Fit Level	Probability of Fit	> 0.1
	|decay length|	< 0.1 cm
Particle Id (dE/dx)	$\|N\sigma_K\|$	< 2
	$\|N\sigma_\pi\|$	< 2

Table 3.5: Cuts applied for D^0 reconstruction in Run-7 Au-Au dataset at $\sqrt{s_{NN}} = 200$ GeV(first production).

a more complete and powerful dataset for this analysis.

Table 3.6 gives a summary of the cuts applied at various levels for D^0 reconstruction. The cut highlights of the second production are that only triggered events were selected, the cut on individual track momenta was modified to a cut on the sum of the daughter momenta to preserve the phase space of the candidate better, the logic and minimum requirement on the number of silicon hits was modified, etc. These cuts were first tested on Monte Carlo data. The number of events after cuts in second production was $\sim$ 28 million in 2007 Au+Au data.

The run was organized such that the code gives an output for each day. These files were combined and subjected to more cuts in order to further clean up the sample and to do analysis faster and easier. These cuts we refer to as pico cuts. Table 3.7 gives the pico cuts used for the two productions.

Cut Level	Cut Parameter	Cut Value
Event Level	Trigger Ids	200001, 200003, 200013
	$\|V_z\|$	< 10 cm
	$\|\sigma V_z\|$	$< 200\mu$ m
	vertex index	0 (best vertex only)
Track Level	Number of Silicon Hits (SSD+SVT)	> 1
	Radius of first hit on Track	< 9 cm if SiHits $= 2$, < 13 cm else
	SVTHits (SVT), SsdHits (SSD)	SVT < 4, SSD < 2
	Momentum of tracks ($p_K + p_\pi$)	> 1.5 GeV/c
	Pseudorapidity ($\|\eta\|$)	< 1.2
	Number of TpcHits fitted	> 25
	Ratio of TpcHits Fitted/Possible	> 0.51
	dE/dx TrackLength	> 40 cm
	DCA to Primary Vertex (DCA_{XY})	< 0.2 cm
D^0 Level	D^0 Rapidity ($\|y_{D0}\|$)	< 1
	$\|\cos(\theta^*)\|$	< 0.8
	Mass$_{D^0}$	1.2 to 2.2
Decay Fit Level	Probability of Fit	> 0.05
	|decay length|	< 0.2 cm
	error of decay length	< 0.1
Particle Id (dE/dx)	$\|N\sigma_K\|$	< 2.5
	$\|N\sigma_\pi\|$	< 2.5

Table 3.6: Cuts applied for D^0 reconstruction in Run-7 Au-Au Dataset at $\sqrt{S_{NN}} = 200GeV$ (second production).

Production	Cut Parameter	Cut Value
first production	$\|\cos(\theta^*)\|$	< 0.6
	$\|\eta_{D^0}\|$	< 1.85
second production	$\|\cos(\theta^*)\|$	< 0.6
	$\|\eta_{D^0}\|$	< 1.85
	D^0 Rapidity($\|y_{D^0}\|$)	< 0.5
	Probability of fit	> 0.1
	Number of silicon hits	> 2
	Transverse DCA to PV (DCA_{XY})	< 0.1
	Particle ID ($\|N\sigma_K\|$,$\|N\sigma_\pi\|$)	< 2.0

Table 3.7: Cuts applied at pico file level for first and second production.

Chapter 4

Results and Physics Discussion

This chapter mainly focuses on the analysis results and the related physics. Invariant-mass peaks from the 2007 Au+Au dataset will be presented for different cut sets and for various centralities. I also present $\bar{D}^0/D^0$ ratio and raw yield for various p_T bins. Results from two productions[1] will be discussed. As a proof of principle, the analysis is extended to reconstruction of strange particles using the secondary vertex fit method. The uncorrected p_T spectra of K^0_s will also be presented for two different centralities.

4.1 Results from First Production

The results from the two production runs explained in Sec. 3.7 will be presented here. The two productions are different in terms of cut values and logic. An event can have several vertices. The first production used all vertices in a given event. However, we only need the best ranked (highest) vertex in a given event, therefore, the correlation between the rank of the event vertex to the multiplicity (gRefMult) can be used for an offline cut. The best vertices are the highest multiplicity ones. From Fig. 4.1, the cut gRefMult > 50 can be used to select the best vertex. This cut on gRefMult is included in all offline cut sets from first production unless otherwise specified. The first production used the cuts given in Table 3.5 and the pico cuts given in Table 3.7.

[1]Two different cuts sets ran over the data set

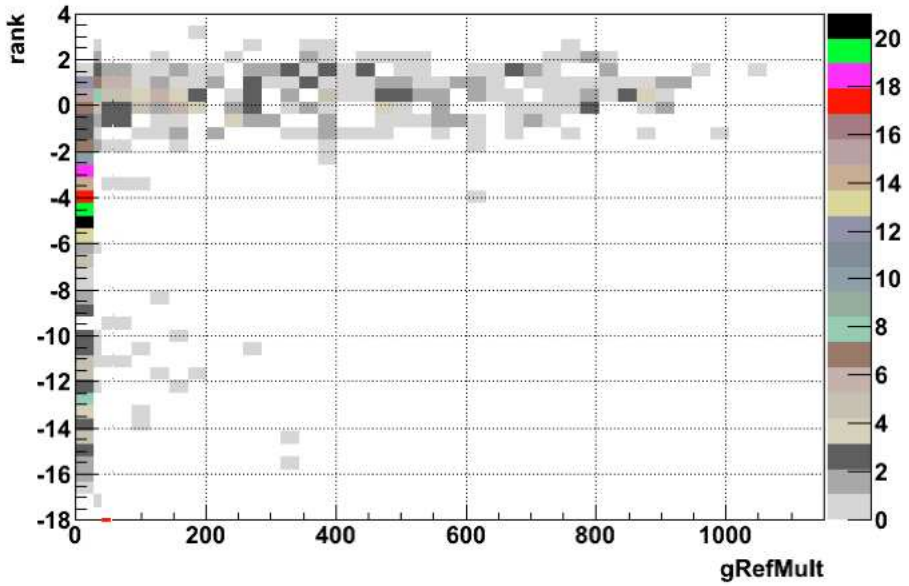

Figure 4.1: Correlation between rank of a vertex and multiplicity

4.1.1 Invariant-Mass Peaks

The invariant-mass plots of D^0 and $\bar{D^0}$ for various offline cut sets are presented in this section. Due to the presence of huge combinatorial background in this analysis, the $D^0(\bar{D^0})$ signal, which appears as a peak in the invariant-mass distribution is not always visible before some form of background subtraction. The distributions before and after background subtraction will be presented along with the method we used for background estimation.

CutSet 1: 50 μm $<$ | decay length| $<$ 400 μm

|DCA of D^0 to PV| $<$ 300 μm, $DCA_{K\pi} < 200\mu$m

|Rapidity of D^0| $<$ 0.5, Track momenta $>$ 0.7 GeV/c

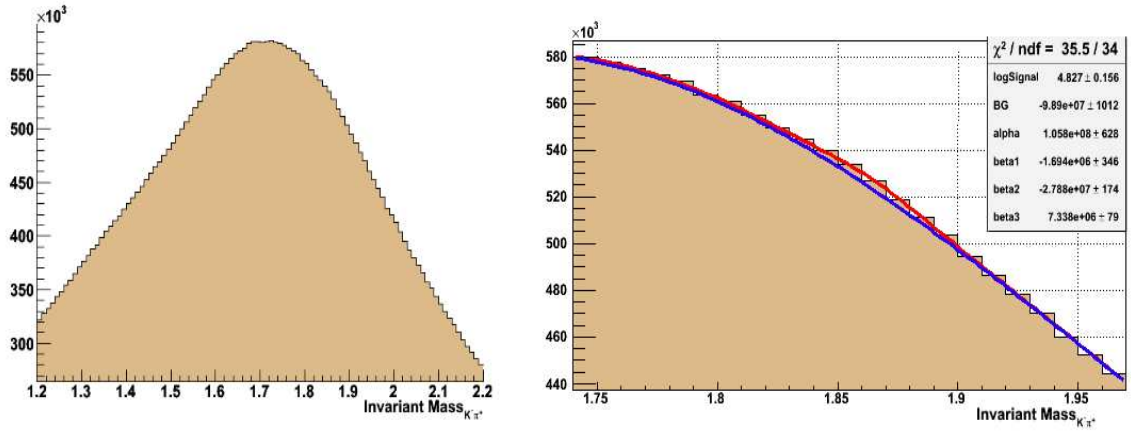

Figure 4.2: Background unsubtracted invariant Mass Plots - CutSet 1

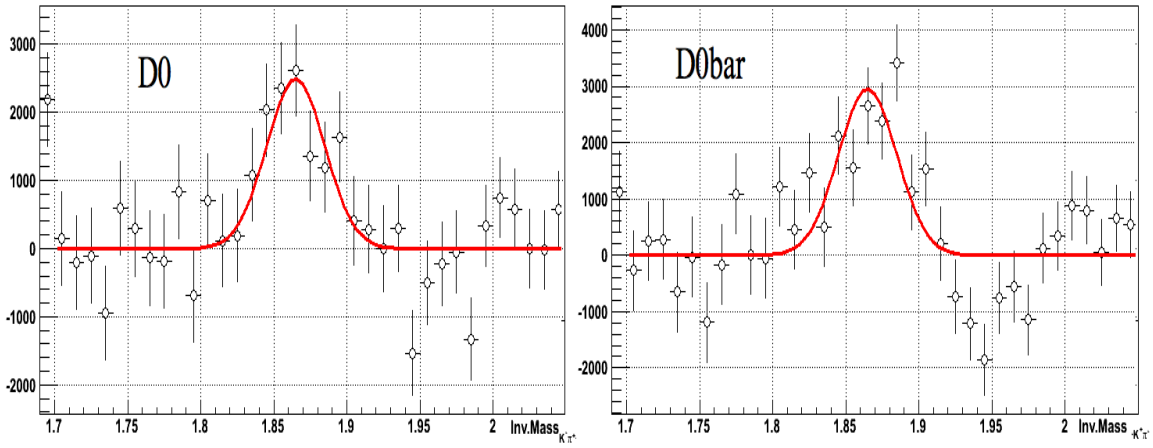

Figure 4.3: D^0 and $\bar{D}^0$ signal after background subtraction - CutSet 1

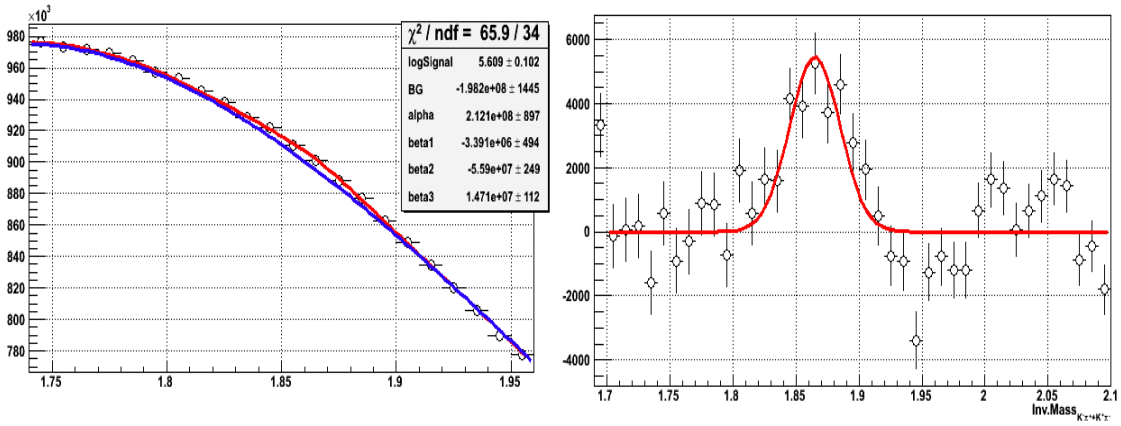

Figure 4.4: Combined $D^0 + \bar{D}^0$ signal - CutSet 1

The left plot in Fig. 4.2 shows the invariant-mass distribution obtained by using the offline cuts given in CutSet 1. In order to extract the signal (S) the invariant-mass distribution is fitted with a third-degree polynomial combined with a gaussian function. The background (B) is fitted with a third-degree polynomial. The right plot in Fig. 4.2 shows the signal (red line) and background (blue line) fit, which is zoomed in around the D^0 mass region. The fit was achieved by a χ^2 minimization method and it returns a value of $\chi^2/NDF \sim 1.04$. The rule of thumb for this method is that a good fit is achieved when the reduced χ^2/NDF equals one. When the data have uncertainities that are gaussian distributed, the χ^2/NDF has an expectation value of one. In the next step, the background fit function is subtracted from the signal and we obtain the peaks for D^0 and $\bar{D}^0$ as shown in Fig. 4.3. This is fitted with a gaussian function. Significance[2] ($\frac{S}{\sqrt{S+B}}$) of the observed signal after background

[2]The significance or effective signal is used in situations where signal has to be judged in the presence of an underlying background. See Appendix D

subtraction is $\sim 6.4\sigma$ for D^0 and $\sim 7.4\sigma$ for $\bar{D}^0$, where significance is

$$\frac{S}{\sqrt{S+B}}. \tag{4.1}$$

Here the assumption is that the statistical uncertainity on background is negligible since background is fitted over a wide range of invariant masses. Figure 4.4 shows the combined $D^0 + \bar{D}^0$ plot. When combined, the peak has a significance of $\sim 10\sigma$. The mean of the gaussian is 1864.19±10 MeV/c^2, which is consistent with the published D^0 mass value of 1864.83±0.14 MeV/c^2.

CutSet 2: -200 μm < decay length < 400 μm, |decay length| > 50 μm

|DCA of D^0 to PV| < 300 μm, $DCA_{K\pi} < 200\mu$m

|Rapidity of D^0| < 0.5, Track momenta > 0.7 GeV/c

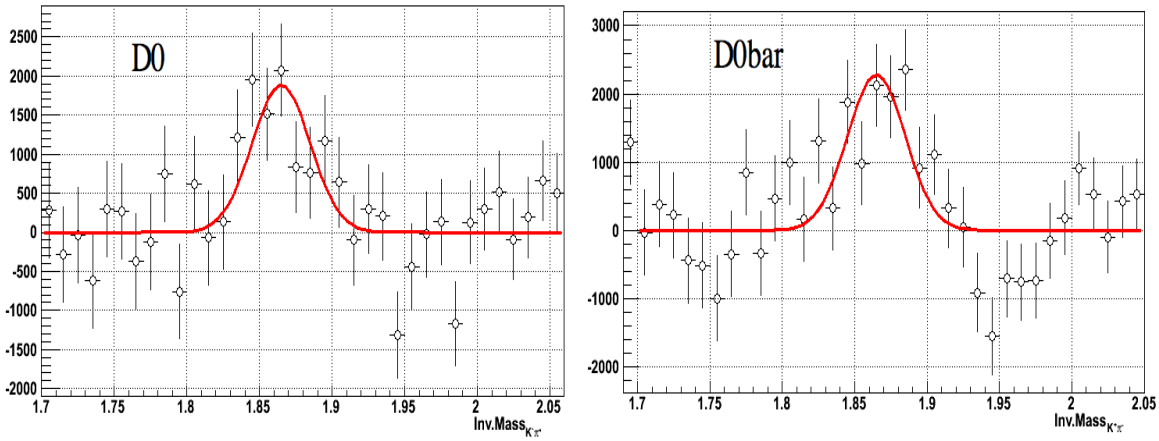

Figure 4.5: D^0 and $\bar{D}^0$ signal after background subtraction - CutSet 2

Here the decay length was varied from CutSet 1. The new cut on signed decay length selects mostly from the positive side, but with a lower cut, |decay length| > 50μm.

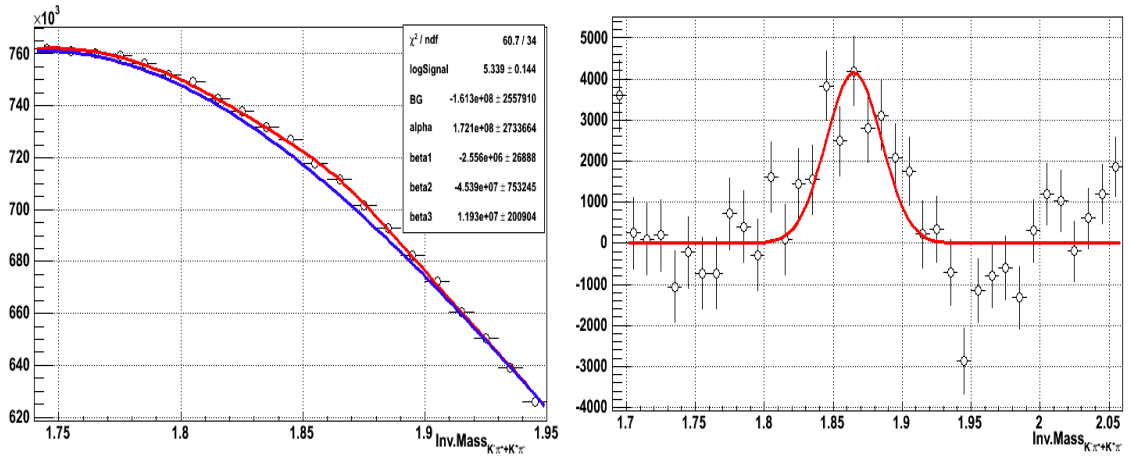

Figure 4.6: Combined $D^0 + \bar{D}^0$ signal - CutSet 2

This cut was tried because, as shown in Sec. 3.6.1, most of the signal events have positive decay lengths whereas the background has no such bias. The signal remains stable and the significance of the observed peak is $\sim 5.4\sigma$ for D^0 and $\sim 5.3\sigma$ for $\bar{D}^0$ (shown in Fig. 4.5). The combined $D^0 + \bar{D}^0$ gives a significance of $\sim 7\sigma$. With CutSet 2 the quality of the fit is better compared to CutSet 1. Table 4.1 gives significance of the signal for various cut sets and the χ^2/NDF of the fit for each case.

One can cross-check the significance value returned by the fit macro by using a bin counting method. This is done by counting the number of signal+background entries under the mass curve for $\pm 3\sigma$ from the mean of the gaussian. For the background, the entries under the third degree polynomial fit is found in the same mass range. The bin counting method in the region 1.81-1.92 GeV/c^2 for CutSet 1 gives 42K signal candidates and 9.8M background counts. This gives, $S/\sqrt{S+2B}$ as ~ 9.5, consistent with value reported by the fit macro.

4.1.2 Stability of the signal

The stability of the signal can be studied by changing the cut values slightly and by looking at the effect on the signal peak. Table 4.1 lists the significance of the observed signal for various cut sets. The table shows that the signal remains robust

CutSet/*Cut varied	Particle	Significance ($\frac{S}{\sqrt{S+B}}$)	χ^2/NDF
CutSet 1	D^0	6.4σ	35.5/34
	$\bar{D}^0$	7.4σ	60.4/34
	$D^0 + \bar{D}^0$	9.8σ	65.9/34
CutSet 2	D^0	5.4σ	35.7/34
	$\bar{D}^0$	5.3σ	54.3/34
	$D^0 + \bar{D}^0$	6.9σ	60.7/34
$*DCA^{D^0}_{PV} < 400\mu$m	D^0	6.4σ	38.1/34
	$\bar{D}^0$	8.5σ	77.8/34
	$D^0 + \bar{D}^0$	8.3σ	72.9/34
$*DCA_{K\pi} < 300\mu$m	D^0	6.2σ	57.7/34
	$\bar{D}^0$	7.1σ	60.35/34
	$D^0 + \bar{D}^0$	9.3σ	90.1/34

Table 4.1: Stability of the D-meson Signal.

when cuts are varied. The best signal is for CutSet 1, and the best χ^2/NDF is for CutSet 2. The third and fourth rows gives varied cut values from CutSet 1 and the result.

4.1.3 Signal Extraction using a Polynomial fit to the Background

The function we used to fit the invariant-mass output was an N-degree polynomial+gaussian:

$$\text{Func} = \text{Yield}(y) \times \text{Gauss} + (\text{Pol}^{\text{N}}) \tag{4.2}$$

where the gaussian function is normalized to one, so as to take into account the binning effects. In other words, if the number os bins are doubled then the counts

under each bin will reduce to half. The N-degree polynomial was used to describe the background. When doing the background fit the the region within 6σ of the D^0 mass is excluded to avoid fitting the cross-feed particles. The D^0 fit macro uses a variable, called z defined as,

$$z = \ln(y). \tag{4.3}$$

This variable is introduced to avoid negative yields. Taking derivative of Eq. 1.3 gives:

$$\frac{1}{dz} = \frac{y}{dy}, \tag{4.4}$$

where $\frac{y}{dy}$ is the significance($\frac{S}{\sqrt{S+B}}$) of the signal (see Appendix D). The fit macro returns both z and dz. When background is determined from fits, the statistical uncertainity on background is often neglected. The value $z + dz$ is reported by the fit macro. The raw yield (counts under the peak) for the cut sets is given in Table 4.3. It is obtained by taking $\exp(z + dz)$ multiplied by number of bins/GeV to get the total yield.

4.1.4 Sensitivity to the Degree of Polynomiall fit

The invariant-mass plots presented here uses a third degree polynomial fit for background estimation. The degree of polynomial fit to the background was varied to see its effect on the signal. Table 4.2 gives the signal and fit quality when going from second-to-fifth degree polynomial fit. The significance of the signal remains stable, however the fit quality degrades when going to higher degree polynomials. The signal is somewhat sensitive to the degree of polynomial fit. Other background estimation methods such as same sign background where tracks with same signs ($++/--$) are

CutSet/*Cut varied	Degree of Pol Fit	Significance ($\frac{S}{\sqrt{S+B}}$)	χ^2/ndf
CutSet1	2nd	10.3σ	60.26/35
	3rd	9.8σ	65.9/34
	4th	9.4σ	73.77/33
	5th	8.9σ	83.99/32
CutSet2	2nd Degree	8.9σ	57.2/35
	3rd	6.9σ	60.7/34
	4th	6.6σ	66.06/33
	5th	6.4σ	73.39/32
$*DCA^{D^0}_{PV} < 400\mu$m	2nd	10.5σ	65.9/35
	3rd	8.3σ	72.89/34
	4th	7.9σ	82.23/33
	5th	9.1σ	94.03/32
$*DCA_{K\pi} < 300\mu m$	2nd	10.5σ	65.9/35
	3rd	9.3σ	90.08/34
	4th	9σ	101.7/33
	5th	8.4σ	116.7/32

Table 4.2: Sensitivity to the degree of polynomial fit

paired, mixed event where tracks from different events are paired etc. are needed to make robust measurements and conclusions. To try a same sign background creation, and to study the systematics, we saved all charge combinations in the second production.

4.1.5 Raw Yield and $\bar{D^0}/D^0$ Ratio

In high-energy collisions, a statistical approach can be used since the collision involves a large number of nucleons and an even larger number of secondary hadrons emerging from such collisions. Particle abundances can give information about the chemical composition of the system. Particle ratios constrain the chemical freeze-out conditions. The statistical-thermal model has two parameters: the baryonic chemical potential $\mu_{\rm B}$, and the temperature T. From experimental data on particle abundances, the value of $\mu_{\rm B}$ can be determined. The temperature T can be obtained

from an analysis of particle spectra. The baryonic chemical potential decreases with increasing energy of the collision [76], becoming quite small at RHIC energies. The temperature increases, reaching a plateau value of about 170 MeV, which compares well with the critical temperature obtained from lattice QCD calculations for the phase transition.

Calculations of particle yield ratios using the statistical-thermal model showed good agreement with measurements at SPS and RHIC suggesting a high degree of chemical equilibrium at freeze-out. The statistical model fit parameters (T, $\mu_{\rm B}$) are determined by comparing model ratios to experimental values (by χ^2 minimization). At RHIC energies, they are determined to be T = 174±7 MeV, $\mu_{\rm B}$ = 46±6 MeV [77][78] for Au+Au collisions at $\sqrt{s}$ = 130 GeV. Table 4.3 presents the raw yield and the $\bar{D^0}/D^0$ ratio obtained for various cut sets. The ratio is stable when cuts are varied. The $\bar{D^0}/D^0$ ratio obtained in this analysis is close to unity and compatible with a vanishing $\mu_{\rm B}$ at RHIC energies. We expect a value close to unity since charm is mostly produced via the gluon fusion process.

CutSet/*Cut varied	D^0 Yield (e^{z+dz}) (e^{z+dz}) $\times 10^2$	$\bar{D^0}$ Yield (e^{z+dz}) (e^{z+dz}) $\times 10^2$	$\bar{D^0}/D^0$ Ratio
CutSet 1	12484±1948	14812±1985	1.18±0.24
CutSet 2	9416±1730	11421±2147	1.21±0.32
$*DCA^{D^0}_{PV} < 400\mu$m	12584±1976	18981±2240	1.5±0.3
$*DCA_{K\pi} < 300\mu$m	17295±2802	20014±2822	1.15±0.25

Table 4.3: Raw yield and $\bar{D^0}/D^0$ ratio for different cut sets

4.1.6 Binary Collisions (N_{bin}) Scaling

Due to its mass, heavy flavor is produced during the early stages of collision. Its production cross section is found to scale with the number of binary nucleon-nucleon

collisions [75]. Study of binary collision scaling of the charm cross section can be used as a strong test of theoretical calculations and to determine if charm is produced in the early stages of collisions at RHIC. This is done by studying signals for different centrality classes. The midrapidity ($|\eta|$ <0.5) multiplicity is assumed to increase monotonically with centrality and it is used for centrality class definition. STAR uses the Glauber Monte Carlo approach for the calculation of geometry-related quantities such as average number of participants $\langle N_{\rm part}\rangle$ and nucleon-nucleon collisions $\langle N_{\rm coll}\rangle$. The Glauber model is a theoretical technique developed to estimate quantities such as impact parameter (b), $N_{\rm part}$, $N_{\rm coll}$ etc. (See Appendix C).

The reference multiplicity saved in the first production needed a reweighing correction to obtain a proper distribution. This was because the first production counted tracks in $\eta < 0.5$ instead of $|\eta| < 0.5$.

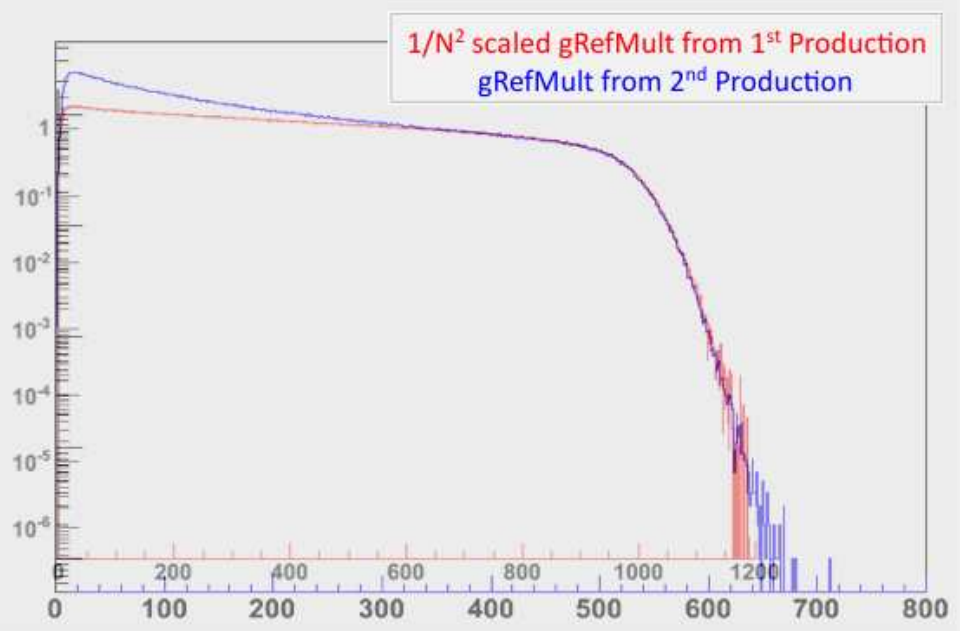

Figure 4.7: Reference multiplicity distribution from first and third productions

We rescaled this distribution with the square of the gRefMult since the background scales with gRefMult^2. The shape of the rescaled reference multiplicity matches with the correct distribution from third production as can be seen from Fig. 4.7. By looking at the x-axis, one can see that the scaling factor is ~ 0.54. However a translation between scaled first production data and MC Glauber results tells us that the conversion factor is 0.62×gRefMult. The final scaled gRefMult is shown in the left plot of Fig. 4.8. A comparison of the data with Glauber results shows that the centrality cuts given in Table 3.3 are valid.

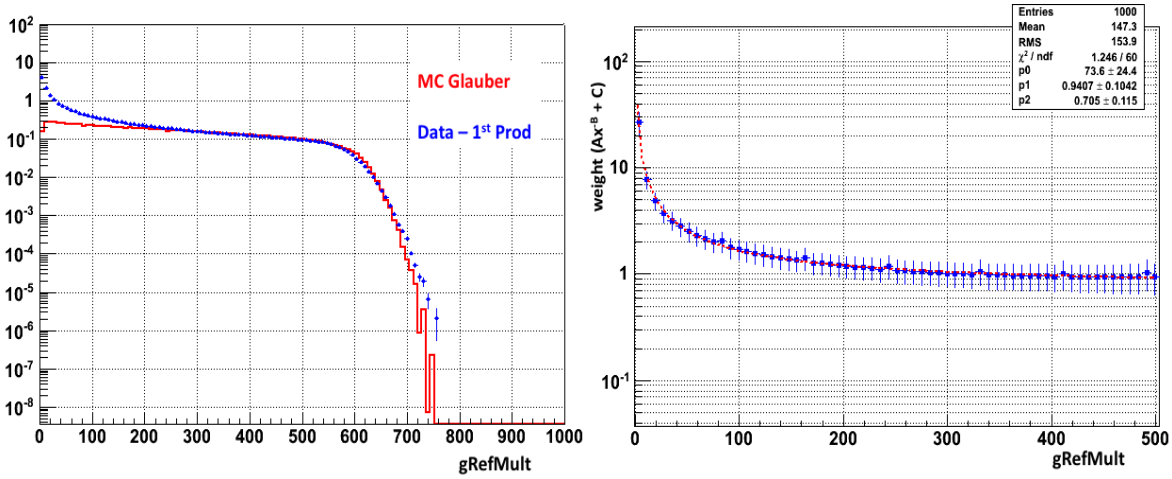

Figure 4.8: Reference multiplicity distribution of Monte Carlo Glauber model with data (left), and the correction factor (right)

The remaining issues were biases due to VPD-trigger requirement. The VPD trigger required events to fall within the inner tracker acceptance; thus, events at higher primary vertex-z are more likely to be peripheral events and events at lower primary vertex-z are more likely to be central [69]. Thus, VPD is more efficient in triggering on central events than peripheral events. This bias can be seen from the left plot of Fig. 4.8, where data differs from the Glauber calculation. To fix this, a

reweighing correction of the functional form $Ax^{-B} + C$, was applied, as shown in the right plot of Fig. 4.8. Here, x is the gRefMult and the values of the parameters A, B and C are given on the plot. As mentioned before, the reason for this bias is the VPD trigger, but also, the VPD's online z resolution is worse for peripheral events relative to central which can lead to a general deficit in peripheral events for a given data sample. Since the trigger-setup (200013) insisted events to fall within the inner tracking acceptance, i.e. with an online cut of $|PV_z| < 5$ cm, the resolution issue means that events at the higher $|PV_z|$'s are more likely to be peripheral whereas the events at lower $|PV_z|$'s are more likely to be central. Thus, there are z-dependent biases in multiplicity distributions.

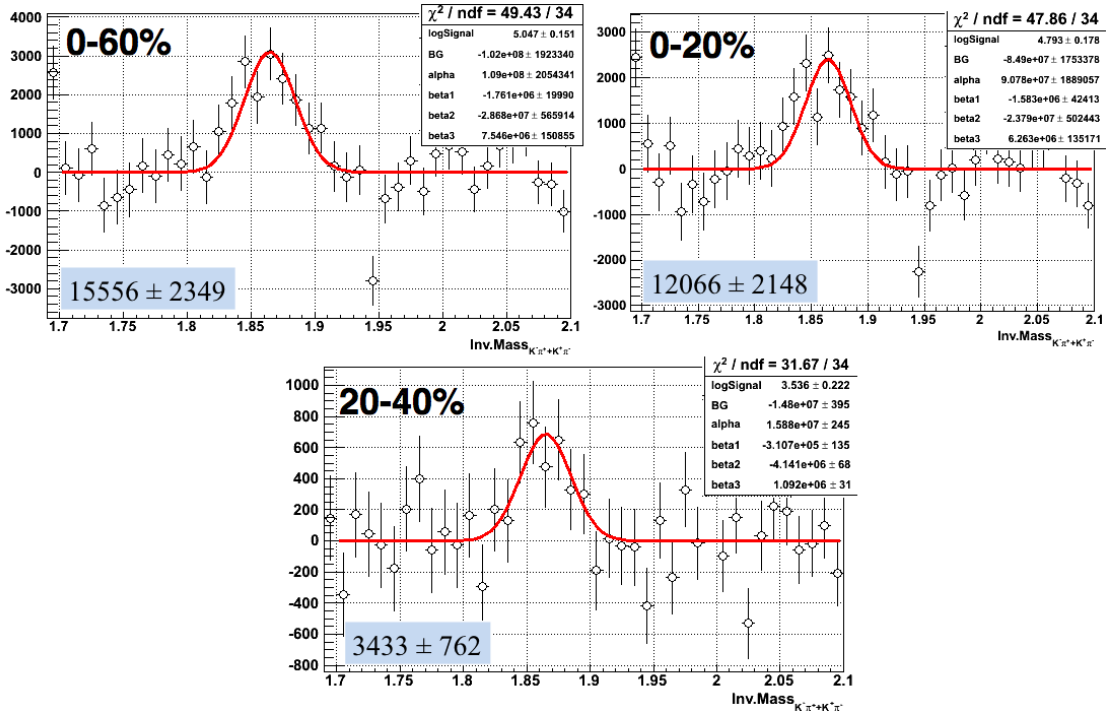

Figure 4.9: Invariant-mass peaks for various centralities

The invariant-mass plots are presented in Fig. 4.9 for centralities, 0-60%, 0-20%

and 20-40%. It uses the reweighing correction as explained above. It can be noted that the fit quality is improved after using the reweighing correction. The central bin, 0-20% gives a signal with significance of 5.6σ, 20-40% gives 4.5σ, 40-60% gives 2σ and 0-60% gives 6.6σ.

From Fig. 4.9 the signal seems to scale with the number of binary collisions, with highest significance for the central and lowest for the peripheral. To test this, we can calculate a ratio of yield (dN/dy) for central events scaled by the number of binary collisions (N_{bin}) to the yield in minimum bias events scaled by N_{bin}. When this ratio is done per event we expect a value close to 1, since charm should scale with the number of binary collisions. However, the first production did not save the event information in the output tree and therefore this plot will be presented from the second production later in this chapter.

4.1.7 Invariant-Mass Spectra of $D^0 + \bar{D}^0$

Spectra of particles produced in collisions of relativistic nuclei are usually plotted in transverse variables, since these are Lorentz invariant. To study the p_T spectra, the signal is first divided into three p_T bins for rapidity < 0.5. The signals for the three p_T bins, 0.6 - 0.9 GeV/c, 0.9 - 1.2 GeV/c and for 1.2 - 1.5 GeV/c are shown in Fig. 4.10. These plots uses the reweighing correction as explained in Sec. 4.1.6. The p_T spectra, which are the normalized yield ($\frac{1}{2\pi p_T N_{Events}} \frac{d^2N}{dydp_T}$) versus p_T is usually done with the rapidity range set to $|y| < 0.5$, so that dy =1. Since the event information was not saved in the output tree structure in first production, we cannot extract a normalized yield here. The p_T spectra will be presented from second production later in this chapter.

Corrections to acceptance of the detector and reconstruction efficiency are needed

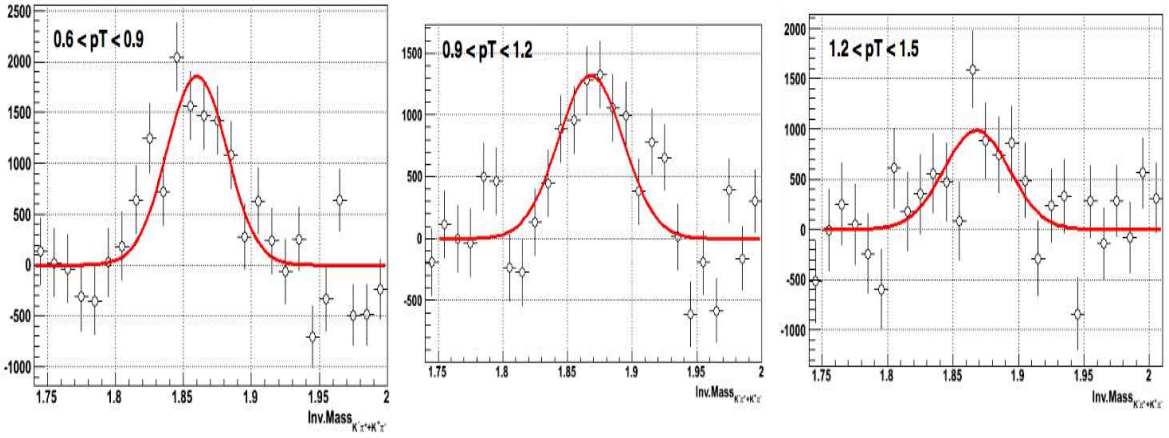

Figure 4.10: $D^0 + \bar{D}^0$ p_T bins (0-60%)

to estimate the yields of the particle in the collision and to discuss any physics from an analysis. At the time of writing this dissertation, we do not have a proper embedding sample to correct for the raw yields presented in this section. Complications in embedding to recreate SVT slow simulator[3] response is an issue with the current embedding sample. A corrected p_T spectrum can be used to measure the total charm cross section in Au+Au collisions.

4.1.8 Invariant-Mass Peaks from Monte Carlo Embedding

The microvertexing method was used to reconstruct D^0 particles embedded in real data events. The number of Monte Carlo particles generated per event was set to 5% of the multiplicity and these particles had a flat distribution in p_T. This check was done primarily to see if the code was successful in bringing up the signal in the presence of background. The plot in Fig. 4.11 was done using 2.5K events and it shows a clear signal peak corresponding to the D^0 mass even with 1% of the total

[3]simulator to obtain the SVT detector response to embedded particles passing through

embedding sample generated.

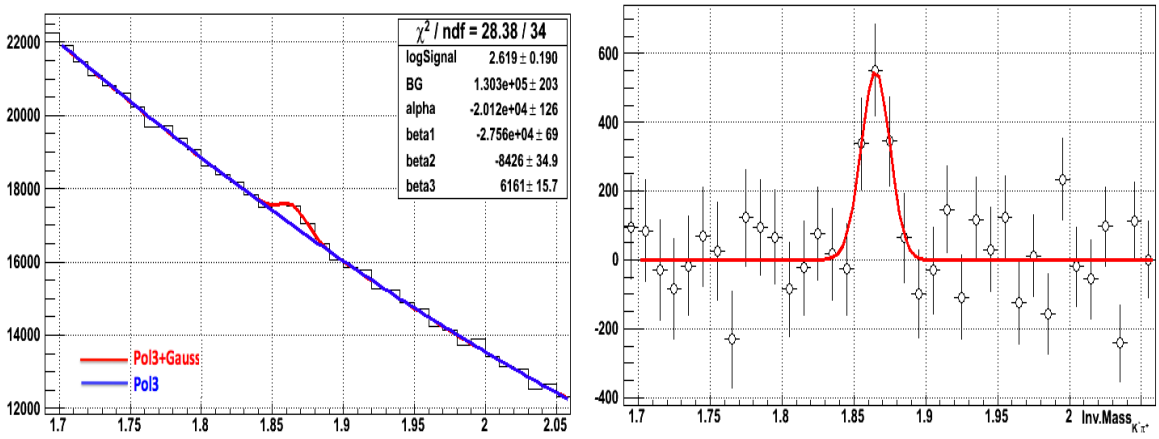

Figure 4.11: D^0 Invariant-mass peak from embedding data

However, the peak was obtained by requiring a minimum of two silicon hits. We used a tighter requirement for real data (SiHits > 2). It was shown that the current embedding sample has too few SVT hit points. As we increased the requirement on silicon hits to match with real data, there was loss of signal events and the significance of the peak got worse. The embedding data was used to assist analysis in cut tuning and also to do corrections for detector acceptance and efficiency. A section on corrections using simulation events is included at the end of this chapter.

4.2 Results from Second Production

As mentioned in Chapter 3, a second production was done with 2007 Au+Au dataset with modified cuts as given in Table 3.6. This production used a correct gRefMult calculation. The highlights of this production are that we saved the azimuthal angle of $D^0(\bar{D}^0)$ and calculated the event plane for an estimation of v_2. Also, all charge combinations were saved to try the same sign background subtraction.

I present results from polynomial background subtraction as well as the same sign background subtraction method.

4.2.1 Invariant-Mass Peaks - Using Polynomial Background

Figure 4.12 shows the invariant-mass distribution from second production before and after a polynomial background subtraction.

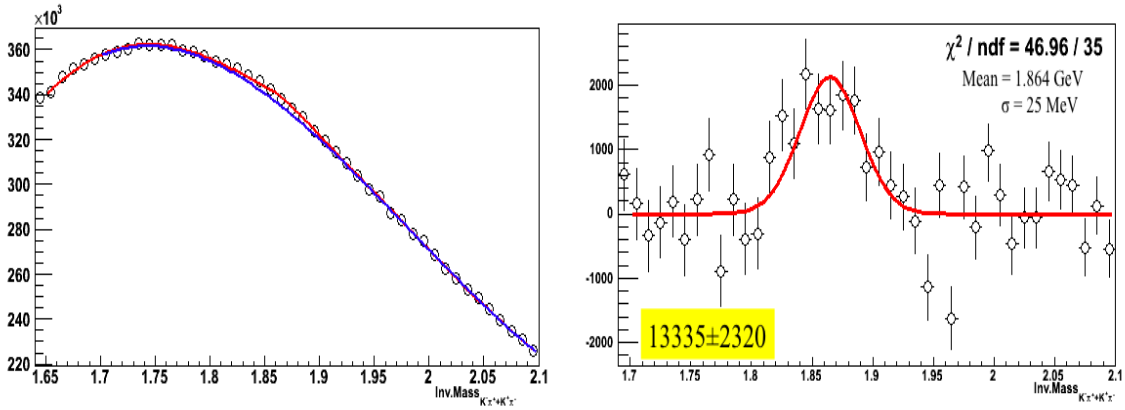

Figure 4.12: $D^0 + \bar{D}^0$ signal peak from second production - using polynomial fit

The plot was done with $\sim$ 11 million minimum bias events. The offline cuts on the plot are: 50 μm < decay length < 400 μm, $|DCA^{D^0}_{PV}| < 200$ μm, $DCA_{K\pi} < 200$ μm, P_K, $P_\pi > 0.7$ GeV/c.

The significance, $\frac{S}{\sqrt{S+B}}$, of the observed signal is $\sim 10\sigma$. The background was fitted with a second degree polynomial. From the fit to the data and background, the signal peak can be clearly differentiated. Compared to first production results we have better fit quality here. However the signal is not observed without a lower cut on momentum.

From the $D^0 + \bar{D}^0$ plot, we separated the $D^0(K^-\pi^+)$ and $\bar{D}^0(K^+\pi^-)$ contributions with a cut on the charge of the daughter tracks. Figure 4.13 shows the particle and

antiparticle signal peaks obtained. Also highlighted on the left hand corner is the raw yield obtained. From this the $\bar{D^0}/D^0$ ratio is 1.28±0.36 (stat.) which is compatible with the value from the first production. Here we assume the acceptance and efficiency effects are cancelled out.

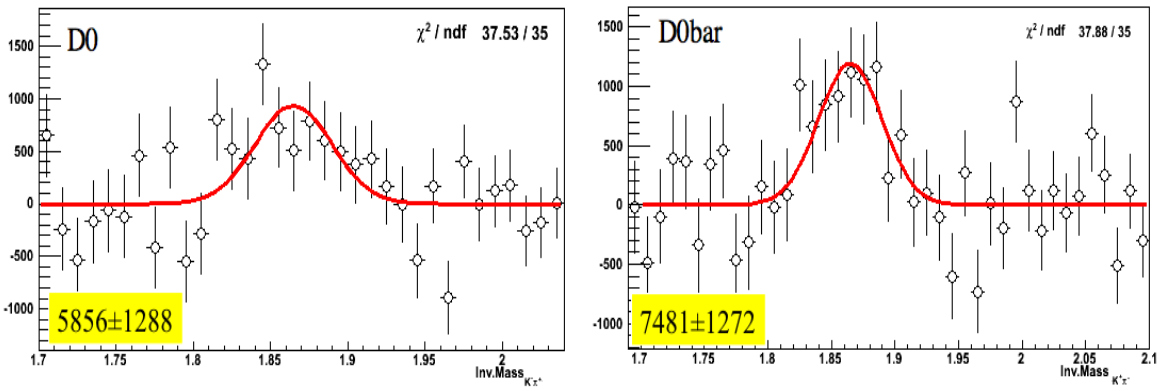

Figure 4.13: D^0 and $\bar{D^0}$ signals using polynomial background method

4.2.2 Binary Collision (N_{bin}) Scaling

D^0+$\bar{D^0}$ signal for three centralities, 0-20%, 20-40% and 40-60% is shown in Fig. 4.14 The ratio of the yield (dN/dy) for central events scaled by the number of binary collisions (N_{bin}) to the yield in minimum bias events scaled by N_{bin} is given in Fig. 4.15. Here the yield is normalized per event. However, the number of events used here did not take into account the loss the peripheral events due to the VPD trigger bias. Preliminary results of $(dN/dy)_{\rm cent}/(dN/dy)_{\rm MB}$ values obtained indicates deviations from the expected value of 1. The value corresponding to the central events is expected to get better when corrected for the trigger bias. However, this may not alter the other two cases, where we look at more peripheral events. This result came as a surprise and it points to the need of validating the invariant mass peak through more

robust background subtraction methods to see if the peak observed was an artifact. This could also be because of the cuts used. For example, the PYTHIA simulation

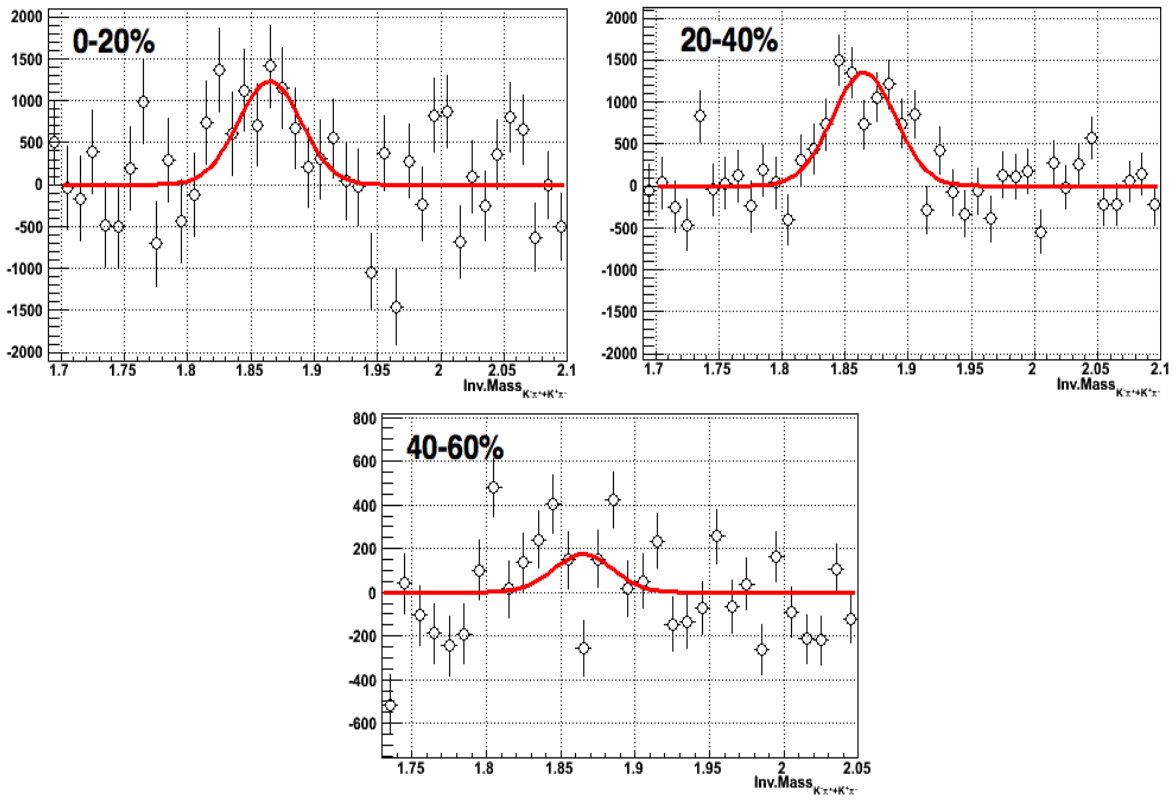

Figure 4.14: Invariant-mass peaks for the centralities 0-20%, 20-40% and 40-60%

showed that the cut on daughter momenta > 0.7 can cause a 60% loss of signal yield since the D^0 has a mean momentum of 1 GeV/c. These loss of signal events may have affected the overall characteristics of the signal. However, cut studies reveal that a lower cut on momentum as high as 0.7 GeV/c is required for a significant signal. This can be seen from Figure 3.12. When the momentum of the tracks are high enough the resolution is marginally adequate for reconstruction of D^0 however, at lower momenta the resolution gets worse. For example, when $\langle p_T \rangle = 1$ GeV/c, the

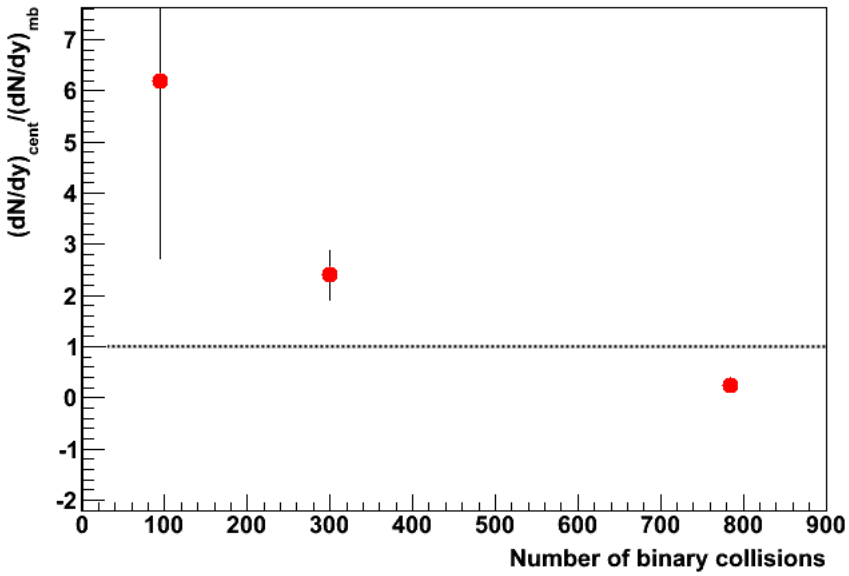

Figure 4.15: dN/dy ratio scaled by the binary collisions vs centrality

resolution of the tracks with 3-4 silicon hits is $\sim$ 250- 450 μm whereas at $\langle p_T \rangle = 0.5$ GeV/c, the resolution is poor $\sim$450- 700 μm. The previous generation silicon detectors does not allow a complete reconstruction of the decay vertex and the measurement suffers from ambiguities. The Heavy Flavor Tracker being built for STAR, with pointing accuracies as high as $\sim$ 25 μm at 1 GeV/c will allow a complete topological reconstruction of charm.

4.2.3 p_T Spectra

The signals for two centralities were divided into three p_T bins: 0.6 - 0.9 GeV/c, 0.9 - 1.2 GeV/c and for $p_T > 1.2$ GeV/c. Figure 4.16 gives the uncorrected p_T spectra obtained for 0-80% and 0-20% centralities for a rapidity range |y| < 0.5 and per event. For both centralities presented, we applied the corrections for the VPD trigger bias as explained before. The 0-10% centrality does not require corrections, or the corrections

needed are very small.

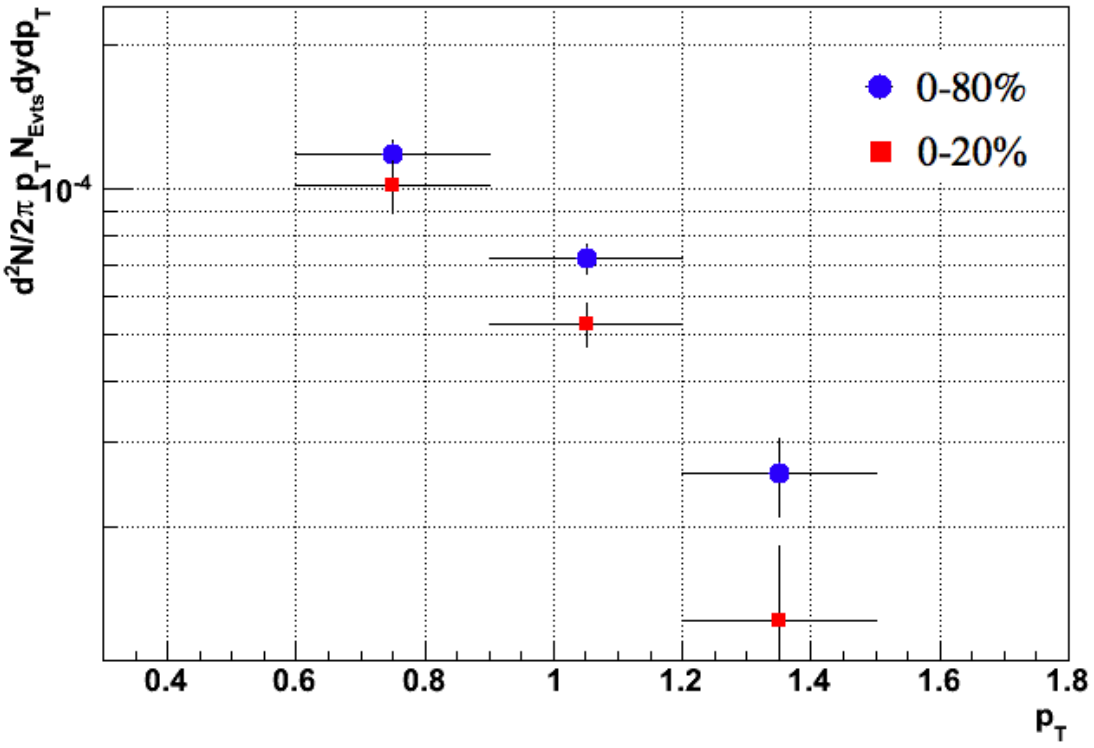

Figure 4.16: Uncorrected p_T spectra for $D^0 + \bar{D}^0$

4.2.4 Invariant-Mass peaks - Using Same-Sign Background

The polynomial background estimation method appeared robust and consistent and had been used in a number of earlier analyses. There are several other ways to do this delicate task. For a neutral particle, such as D^0, which decays into a positive and negative daughter, one can generate a true background by combining two positive tracks or two negative tracks from the same event. This can produce an invariant-mass distribution of random pairs. This is called the 'same-sign' method and it is widely used in experimental physics. Another method uses the 'event mixing' technique, by randomly selecting tracks each from different events to create a random

invariant-mass distribution. This method is typically used to perform a first level of background subtraction to remove the bulk of the background, which is then followed by a second subtraction using a simple fit. There is also a 'rotation method' where one of the daughter tracks is rotated in azimuth to destroy the initial correlation.

We used the 'same-sign' method in our analysis of the second production. We used two ways to generate the same-sign background: (1) a sum of $K^-\pi^- + K^+\pi^+$ and (2) $2\sqrt{K^-\pi^- \times K^+\pi^+}$. In both cases the same-sign distribution describes the background shape very well. Figure 4.17 shows the invariant-mass of oppositely signed pairs and same-sign pairs together. This plot uses the same offline cuts as in Fig. 4.12. The shaded area represents the same-sign combination and the red circles represents the opposite-sign distribution.

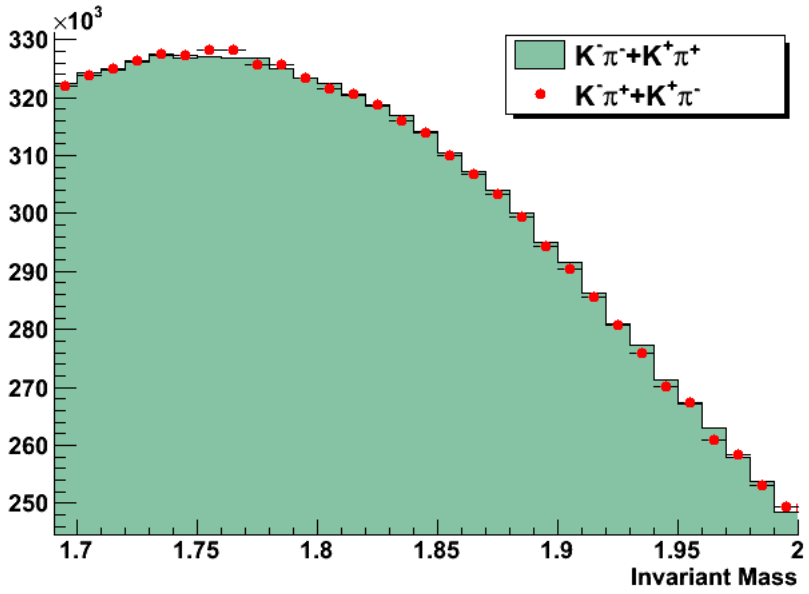

Figure 4.17: Invariant-Mass distribution of same/opposite sign pairs from second production

The same-sign distribution shows no peak above the background level. We performed a series of checks on the data set, but they failed to bring up a significant D-meson signal when using the same-sign background subtraction method. This was a completely unexpected result. However, one has to be cautious since the same-sign method is not desirable in low statistics scenarios. The charge symmetry produces same statistics for same-sign background as the original invariant-mass spectrum. After subtraction, the statistical uncertainity increases by a factor of $\sqrt{2}$. Some of the checks we did are discussed below.

As explained in Sec. 3.6.2, we used the information from significance distribution of cut variables to try a graphical cut. The ROOT graphical cut class TCutG can be used to select the highest significance areas from a 2D plot such as those shown in Fig. 3.28. The invariant-mass of $D^0 + \bar{D}^0$ which uses such a graphical cut selection, is shown in Fig. 4.18, before and after same-sign background subtraction. The offline

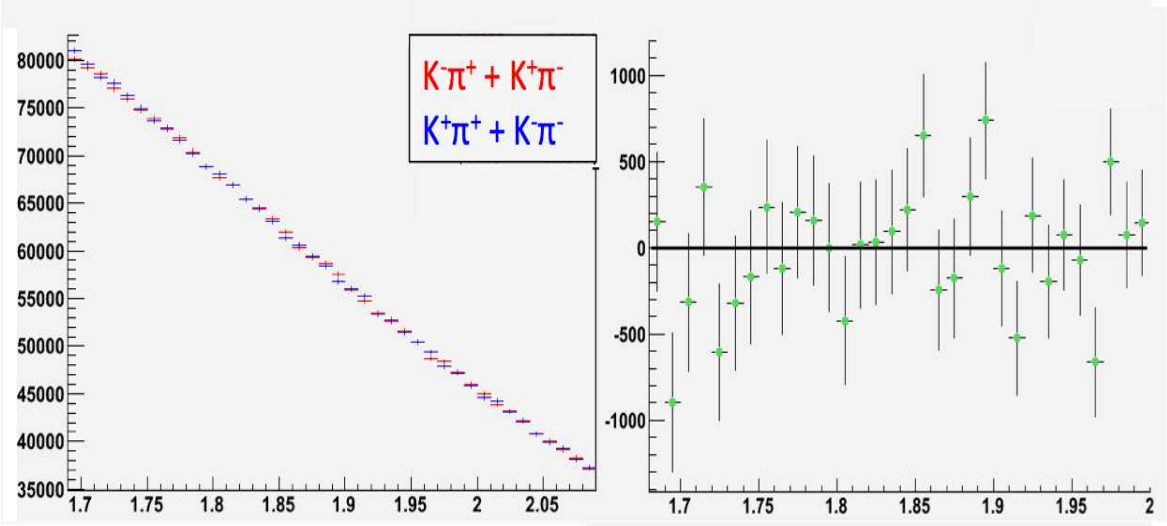

Figure 4.18: Invariant-mass distribution of same/opposite sign pairs (left) and subtracted plot (right) using a graphical cut selection

cuts used are graphical selection cuts on: (1) decay length significance, (2) $\mathrm{DCA}_{\mathrm{PV}}^{\mathrm{D}^0}$, and (3) decay length significance of daughter tracks K and π. This plot was done using 26 million events.

This data set suffers from poor particle identification (PID) capability between kaon and pion for $p_T > 0.7$ GeV/c. One way to reduce the kaon-pion contamination is to impose a tighter cut on the $N\sigma$. Another possibility is to use a momentum-dependent cut on the standard deviations of dE/dx distributions ($N\sigma$) cut. As shown in Fig. 4.19 we tried the PID cut based on the momentum region we used: For $p_T <$ 1.2 GeV/c, we used the upper half of the kaon band (blue band) and lower half of the pion band (red band); $0 < |N\sigma_K| < 2$ and -2 $< |N\sigma_\pi| <$ 0. For $p_T >$ 1.2 GeV/c, the cut was reversed, -2 $< |N\sigma_K| <$ 0 and $0 < |N\sigma_\pi| <$ 2.

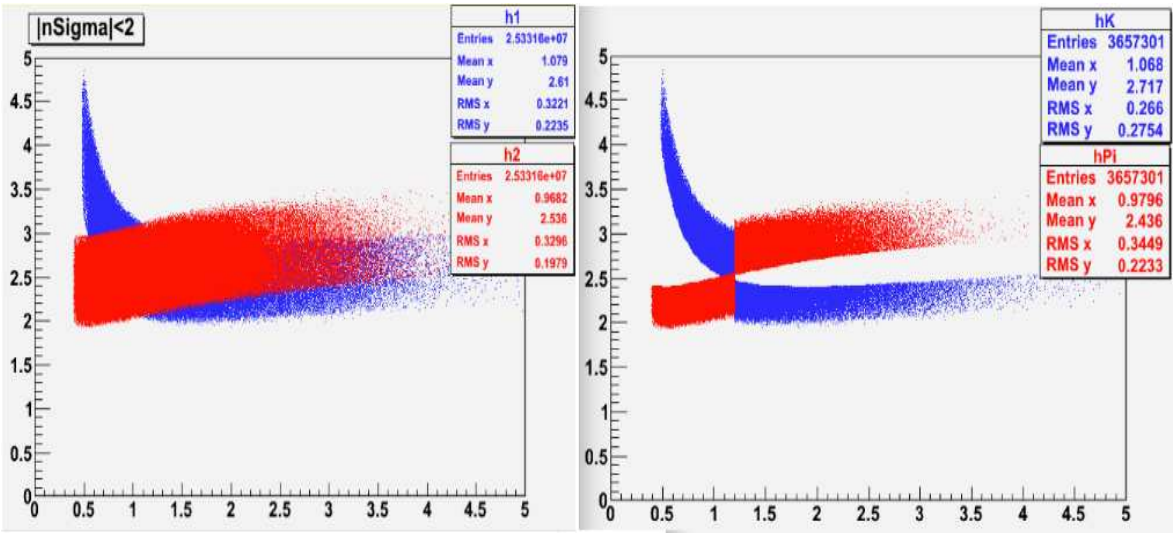

Figure 4.19: Kaon (blue) and pion (red) bands before (left) and after (right) a momentum-dependent dE/dx cut.

While it helps reduce the combinatorial background, the available statistics reduces significantly. From simulation, such a cut reduced the signal by 77% and background by 86%. Figure 4.20 shows a plot done with the new dE/dx. The subtracted

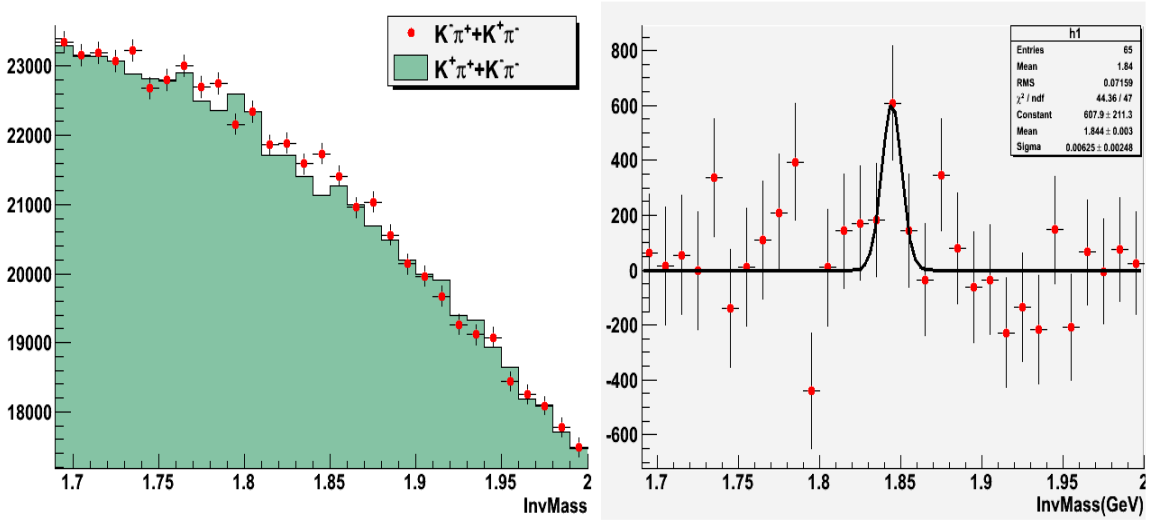

Figure 4.20: Invariant-mass of same/opposite sign pairs using graphical cuts and a momentum dependent dE/dx cut.

plot is fitted with a simple gaussian. However, it is impossible to make any claims with this plot. The width of the gaussian is lower than we expect for a real signal. We did a number of tests, including trying different cut sets and checking the real data to see the performance of the silicon detector as a function of time. Some days of the run are marked by enormous fluctuations in silicon detector performance reflected by a worse DCA resolution. We selected those days where the DCA resolution was stable. Perhaps, exploring another background generation such as the mixed event or rotational background method would be worth to try. The fact that one third of the SVT/SSD was dead during Run 7 (can be seen from Fig. 3.13), combined with the poor resolution of the silicon detectors and limited statistics prevented us from

obtaining a clean and statistically significant charm signal when using the 'same-sign' background estimates. The signal observed from first production is powerful, and is consistent with a vanishing baryo-chemical potential ($\mu_{\rm B}$) at RHIC. However due to the lack of event information in the saved output we could not extract more physics from this production. More results will be presented from second production. Another check one can do is to make a corrected p_T spectrum and extract estimates for the cross section to compare with theoretical predictions. In order to do this, the raw p_T spectra from polynomial background method, needed corrections to draw useful quantities such as the freeze-out temperature ($T_{\rm fo}$) for a comparison with the expected value at RHIC collisions. However, as mentioned before, we do not have a proper embedding sample to do corrections at this time. A final attempt to measure signal using a same-sign background subtraction is being done with the Toolkit for MultiVariate Analysis (TMVA). TMVA is a machine-learning technique as described in Sec. 3.6.3.

4.2.5 Preliminary Results using TMVA

As mentioned in Sec. 3.6.3, I will present the results using multivariate analysis in Monte Carlo embedding data here. This phase can evaluate the performance of the classifiers. I will show only the results from one classifier, the Boosted Decision Tree (BDT). BDT is a nonlinear discriminant analysis, which has been successfully used in high energy physics analysis. Successive decision nodes are used to categorize the events in the sample as either signal or background. Each node uses only a single discriminating variable to decide if the event is signal-like or background-like. This forms a tree-like structure with "baskets" at the end (leave nodes), and an event is classified as either signal or background according to whether the basket where it

ends up has been classified signal or background during the training. Training of a decision tree is the process to define the "cut criteria" for each node. The number of variables in the input training sample and their correlations are important.

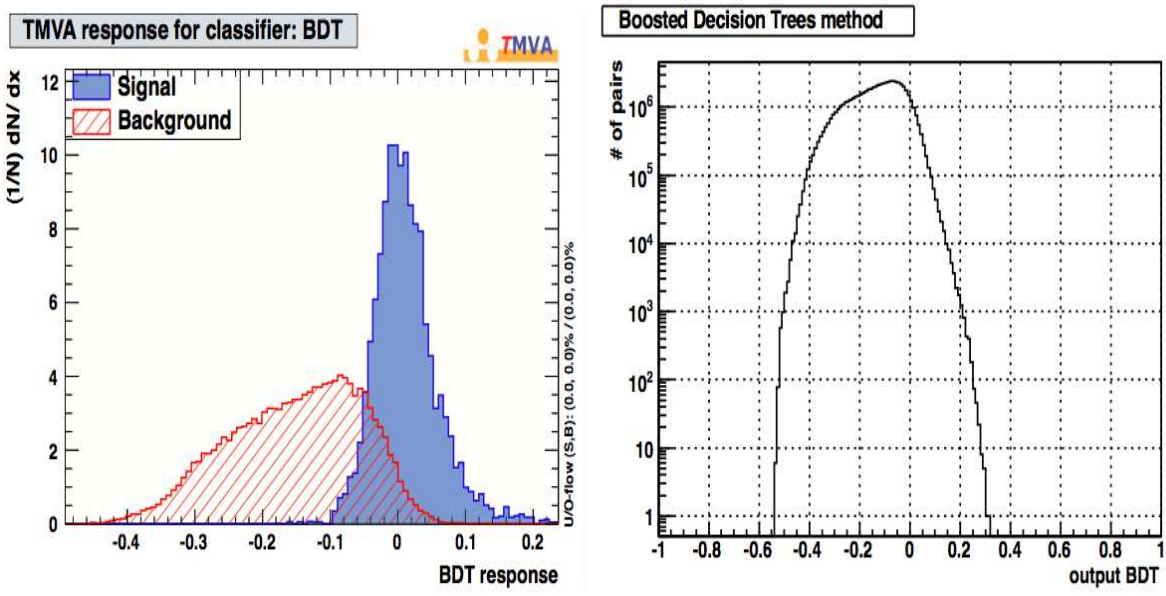

Figure 4.21: Boosted Decision Tree (BDT) classifier - probability density distribution for signal and background (left) and classifier output (right)

We chose to use pure D^0 events using power law p_T as the signal input and HIJING Au+Au events as the background for the training phase. The probability density distribution of signal and background created from the training sample (signal and background) is shown in the left plot of Fig. 4.21. As can be seen from the figure, BDT classifiers gives very good purity versus background rejection. After the training phase, a testing sample is given, it produces classifier output (right plot of Fig. 4.21), which is unnormalized. This is shown in the right panel of Fig. 4.21. The classifier output represents the signal and background behavior together. The signal-like events "go right" and background-like events "go left". Cutting on the classifier output is

equivalent to cutting on multiple variables. A possible cut on BDT output starts at 0; as one tightens this cut the background is more suppressed.

The TMVA analysis was tried on same and opposite sign pairs in a sample of Monte Carlo D^0 events embedded into a real data background sample. We looked at invariant-mass distributions of all sign combinations and for $K^+\pi^+, K^-\pi^-, K^+\pi^-$ and $K^-\pi^+$ separately. The results are shown in Fig. 4.22. The signal distribution ($K^-\pi^+$) shows a clear peak, whereas the background shows no peak. The method works fine and same-sign combination describes the background very well.

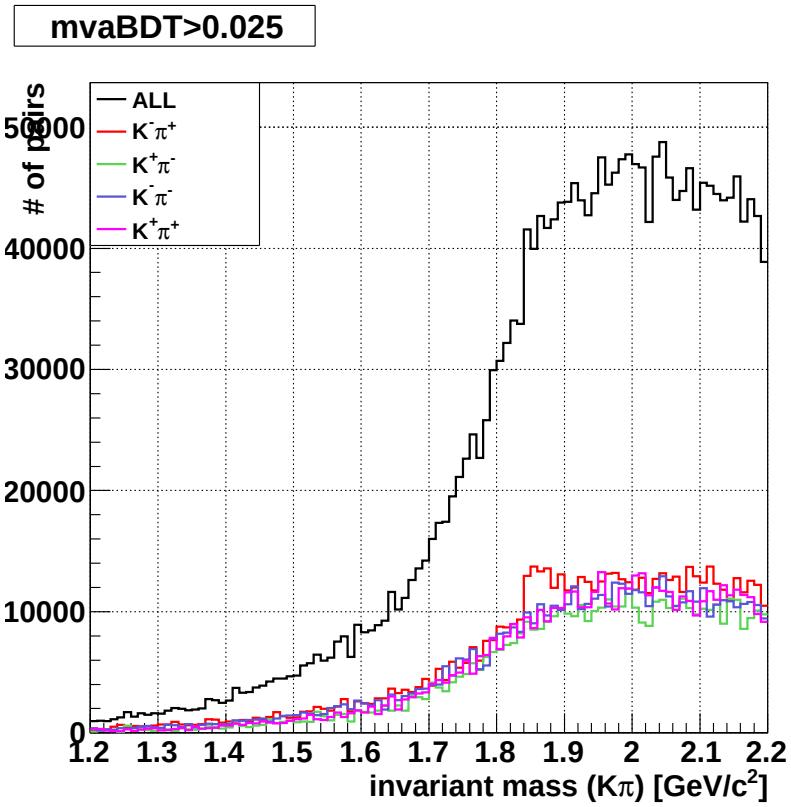

Figure 4.22: BDT classifier results on embedding data showing same/opposite sign charge combinations

The TMVA approach was tried for real data also. Here also, we used the Boosted

Decision Tree (BDT) classifier. The results are presented for a subset of the sample[4] available. Figure 4.23 shows invariant-mass peaks obtained from real data. The bottom right plot has no cut on classifier value, whereas the other three plots used a cut on the classifier value combined with a cut on decay length significance and pointing angle of the reconstructed D^0. A comparison of the plots shows that the above-mentioned cuts reduce the background by a factor of four orders of magnitude. Optimization of these cuts and trying a same-sign background behavior in real data with higher statistics is an interesting next step in this analysis.

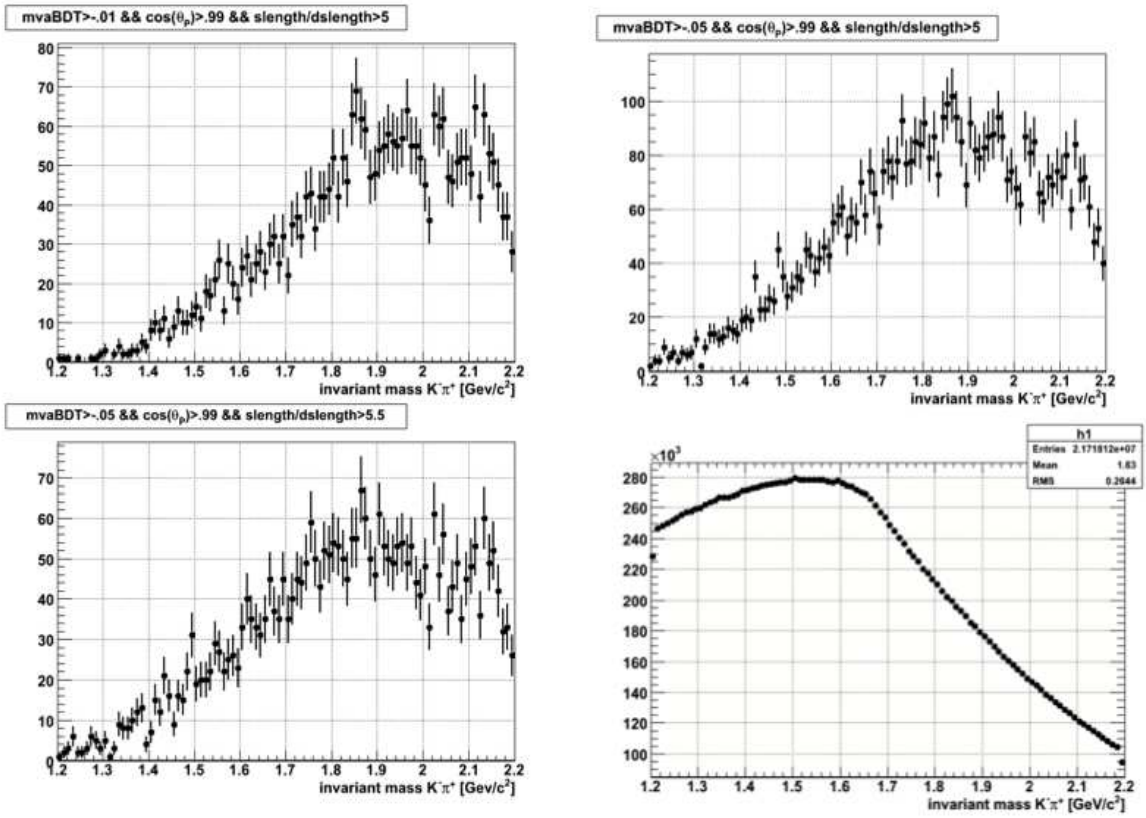

Figure 4.23: BDT classifier results in real data for opposite charge pairs

[4]day 123 of the 2007 RHIC run $\sim$ 2% of the available sample

A future possibility is to look at other decay channels of open charm mesons. One such channel is

$$D^+ \longrightarrow K_s^0 \pi^+. \tag{4.5}$$

The first step in this is the reconstruction of a K_s^0 using the TCFIT method. Once a clean sample of K_s^0 events is obtained it can be combined with pion tracks for D^+ reconstruction. The advantage here is that having a clean sample of K_s^0 events can reduce the combinatorial background coming from kaon-pion mixing. In the Sec. 4.3, I present K_s^0 reconstruction using the microvertexing code. The goal is to show a proof of principle of the TCFIT secondary vertex finder and utilize cuts on fit probability and decay length significance accessed through the secondary vertex fit method.

4.3 K_s^0 Reconstruction Using the Silicon Vertex Detectors

Here, we extend the analysis using STAR silicon detectors to strange particle reconstruction. Results are presented from 2007 Au+Au collisions at $\sqrt{S_{NN}} = 200$GeV for K_s^0 mesons, although other strange particles such as, Λ, Ξ and Ω were successfully reconstructed using the microvertexing code. K_s^0 events are reconstructed via the hadronic channel:

$$K_s^0 \longrightarrow \pi^+\pi^- \tag{4.6}$$

The decay has a branching ratio of 69.2% and a decay length of $c\tau = 2.68$cm. We used the code with cuts modified to the K_s^0 decay topology. The code loops over the track pool and each track is assigned to a π^-, a second loop within the first assigned to a π^+. The $\pi^+\pi^-$ candidates are then subjected to secondary vertexing.

4.3.1 Cuts

The K_s^0 analysis is based on secondary vertex fit properties, such as signed decay length, its uncertainity and probability of the fit etc., which are accessed through the TCFIT method. As such, we used a cut on decay length significance (described in Sec. 3.6.1) to obtain the signal peak. Figure 4.24 shows the effect of cutting on decay length significance ($S_L = \mathbf{dL}/\sigma_{dL}$). The left-most plot uses no requirement on S_L,

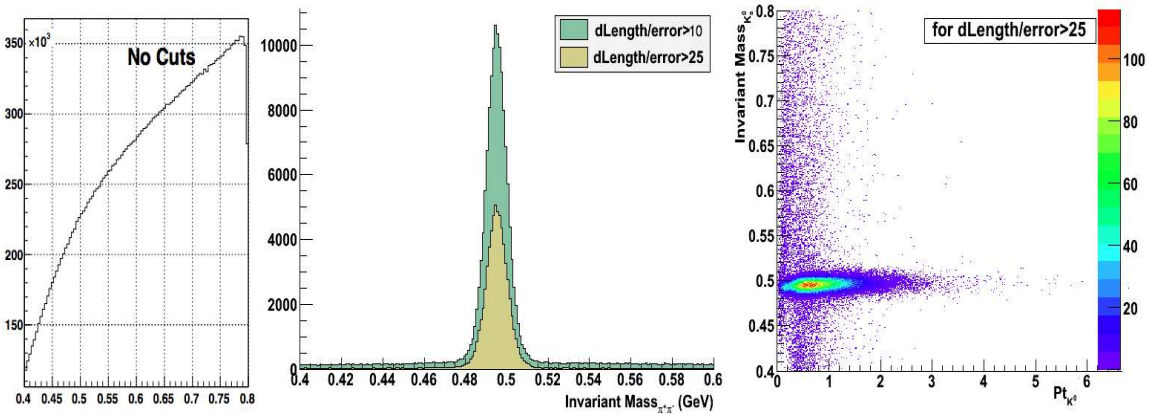

Figure 4.24: Invariant-mass plots showing K_s^0 signal.

whereas the middle plot is obtained when we cut on this variable. As this cut value is increased, the residual background completely disappears. Also we require the number of silicon hits to be greater than two. Another important variable accessed through the silicon detector is the impact parameter, a.k.a, DCA of tracks to the event vertex. The data was processed with microvertexing, code with cuts shown in Table 4.4.

4.3.2 p_T Spectra

Invariant mass peaks were identified from 0.1 to 5 GeV/c in p_T bins of width 0.5 GeV/c as shown in Figure 4.25. The signal is fitted with a gaussian. The mean

of the gaussian fit is 0.495 GeV/c^2 and the standard deviation of the signal peak

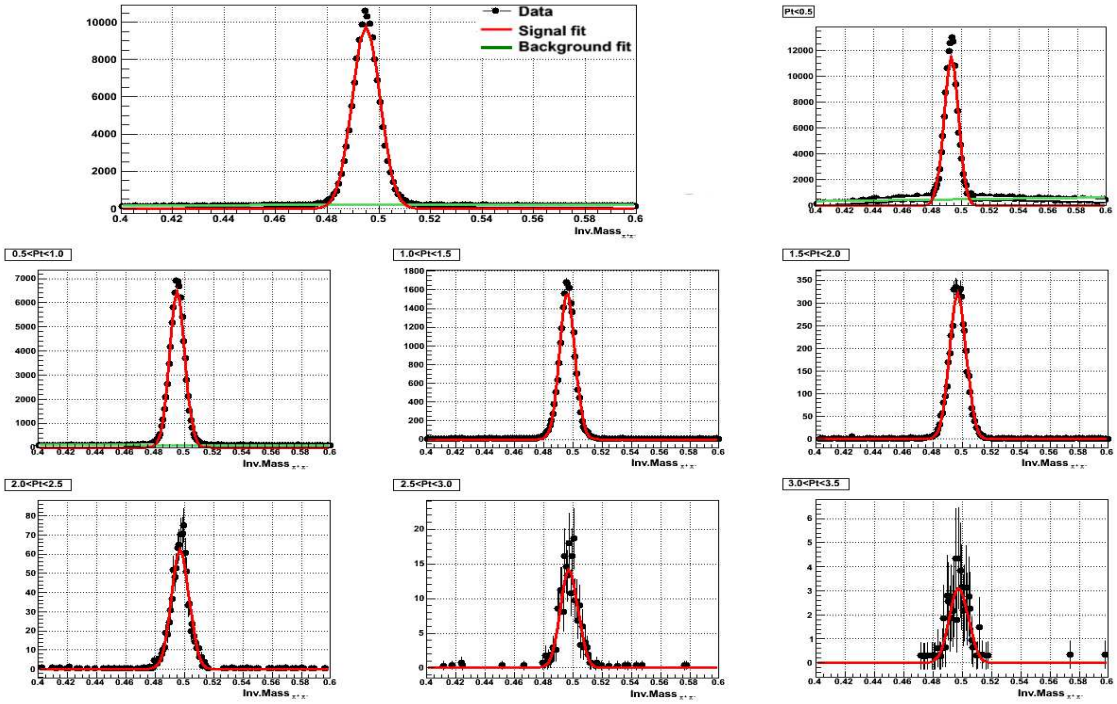

Figure 4.25: The K^0_s invariant mass peak and the signal rebinned into p_T bins.

is 5 MeV. The residual background is fitted with a 1st degree polynomial for lower p_T bins. The background goes to zero for $p_T > 1$ GeV/c. For $p_T < 1$GeV/c, the counts under the background fit is subtracted off from the total counts under the histogram in the range, 0.495 GeV/c^2 $\pm 3\sigma$. The extracted p_T spectrum for three centralities, 0-80%, 0-10% and 60-80% is given in Fig. 4.26. Here also there is a need for reweighing corrections to be done in order to account for the loss of peripheral events due to trigger bias. However, the plots shown here did not use the correction. With optimized cuts, it was observed that the p_T reach of the spectra can be extended.

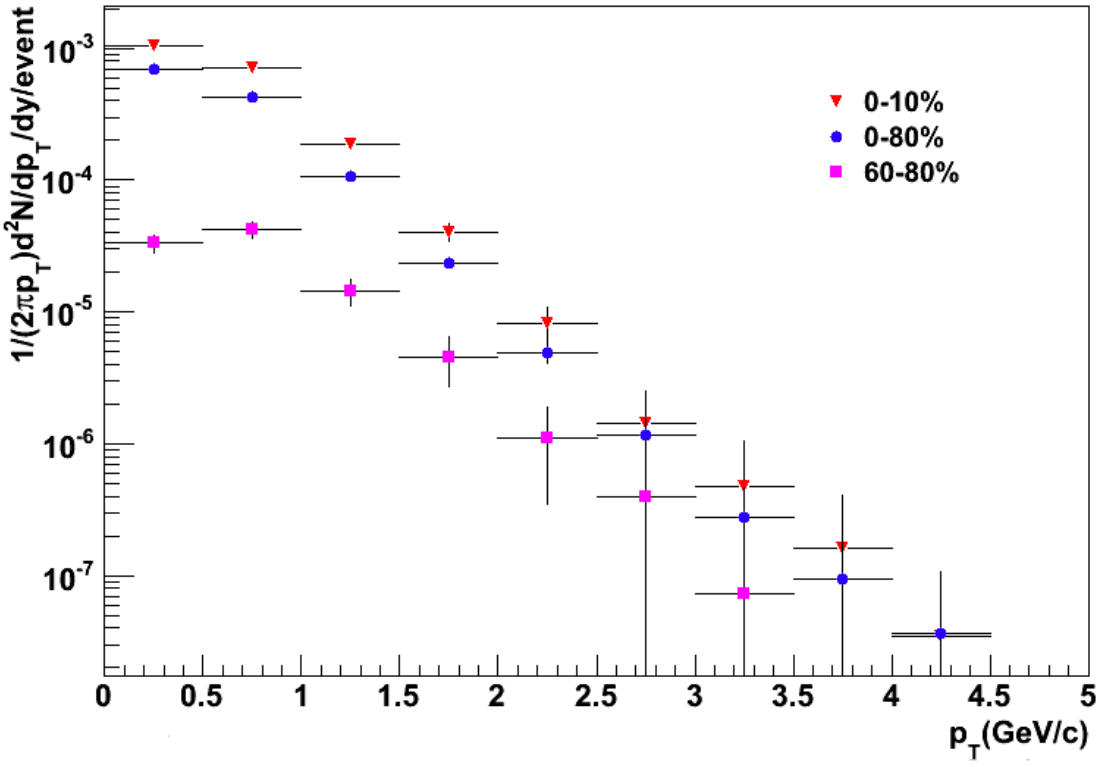

Figure 4.26: The uncorrected K^0_s invariant yield as a function of p_T

Cut Level	Cut Parameter	Cut Value
Event Level	Trigger Id	200001, 200003, 200013
	$\|V_z\|$	< 10 cm
	σ_{V_z}	< 0.1cm
Track Level	Ratio of TPCHits Fitted/Possible	> 0.51
	$\|\eta\|$	<1.2
	dE/dx TrackLength	> 40 cm
	Number of Silicon Hits	> 2
	decay length/uncertainity of decay length	> 15
	Transverse DCA to PV/error of DCA to PV	> 3
	Particle ID ($\|n\sigma_\pi\|$)	< 2.0
	Rapidity ($\|y_{\pi\pi}\|$)	< 0.5

Table 4.4: K^0_s Reconstruction - Cuts used

4.4 Corrections

The final spectra are obtained by applying corrections for the remaining background, and for acceptance of the detector due to limited geometrical coverage and for reconstruction efficiency. The corrections are usually done using signal and background events and a technique called embedding.

Monte Carlo D^0 and $\bar{D}^0$ particles are generated and they are propagated and decayed in the STAR setup. The GEANT determines how the generated particles interact among themselves and with the detector material. In order to evaluate the efficiency corrections for reconstruction, the TPC, SSD and SVT detector responses to the daughter tracks, kaons and pions at the time of the run, must be known. The response simulator generates an output in the same format as the real data. These are then mixed with real data and reconstructed. After this, an association maker is run to tag all tracks that are successfully reconstructed. The process is schematically shown in Fig. 4.27.

4.4.1 Acceptance and Efficiency Corrections

We need to account for all the daughter tracks that do not leave a measurable signal in the detector, and those that decay away before reaching the silicon layers. This type of correction is called an acceptance correction. So, acceptance correction is defined as:

$$\text{Acceptance}_{\text{correction}} = \frac{\text{all\_MC\_D}^0\text{\_particles\_that\_GEANT\_decayed\_in\_the\_fiducial\_volume}}{\text{all\_MC\_D}^0\text{\_particles\_that\_were\_embedded}}$$

We also have to account for all the D^0s that decayed in the fiducial volume but were

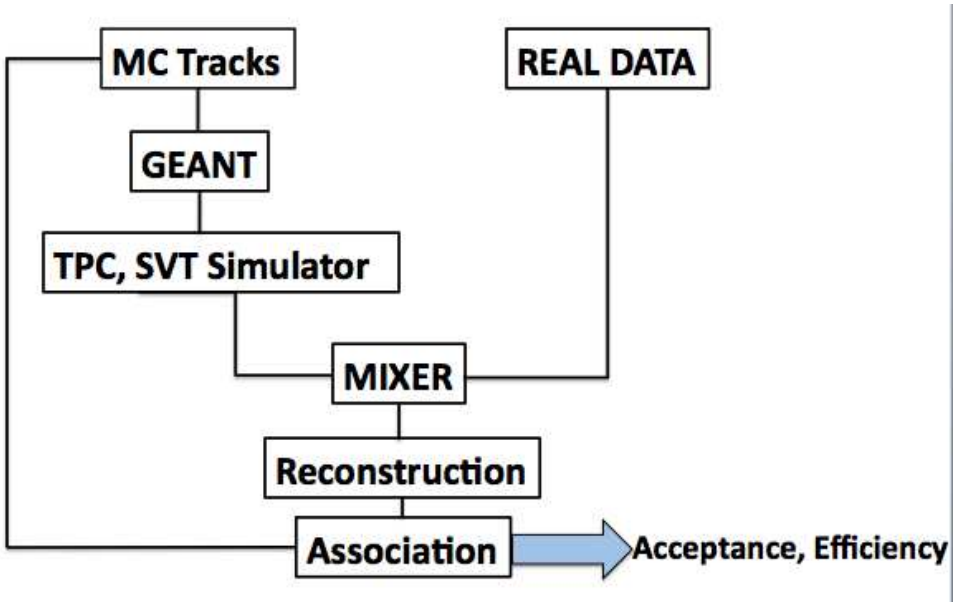

Figure 4.27: Schematic of the embedding process.

not found by the microvertexing code. These are the D^0s that did not pass the analysis cuts. This is called the efficiency correction and it is defined as:

$$\text{Efficiency}_{\text{correction}} = \frac{\text{all\_MC\_D}^0\text{\_particles\_that\_passed\_the\_analysis\_cuts}}{\text{all\_MC\_D}^0\text{\_particles\_GEANT\_decayed\_in\_the\_fiducial\_volume}}$$

An additional correction called the vertex correction, must be applied to account for primary vertices that existed, but were not reconstructed. This is called the vertex correction.

4.4.2 Systematic Corrections

The biases in measurements or systematic uncertainities are investigated through variation of analysis cuts, background subtraction methods, fitting methods and vertex correction methods. The relation used for calculating the systematic uncertainity

is given by:

$$s^2 = \frac{1}{n-1}\sum_{i=1}^{n}(x_i - x)^2, \tag{4.7}$$

where x_i is the result of the ith set of cuts out of the total n sets and x is the value for the default set of cuts. The overall systematic uncertainty can be obtained by adding the four separate uncertainties in quadrature:

$$\mathrm{s_{total}} = \sqrt{\mathrm{s^2_{cuts}} + \mathrm{s^2_{bkg}} + \mathrm{s^2_{fits}} + \mathrm{s^2_{vtx}}} \tag{4.8}$$

Chapter 5

Summary and Future

5.1 Summary

I have presented the results of charm reconstruction using a constrained secondary vertex fit method in Au+Au collisions at $\sqrt{s_{NN}} = 200$ GeV. The measurement of D^0 and $\bar{D}^0$ signal was done using the pointing capabilities of silicon detectors (SVT, SSD) and using 24 million minimum bias good events collected during the 2007 RHIC-run. We observed a $D^0 + \bar{D}^0$ signal of significance $\sim 10\sigma$ when using a polynomial background estimation. The signal is stable when cuts are varied. Preliminary results show a $\bar{D}^0/D^0$ ratio of $\sim 1.05 \pm 0.19$ and therefore a vanishing μ_B at RHIC energies. The signal was measured for various p_T bins and uncorrected p_T spectra for two centralities are presented. This work also presents progress on the method for full topological reconstruction of open charm mesons. We find that the secondary vertex fit method yields a factor of two improvement in decay vertex resolution compared to traditional helix swimming methods (See Sec. 3.5.2). The method developed here is a baseline to analysis involving the future upgrade to STAR - The Heavy Flavor Tracker (HFT).

Also presented is the K^0_s measurement using the constrained vertex fit method. This is a proof of the method we use, and also shows the power of cutting on TCFIT variables and their uncertainties. Uncorrected p_T spectra of the K^0_s are presented in Chapter 4. With a clean sample of K^0_s, the possibility of reconstructing the decay,

$D^+ \longrightarrow K^0_s + \pi^+$ can also be explored. Measurement of additional charmed meson decay channels could help improve the current charm-cross section estimates.

5.2 Discussion of Results

We find a strong signal from first and second production when using a polynomial background subtraction method. The results were satisfying in terms of signal stability and $\bar{D^0}/D^0$ ratio. However, it shows indications of the signal, failing to scale with the number of binary collisions. The data set had a bias arising from the trigger requirement, this was taken into account when producing the invariant mass peaks, however the number of events used wasn't corrected for this effect. This gives some ambiguity to the results, although we expect this effect to be small. The cut on track momenta to select the high p_T tracks biases our sample. However, this cut is proved necessary since the resolution needed for this measurement is achieved only at higher momenta. From PYTHIA simulation, with a cut on daughter momenta as high as $p_T > 0.7$ GeV/c, there is 70-80% loss of candidates since the mean p_T of the D^0 is $\sim$ 1 GeV/c.

In order to draw meaningful insights from the p_T spectra obtained using the polynomial background subtraction method, and to compare the extracted parameters to predictions, we need to apply corrections to reconstruction, acceptance efficiency. This is usually done with an embedding sample where Monte Carlo D^0 events are mixed with real data background. The current sample of embedding has too few silicon hits and therefore cannot be used for making corrections to the raw spectrum.

The second production was expected to give us a handle on studying systematics. We saved additional information in the output to enable more physics possibilities such as calculation of charm elliptic flow (v_2). But the results from second production

are rather puzzling. Subtraction of same-sign background does not show a significant peak in the invariant-mass distribution. We required a minimum of two silicon hits for the tracks in second production, which gives a resolution of about 450-600 μm at 1 GeV/c, whereas the first production used a more stringent cut on silicon hits. Second production uses all tracks without discriminating on their charge, which increases the background levels; thus, more efficient methods are needed to extract the signal in the second production dataset. Limited resolution and the combinatorial background from the particle misidentification limits the physics possibilities of this analysis.

The multivariate analysis (TMVA) seems to be an effective tool for discriminating the signal from background. The preliminary TMVA results from embedding using same-sign background estimate is presented in Chapter 4 and the results are promising. A subset of the real data set shows a peak when using the TMVA. Tighter requirements on silicon hits may be needed to suppress the background. Analysis of the whole statistics available with TMVA, combined with other optimized cuts is ongoing, and would be the final phase of our efforts to measure charmed meson and to draw physics conclusions from the 2007 dataset.

5.3 Future Directions

Finding a signal peak in the invariant-mass with same sign/mixed event/rotational background method is the sorely needed advancement in this analysis. Once such a signal peak is found, the second production data set offers many physics possibilities, including a corrected p_T spectra and R_{AA}, a cross-section estimate and some charm elliptic flow measurements. This is important since it can shed some light on the energy-loss puzzle at RHIC, the cross-section discrepancy between STAR and PHENIX and the question of thermalization.

5.3.1 Corrected Spectrum

A p_T spectra corrected for acceptance and efficiency was used to extract the total charm cross section. This is done by fitting the corrected spectrum with an exponential function in transverse mass, $m_T - m_A$ for particle A, defined as,

$$\frac{1}{2\pi N_{\text{events}}} \frac{d^2N}{p_T dp_T dy} = \frac{dN_A}{dy} \frac{e^{-(m_T - m_A)/T_{\text{eff}}}}{2\pi T_{\text{eff}}(m_A + T_{\text{eff}})} \tag{5.1}$$

where, T_{eff} is the effective temperature of particle A. The low significance of the hadronically reconstructed open charm signal limits the number of p_T bins into which the signal can be divided. Therefore a fit is done and the integral of the fit function is used to obtain the midrapidity yields rather than using the midpoints of bins. From the fit one can extract, dN/dy and T_{eff}. The midrapidity measurement is then extrapolated to full rapidity range using a PYTHIA simulation of D^0 meson production in $p + p$ collisions [82] and an inclusive charm cross-section per nucleon-nucleon collision is extracted. This allows a comparison to pQCD predictions. The total cross section is calculated using,

$$\sigma_{c\bar{c}}^{NN} = \left(\frac{dN_{D^0+\bar{D}^0}/2}{dy} \right) \times (\sigma_{pp}^{\text{inelastic}} / N_{\text{bin}}^{\text{AuAu}}) \times (f/R). \tag{5.2}$$

The number of $c\bar{c}$ pairs is estimated using the ratio of $c\bar{c}$ to D^0 found in e^+e^- collisions, $R = 0.556 \pm 0.036$ is the ratio of $c\bar{c}$ pairs to D^0 mesons in e^+e^- collisions [85]. $f = 4.7 \pm 0.7$ is the extrapolation to the full rapidity range. In order to calculate the production of $c\bar{c}$ pairs per nucleon-nucleon collisions, the number of $c\bar{c}$ pairs must be multiplied by the proton-proton inelastic cross-section, $\sigma_{pp}^{\text{inelastic}} = 42$ mb [83]. This is divided by $N_{\text{bin}}^{\text{AuAu}}$, which is the number of binary collisions in Au+Au collisions at $\sqrt{S_{NN}} = 200$ GeV to calculate the yield per nucleon-nucleon collision.

The caveat here is that the Statistical Hadronization Model (SHM) predicts large

strangeness production and thus enhancement in the D_s yield compared to e^+e^- collisions [84], which can cause a reduction in the $c\bar{c}$ to D^0 ratio from the value 0.556. The charm cross section calculated is compared to pQCD predictions and experimentally measured values from PHENIX. There are still some unresolved discrepancies between the charm cross-section measurements of STAR and PHENIX.

In addition to the cross section measurement, the corrected p_T spectrum can be used to study the thermal freezeout. A blast-wave fit is used to extract the freezeout temperature, T_{fo} and average radial velocity, $\langle\beta\rangle$. However, the blast wave function has three parameters, and with only three p_T bins, the extraction of all these parameters is difficult. Earlier works on Cu+Cu data [65] used a comparison with lighter particle species with the assumption that the D^0 mesons are fully coupled with the lighter species in the later stages of the collision fireball. However, the results from that analysis showed that the D^0 are not fully coupled with the light particles and suggested a radial velocity smaller than those of lighter species.

5.3.2 Cross Section Discrepancy between STAR and PHENIX

The STAR measurement of the open charm cross section is roughly a factor of two larger than the PHENIX measurement. STAR measures a cross section of 1.29 $\pm$ 0.12 (stat.) $\pm$ 0.39 (sys.) mb in Au+Au collisions [87] and 1.4 $\pm$ 0.2 (stat.) $\pm$ 0.4 (sys.) mb in d+Au collisions [86]. The central Au+Au measures a value of 1.40 $\pm$ 0.11 (stat.) $\pm$ 0.39 (sys.) mb. The PHENIX experiment measures 0.622 $\pm$ 0.057 $\pm$ 0.160 mb in minimum bias Au+Au collisions and 0.567 $\pm$ 0.057 (stat.) $\pm$ 0.224 (syst.) mb in p+p collisions. Figure 5.2 shows the inclusive total charm cross section measured by STAR and PHENIX along with the pQCD calculations as a function of averaged number of binary collisions.

Both STAR and PHENIX show that the charm cross section scales with the number of binary collisions. This confirms the fact that charm is produced during the initial hard collisions and that its production cross section does not depend upon the collision system. STAR uses a combined fit of three spectra: direct D^0, muon measurements and nonphotonic electron measurements at low p_T. PHENIX is extracting charm cross section using an extrapolation from nonphotonic electron measurements. The PHENIX detector covers only 15% of the kinematical range, but due to low

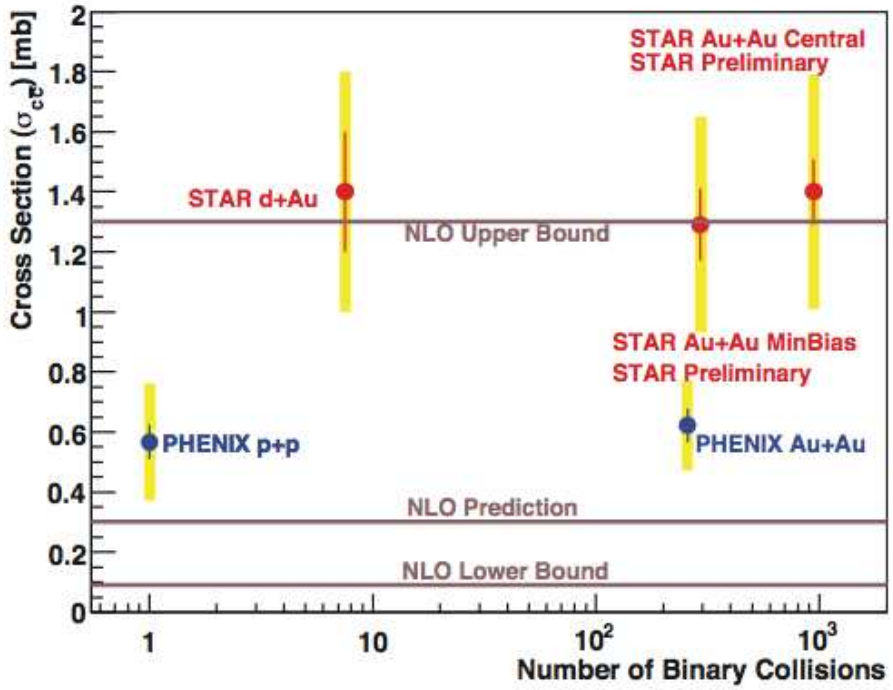

Figure 5.1: Inclusive charm cross-section measurements

material budget around the beam pipe, PHENIX is able to measure a clean electron sample. The charm cross section from NLO pQCD predictions has large systematic uncertainities and both experimental values are within the calculated range. Resolving the discrepancy between STAR and PHENIX cross-section measurements will be

an integral part of future measurements.

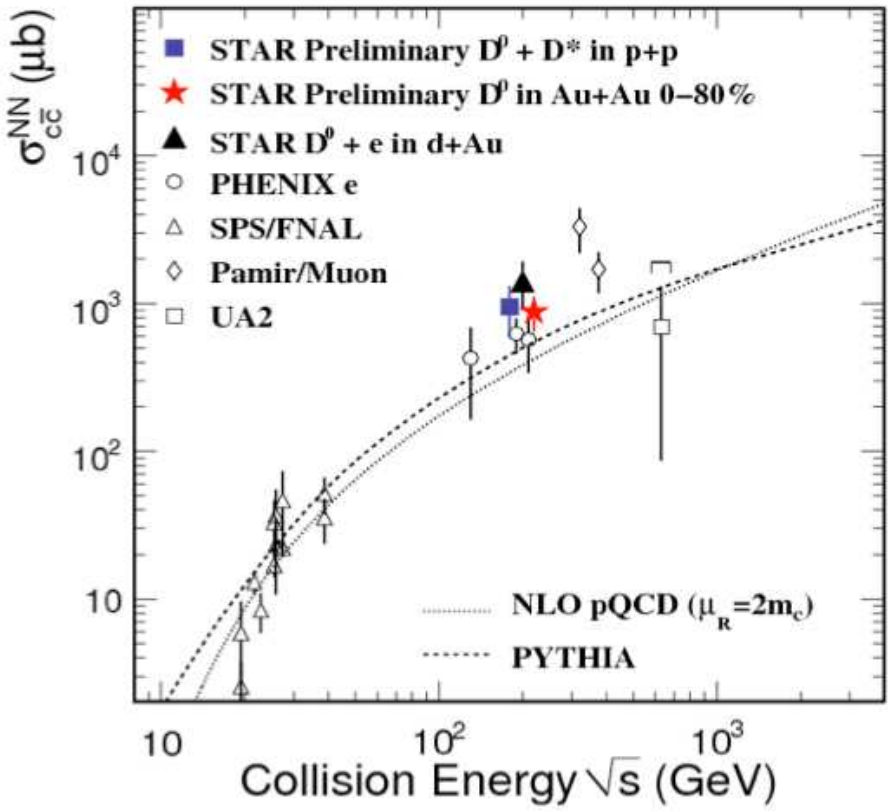

Figure 5.2: Inclusive charm cross-section measurements

A new microvertex detector (Heavy Flavor Tracker - HFT) is designed for STAR for exclusive charm measurement and it is expected to start taking data in 2013. This can unambiguously make measurements in the heavy quark sector and can answer the mechanism of partonic energy loss at RHIC. The technique developed here will be baseline for analyses involving HFT.

5.4 Results with Time-Of-Flight (TOF) Detector

The newly completed full barrel Time-Of-Flight detector (2π coverage in azimuthal direction) improved the particle identification capabilities of the STAR detector. The TOF detector has very good hadron identification capabilities to very low momentum by using velocity information, β. This can be combined with the dE/dx measurements from the TPC to obtain clean particle identification. I will present some of the new results obtained with TOF in the charm sector [88]. Measurements of D^0+D^* from 2009 p+p data give a charm cross section,

$$\frac{d\sigma^{c\bar{c}}}{dy} = 173 \pm 49(\text{stat.}) \pm 36(\text{syst.})\mu b$$

.

Measurements of D^0 from 2010 Au+Au data give a value of

$$\frac{d\sigma^{c\bar{c}}}{dy} = 210 \pm 56(\text{stat.}) \pm 52(\text{syst.})\mu b$$

.

These two values are consistent with the measurement from d+Au of 0.30±0.04±0.09 mb obtained by using the electron-D^0 correlated method. These results also confirms the already observed fact that charm follows binary collision scaling; however, this does not resolve the difference between STAR and PHENIX.

The D^0 nuclear modification factor was obtained by dividing D^0 yields in Au+Au collisions by those in p+p collisions scaled by the number of binary collisions. This is shown in Fig. 5.3. No obvious suppression is observed for $p_T < 3$ GeV/c. The blue dashed curve shows the blast-wave fit. The shaded band is the predicted D^0 R_{AA} with parameters from light-quark hadrons, and it shows difference from data. This

might indicate that D^0 mesons freeze out earlier than the light-quark hadrons.

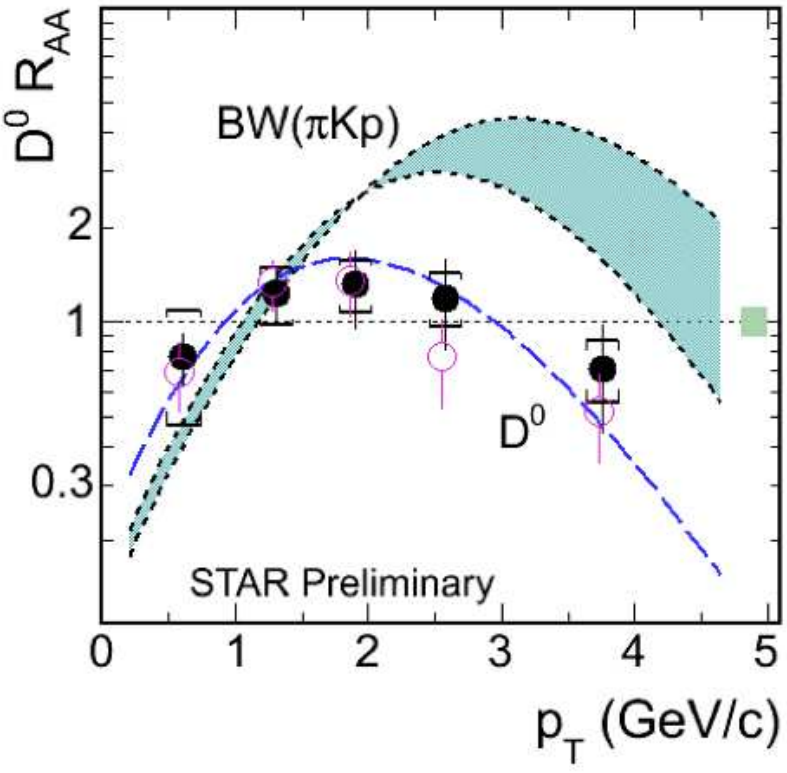

Figure 5.3: D^0 nuclear modification factor R_{AA} as a function of p_T

5.5 Future HFT with TOF

In the near future, the new microvertex detector, Heavy Flavor Tracker (HFT) will be built for STAR, which aims at measuring production rates, spectra and correlations in heavy ion collisions for heavy flavor hadrons. The HFT uses low mass, active pixel technology near the event vertex, which will provide ultimate resolution for secondary vertex reconstruction of D^0 mesons. The HFT can measure all major charm carrying particles including the charmed baryon, Λ_c. Therefore, the bottom contribution can be extracted from the nonphotonic spectrum. The difference in DCA of C and B decay

electrons can be utilized to separate their contributions to the total NPE spectra. With mature nonphotonic electron measurements, it would be possible to measure the bottom quark unambiguously. Figure 5.4 shows the performance example of the

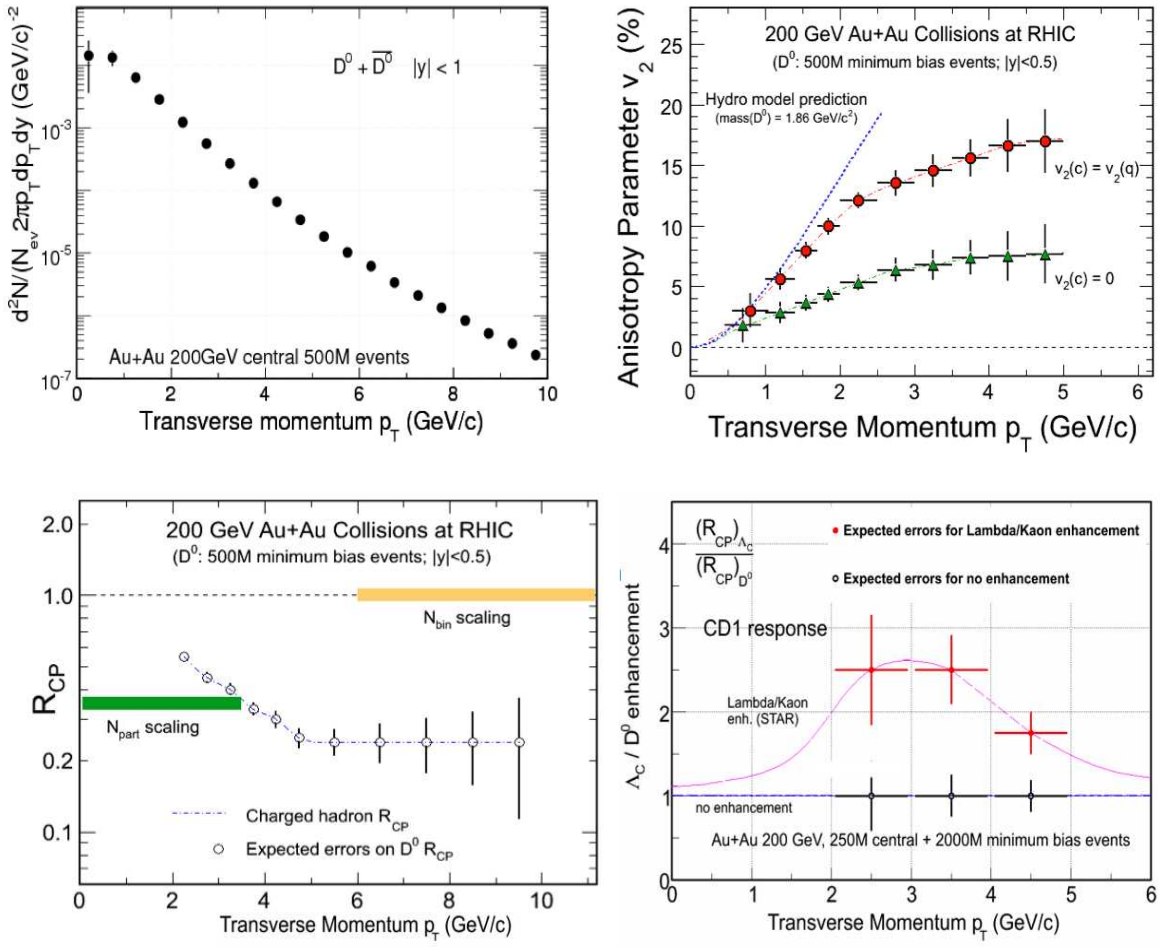

Figure 5.4: Key measurements with HFT - Error projections on spectra and flow measurements (upper panel), R_{CP} and Λ_c capabilities (lower panel)

HFT. HFT will be able to measure the spectra (left plot) and cross section with great accuracy extending the p_T reach. Figure 5.4 (right) shows the two extreme scenarios of the flow parameter, v_2. The error projections on v_2 allow us to distinguish the

two cases, where charm flows (red circles) and where charm does not flow (green triangles). HFT can perform precision low p_T flow measurements. Figure **??** shows the R_{CP} of the D^0(left) and ratio of Λ_c/D^0(right). HFT will be able to unambiguously measure R_{CP} directly for $p_T < 10\text{GeV}/c$ and can answer the heavy flavor energy loss puzzle at RHIC. Measuring the Λ_c/D^0 ratio is important since we want to know if the baryon-to-meson ratio is enhanced in the heavy quark sector as observed in those involving light quarks in the intermediate p_T region.

Appendix A

Track Finding and Reconstruction

The track reconstruction code associates hits measured with various detector components to reconstruct particle trajectories by fitting with an appropriate track model to determine the curvature, direction, and origin of the track. One must also determine the momentum and species identity of the particle.

The determination of the curvature is done by finding the hits reconstructed within the relevant detectors and fitting them with an appropriate function. Without making any assumptions as to the origin of the particles, the track parameters are determined except for the momentum vector. This is because the momentum vector seeks the vector at the vertex of origin of the particle. The point of origin can be any of the following: a main interaction vertex, a false vertex due to pile-up events, a secondary vertex or a scattering center. Thus, properties such as momentum vector and particle identity are calculated afterwards on the basis of track parameters and the known position of vertex of origin.

Global and Primary Tracks

STAR uses the notions of global, primary and secondary tracks. Primary tracks are those emanating directly from the main collision vertex whereas secondary tracks are produced by decay or interaction of primary tracks within the detector. The finite resolution of the track reconstruction , and kinematical focussing of decay products makes it difficult to distinguish between the many primary and secondary tracks.

One first analyzes all tracks as if they were secondary tracks, and do not include the main collision vertex. One then searchs for the fraction of those that present a good match with the main collision vertex and can be labelled as primaries. The tracks obtained in the first pass are labeled "global tracks" and are fitted without a vertex. The primary tracks are an extension of the global tracks including the vertex: their fit includes the vertex. STAR maintains a double list of tracks, global and primaries, where tracks that match the main vertex appear twice - once as global and once as primary. It is thus possible to recover the track parameters with and without the primary vertex for further analysis of decay topologies.

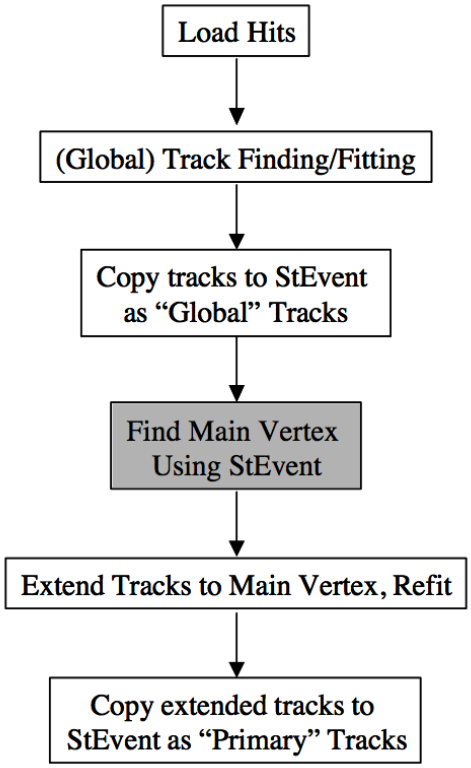

Figure A.1: Sequence of tasks involved in the track reconstruction

Track Search and Fitting Algorithm - The Kalman Filter Approach

In STAR, track reconstruction naturally proceeds from the outside to the inside, starting from the Time Projection Chamber (TPC) through the Silicon Strip Detector (SSD) to the Silicon Vertex Tracker (SVT). Track densities on outer layers are smaller than on the inner layers, therefore there is much less ambiguity in forming and following tracks. Tracking proceeds in two steps: candidate, or "seed" finding and track extension and fitting. The Kalman filter approach enables one to use the points available to refine the track parameters, and then extrapolate the tracks inward until no more tracks are found. A Kalman filter algorithm is used for this. The finder iterates on relevant data points to find sensible candidates. Given an existing segment of track, the Kalman methodology uses the knowledge provided by this segment to predict and estimate where the next point on the track might be. Once the new point is found, it will update the knowledge of the track. Thus, the approach can be qualified as "local" in space. No correlations between tracks are considered although hits may initially belong to more than one track. The search for each track is initiated with a call to a track seed finder. The search stops when the seed finder returns no seed. Track seeds are short track stubs consisting of a sequence of a few hits and they carry just enough information to enable a rough estimate of the track position, direction and curvature. Since its easier to find reliable track patterns in a low density environment, in STAR, the search for seeds proceeds from the outside to in. Thus the seeds are typically located near the periphery of the detector in STAR.

Since the seeds predominantly lie near the periphery of the detector, the Kalman search proceeds inward through the layers of the detector step by step. It is considered complete when the search reaches the innermost volume or a prescribed minimum

number of active detector layers has been crossed without finding matching hits. If no matching hit is found in a layer, then the given layer is skipped. Matching hits are found within a radius of confidence determined by the error parameters of the track. Candidates are deemed acceptable if the χ^2 increment is smaller than a set maximum. If more than one candidate hit satisfies the χ^2 requirement, one selects and adds to the track the hit with the lowest incremental χ^2 value. After each hit is added the track parameters are updated using the Kalman track model. Once the track search reaches the inner most detector volume, the track parameters are progressively refined [89].

The track search and event reconstruction proceeds in the following steps. First global tracks are identified and then copied to the STAR event model StEvent/StTrack. The main vertex finder is called next (with StEvent as the argument) to find the vertex of the event. If a vertex is found, the Kalman vertex finder is called once again to attempt an extension of all found tracks to the main vertex. Those tracks that were successfully extended to the main vertex are copied to the StEvent as primary tracks.

Appendix B

Relativistic Kinematics

Lorentz Transformation

When two observers are moving relative to each other, Lorentz transformations are used to relate their observations. Lorentz transformations operate on four-vectors (eg. space-time coordinate, four-momentum coordinate). Consider two inertial frames S and S'. S' is moving along the z-axis with a velocity v. The four-momentum coordinate in the two reference frames are related by:

$$E' = \gamma(E - \beta p_z), \tag{B.1}$$

$$p'_x = p_x, \tag{B.2}$$

$$p'_y = p_y, \tag{B.3}$$

$$p'_z = \gamma(p_z - \beta E), \tag{B.4}$$

where,

$$\beta = v/c, \tag{B.5}$$

$$\gamma = \frac{1}{\sqrt{(1-\beta^2)}}. \tag{B.6}$$

Similar is the transformation of the space-time coordinates. A four-vector is defined to be any quantity that transforms in this way. A quantity that remains unchanged

by a Lorentz transformation is called Lorentz scalar. With the given definitions of γ and β one finds that the following relations hold: E = γm, p = $\gamma\beta$m, p = βE with $\beta < 1$, $\gamma \geq 1$.

Rapidity and Pseudorapidity

Longitudinal distributions of secondary particles from high energy reactions are usually studied in rapidity, y or pseudorapidity, η variables. Rapidity is defined as:

$$y = \frac{1}{2}\ln\left(\frac{1+\beta}{1-\beta}\right) \tag{B.7}$$

where, $\beta = p/E$. Rapidity is additive under Lorentz transformation. The proof is given below.

Lets consider two inertial frames of reference. One frame is moving with a Lorentz boost in the z direction. Using Eq. (B.7), the rapidity in the new frame of reference can be written in terms of other variables as

$$y' = \frac{1}{2}\ln\left(\frac{E'+p'_z}{E'-p'_z}\right) \tag{B.8}$$

$$= \frac{1}{2}\ln\frac{\gamma(E-\beta p_z)+\gamma(p_z-\beta E)}{\gamma(E-\beta p_z)-\gamma(p_z-\beta E)} \tag{B.9}$$

$$= \frac{1}{2}\ln\frac{E+p_z-\beta(E+p_z)}{E-p_z+\beta(E-p_z)} \tag{B.10}$$

$$= \frac{1}{2}\ln\frac{(E+p_z)(1-\beta)}{(E-p_z)(1+\beta)} \tag{B.11}$$

$$= \frac{1}{2}\ln\frac{E+p_z}{E-p_z} + \frac{1}{2}\ln\frac{1-\beta}{1+\beta} \tag{B.12}$$

$$= y + a, \text{where}, a = \frac{1}{2}\ln\frac{1-\beta}{1+\beta}. \tag{B.13}$$

(B.14)

This means that the shape of the rapidity distribution is invariant under Lorentz

transformation and acquires only a parallel shift when going from one reference frame to another.

For ultrarelativistic particles $E \approx p$ and $\cos(\theta) = p_z/\mathbf{p}$, and rapidity becomes equivalent to another variable called pseudorapidity defined in Eq. (3.4)

Proof:

Eqn. A.7 can be rewritten as:

$$y = \frac{1}{2}\ln\left(\frac{E+p_z}{E-p_z}\right) \tag{B.15}$$

$$= \frac{1}{2}\ln\left(\frac{1+\frac{p_z}{E}}{1-\frac{p_z}{E}}\right) \tag{B.16}$$

$$= \frac{1}{2}\ln\left(\frac{1+\frac{p_z}{p}}{1-\frac{p_z}{p}}\right) \tag{B.17}$$

$$= \frac{1}{2}\ln\left(\frac{1+\cos\theta}{1-\cos\theta}\right) \tag{B.18}$$

$$= \frac{1}{2}\ln\left(\tan^{-1}(\frac{\theta}{2})\right)^2 \tag{B.19}$$

$$= -\ln\left(\tan\frac{\theta}{2}\right) \tag{B.20}$$

$$= \eta \tag{B.21}$$

Appendix C

Geometrical Picture of Collisions

The simple dependence of the total cross section of relativistic heavy ion reactions on the sizes of colliding nuclei suggests an important role of the collision geometry. The collision can be described in terms of impact parameter b, $N_{\rm part}$ and $N_{\rm binary}$. $N_{\rm part}$ is the number of incoming nucleons in the overlapping region that undergoes at least one collision. In Fig. C.1 $N_{\rm part}$ corresponds to the nucleons in the shaded area. In the case of Au+Au collisions, the maximum value of $N_{\rm part}$ is $197\times\ 2 = 394$.

$N_{\rm binary}$ is the total number of inelastic nucleon-nucleon collisions.

The Impact parameter (b) is the distance between the centers of the colliding ions. It is used as a measure of the centrality of the collision. The most central collisions have zero impact parameter.

Figure C.1 shows a schematic of the collision process.

The colliding nuclei are assumed to travel in straight lines and only the geometrically overlapping parts of them interact (participants) and what remains are the spectators. With femtoscopic length scales involved, estimates of the impact parameter (b), $N_{\rm part}$ and $N_{\rm binary}$ may seem intractable. However, the participant-spectator picture allows for a simple calculation of the number of nucleons involved in a collision with a given value of impact parameter. This is done using theoretical techniques referred to as Glauber models. It assumes that the nucleons in each nuclei are hard spheres distributed according to the nuclear density function (e.g. Saxon-Woods)

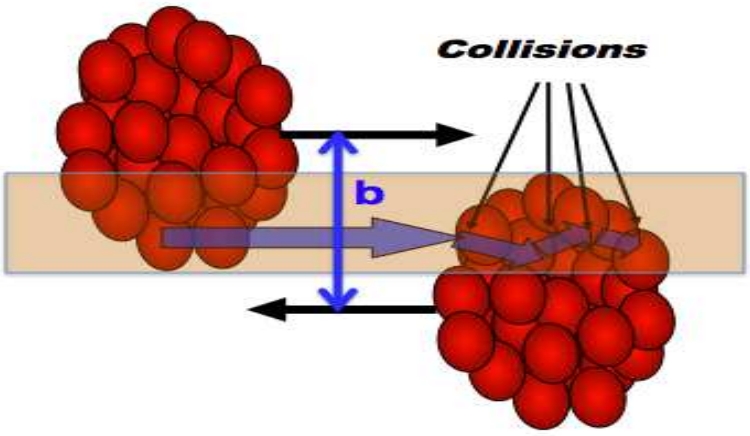

Figure C.1: Schematic of collision geometry

and they move along parallel, straight lines, interacting with nucleons from the other nucleus with cross sections known from elementary processes. Nucleons are treated as free particles. When counting only the first collisions, one obtains the number of nucleon participants (N_{part}), or wounded nucleons. By counting also the subsequent collisions one obtains the total number of binary collisions (N_{binary}). Results of the Glauber model calculation are shown in Fig. C.2

The calculation of impact parameter is done by looking at the total multiplicity, transverse energy etc., and using the Glauber model. For example, centrality $b = 0 - 4.5$fm gives $\langle b \rangle = 3$ fm which translates to 5% top central (assuming Au radius $\sim$ 7fm.). This gives about 1000 binary collisions per event.

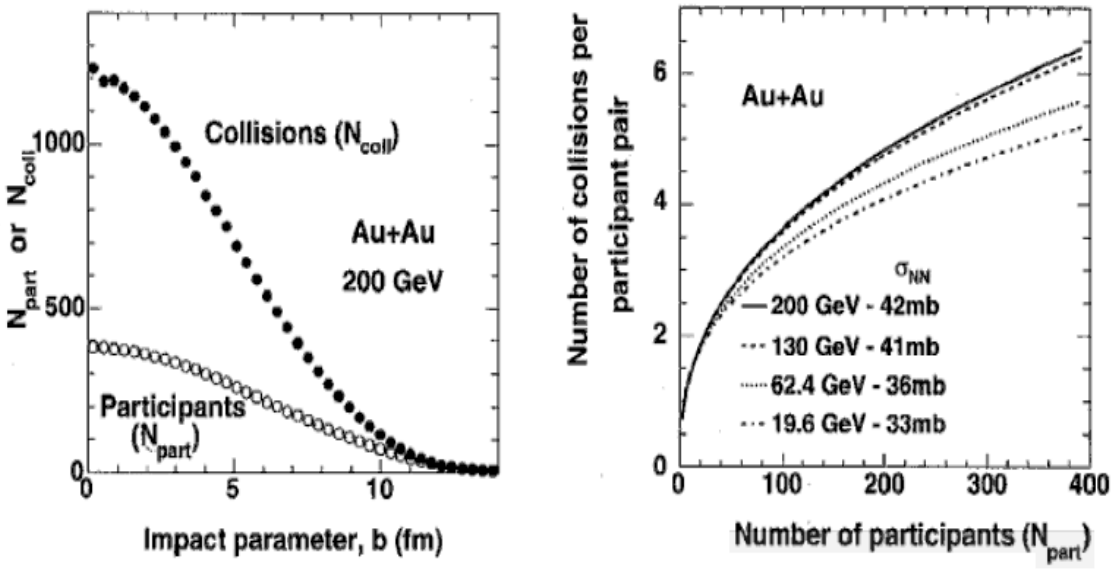

Figure C.2: Glauber model calculation for Au+Au collisions

Appendix D

Effective Signal

The effective signal, S_{eff}, is often used as a measure of the signal strength of resonances where a given signal has to be judged in the presence of an underlying background. In cases, where there is no background, S_{eff} is the signal only, $S = S_{\text{eff}}$.

Significance of a Signal

In the following we assume that we conduct a measurement and observe a total count T, which is the sum of actual signal S and background B. Therefore the actual signal can be obtained by,

$$S = T - B, \tag{D.1}$$

where B has to be evaluated through some means. In the case of a neutral D-meson measurement, T would be number of opposite-sign pairs in some mass range and B would be the number of same-sign pairs for the same mass range. The significance of the signal is expressed in terms of signal yield divided by the statistical uncertainity of the signal, S/∂S. A signal such as $S = 10\pm5$ is often referred to as a 2σ signal. When expressing signal in terms of σ one assumes, not always correctly, that the uncertainities are gaussian distributed. Using a gaussian error propagation, the uncertainty on S in Eqn. (D.1) is

$$\partial S = \sqrt{\left(\frac{\delta S}{\delta T}\delta T\right)^2 + \left(\frac{\delta S}{\delta B}\delta B\right)^2}, \tag{D.2}$$

$$= \sqrt{(\delta T)^2 + (\delta B)^2}. \tag{D.3}$$

(D.4)

Since $T = S + B$ and assuming simple counting statistics, $\delta S = \sqrt{S}$ and $\delta B = \sqrt{B}$, we obtain:

$$\delta S = \sqrt{S + 2B}. \tag{D.5}$$

In cases where the background is determined from fits or event mixing, the statistical uncertainty of the background is often neglected and Eqn. (D.5) becomes, $\delta S = \sqrt{S + B}$

Therefore the significance of the measurement becomes,

$$\frac{S}{\delta S} = \frac{S}{\sqrt{S + 2B}} \tag{D.6}$$

Background Free Equivalent - Effective Signal

Effective signal refers to the significance in the absence of any background. In other words, S_{eff} is the "background free equivalent". Significance of S_{eff} is:

$$\frac{S_{\text{eff}}}{\delta S_{\text{eff}}} = \frac{S_{\text{eff}}}{\sqrt{S_{\text{eff}}}} = \sqrt{S_{\text{eff}}}. \tag{D.7}$$

Since we require that S_{eff} has the same significance as in the case with background,

$$\frac{S}{\delta S} = \frac{S_{\text{eff}}}{\sqrt{S_{\text{eff}}}}, \tag{D.8}$$

$$\frac{S}{\sqrt{S + 2B}} = \sqrt{S_{\text{eff}}}. \tag{D.9}$$

Therefore we obtain S_{eff} as

$$S_{\text{eff}} = \frac{S}{2\frac{B}{S} + 1}. \tag{D.10}$$

This is the signal strength in the absence of any background that has same significance as a measurement with background. Quoting S_{eff} avoids asking what is the signal-to-background ratio. Another advantage is optimization of cuts. Sometimes tuning

cuts to reduce background also reduces the signal. Since S_{eff} reflects both signal and background, it's the simplest measure to judge the optimization study.

References

[1] K. Nakamura *et al.* (Particle Data Group), "(2010) and 2011 partial update for the 2012 edition", J. Phys. G **37**, 075021 (2010).

[2] J. Adams *et al.*, "Experimental and Theoretical Challenges in the Search for the Quark Gluon Plasma: The STAR Collaboration's Critical Assessment of the Evidence from RHIC Collisions", Nucl. Phys. A **757**, 102 (2005).

[3] K. Yagi, T. Hatsuda and Y. Miake, "Quark-Gluon plasma: from big bang to little bang", Cambridge University Press (2005).

[4] B. Muller, "The Limits of Ordinary Matter", Science Magazine **332 (6037)**, 1513 (2011).

[5] S. Bethke, "Experimental Tests of Asymptotic Freedom", Prog. Part. Nucl. Phys. **58**, 351 (2007).

[6] J. Kogut, "The lattice gauge theory approach to quantum chromodynamics", Rev. Mod. Phys. **55**, 775 (1983).

[7] F.Karsch, "Lattice QCD at High Temperature and Density", Lect.Notes Phys. **583**, 209 (2002).

[8] M.Gyulassy and L. McLerran, "New Forms of QCD Matter Discovered at RHIC", Nucl. Phys. A **750**, 30 (2005).

[9] F.Karsch E.Laermann and A.Peikert, "The Pressure in 2, 2+1 and 3 Flavour QCD", Phys.Lett. B **478**, 447 (2000).

[10] T.Matsui and H.Satz, "J/Psi Suppression by Quark-Gluon Plasma Formation", Phys. Lett. B **178**, 416 (1986).

[11] O.Kaczmarek, F.Karsch, E.Laermann and M. Lutgemeir, "Heavy Quark Potentials in Quenched QCD at High Temperature", Phys. Rev. D **62**, 034021 (2000).

[12] J.Schaffner-Bielich, "What is so special about strangeness in hot matter?", J. Phys. G **30 R**, 245 (2004).

[13] D.A. Appel, "Jets as a probe of quark-gluon plasmas", Phys. Rev. D **33**, 717-722 (1986).

[14] W.Reisdorf and H.G. Ritter, "Collective flow in Heavy-Ion Collisions", Annu. Rev. Nucl. Part. Sci. **47**, 663 (1997).

[15] J. Y. Ollitrault, Phys. Rev. D **46**, 229 (1992); 48, 1132 (1993), S. Voloshin and Y. Zhang, Z. Phys. C **70**, 665 (1996), Plastic Ball Collaboration, H.H. Gutbrod, K. H. Kampert, B. Kolb, A.M. Poskanzer, H.G.Ritter, R. Schicker, H.R. Schmidt, Phys. Rev. C **42**, 640 (1990).

[16] H. Sorge, "Elliptical Flow: A Signature for Early Pressure in Ultrarelativistic Nucleus-Nucleus Collisions", Phys. Rev. Lett. **78**, 2309 (1997).

[17] P.F. Kolb, J.Sollfrank and U. Heinz, "Anisotropic flow from AGS to LHC energies", Phys. Rev. C **459**, 667 (1999).

[18] Peter Steinberg, "Hotter, Smaller, Denser, Faster...and Nearly-Perfect: What's the matter with RHIC?", 2007 J. Phys.: Conf. Ser. **69**, 012032 (2006).

[19] Ulrich W. Heinz, "Thermalization at RHIC", AIP Conf. Proc. **739**, 163 (2005).

[20] S. S. Adler et al., "Nuclear Modification of Electron Spectra and Implications for Heavy Quark Energy Loss in Au+Au Collisions at $\sqrt{S_{NN}}$ = 200 GeV", Phys. Rev. Lett. **96**, 032301 (2006).

[21] A. Adare et al., "Energy Loss and Flow of Heavy Quarks in Au+Au Collisions at $\sqrt{S_{NN}}$ = 200GeV", Phys. Rev. Lett. **98**, 172301 (2007).

[22] Yu. L. Dokshitzer and D. E. Kharzeev, "Heavy-quark calorimetry of QCD matter", Phys. Lett. B **519**, 199 (2001).

[23] M. Djordjevic M. Gyulassy and S. Wicks, "Open Charm and Beauty at Ultrarelativistic Heavy Ion Colliders", Phys. Rev. Lett. **94**, 112301 (2005)

[24] Z. Lin and M. Gyulassy, "Open charm as a probe of preequilibrium dynamics in nucelar collisions", Phys. Rev. C **51**, 2177 (1995)

[25] C. Adler, et al. (STAR Collaboration), "Disappearance of back-to-back high pT hadron correlations in central Au+Au Collisions at $\sqrt{S_{NN}}$ = 200GeV", Phys. Rev. Lett. **90**, 082302 (2003).

[26] C. Adler, et al. (STAR Collaboration), "Centrality dependence of high pT hadron suppression in Au+Au collisions at $\sqrt{S_{NN}}$ = 130GeV", Phys. Rev. Lett. **89**, 202301 (2002).

[27] J. Adams, et al. (STAR Collaboration), "Evidence from d+Au measurements for final-state suppression of high pT hadrons in Au+Au collisions at RHIC", Phys. Rev. Lett. **91**, 072304 (2003).

[28] Shusu Shi, "The elliptic flow of multi-strange hadrons in $\sqrt{S_{NN}}$ = 200GeV Au+Au collisions at STAR" Nucl. Phys. A **862-863**, 263c (2011).

[29] M. A. C. Lamont (STAR Collaboration), "Recent results on strangeness and Heavy Flavour at RHIC", J. Phys. Conf. Serv. **50**, 192 (2006).

[30] C. Adler, et al. (STAR Collaboration), "Mid-rapidity Λ and $\bar{\Lambda}$ Production in Au+Au Collisions at $\sqrt{S_{NN}} = 130$ GeV", Phys. Rev. Lett. **89**, 092301 (2002).

[31] J. Adams, et al. (STAR Collaboration), "Multi-Strange Baryon Production in Au+Au collisions at $\sqrt{S_{NN}} = 130$ GeV", Phys. Rev. Lett. **92**, 182301 (2004).

[32] STAR Collaboration, "Kaon Production and Kaon to Pion Ratio in Au+Au Collisions at $\sqrt{S_{NN}} = 130$ GeV", Phys. Lett. B **595**, 143 (2004).

[33] M. G. Mustafa, "Energy loss of charm quarks in the quark-gluon plasma: Collisional vs radiative losses", Phys. Rev. C **72**, 014905 (2005); M. G. Mustafa and M. H. Thoma, Acta Phys. Hung. A **22**, 93 (2005)

[34] A. K. Dutt-Mazumder, J. Alam, P. Roy and B. Sinha, "Stopping power of hot QCD plasma", Phys. Rev. D **71**, 094016 (2005).

[35] M. Djordjevic, "Collisional Energy Loss in a Finite Size QCD Matter", Phys. Rev. C **74**, 064907 (2006).

[36] M. Djordjevic, "Heavy Quark Energy Loss: Collisional vs Radiative", Nucl. Phys. A **783**, 197c (2007).

[37] B. I. Abelev et al. (STAR Collaboration), "Transverse momentum and centrality dependence of high p_T nonphotonic electron suppression in Au+Au collisions at $\sqrt{S_{NN}} = 200$ GeV", Phys. Rev. Lett., 98, 192301 (2007).

[38] X. Dong, "Open charm Production at RHIC", Acta Physica Polonica B Proceedings Supplement (2008).

[39] M. Djordjevic, M. Gyulassy, "The Ter-Mikayelian Effect on QCD Radiative Energy Loss", Phys. Rev. C **68**, 034914 (2003).

[40] B. G. Zakharov, "Coherent final state interaction in jet production in nucleus-nucleus collisions", JETP Lett. **76**, 201 (2002).

[41] M. Djordjevic, M. Gyulassy, "Heavy Quark Radiative Energy Loss in QCD Matter", Nucl. Phys. A **733**, 265 (2004).

[42] S. Wicks et al., "Elastic, inelastic, and path length fluctuations in jet tomography", Nucl. Phys. A **784**, 426 (2007).

[43] F. Laue (STAR Collaboration), "Studying charm quark elliptic flow via single electron measurements", J. Phys. G: Nucl. Part. Phys. **31**, S1121 (2005).

[44] A. Adler et al. (PHENIX Collaboration), "Measurement of single electron event anisotropy in Au+Au collisions at $\sqrt{S_{NN}} = 200$ GeV", Phys. Rev. C **72**, 024901 (2005).

[45] S. Batsouli, S. Kelly, M. Gyulassy, "Does the Charm Flow at RHIC?" Phys. Lett. B **557**, 26 (2003).

[46] G.Wang (STAR Collaboration), "Non-photonic electron-hadron correlations and non-photonic electron v_2 at STAR/RHIC", Nucl.Phys. A **855**, 319 (2011).

[47] B. Zhang, L.W. Chen, C.Ko, "Charm elliptic flow in Au+Au collisions at RHIC", Nucl. Phys. A **774**, 665 (2006).

[48] M. Cacciari, P. Nason, R. Vogt, "QCD Predictions for Charm and Bottom Quark Production at RHIC", Phys. Rev. Lett. **95**, 122001 (2005).

[49] J. Bouchet, "Heavy Flavor Tracker (HFT): A new inner tracking device at STAR", Nucl. Phys. A **830**, 636c (2009).

[50] H. Hahn et al., "The RHIC design overview", Nuclear Instruments and Methods in Physics Research A **499**, 245 (2003).

[51] BRAHMS Collaboration, "The BRAHMS experiment at RHIC", Nuclear Instruments and Methods in Physics Research A **499**, 437 (2003).

[52] The PHOBOS Collaboration, "The PHOBOS detector at RHIC", Nuclear Instruments and Methods in Physics Research A **499**, 603 (2003).

[53] The PHENIX Collaboration, "PHENIX Detector overview", Nuclear Instruments and Methods in Physics Research A **499**, 469 (2003).

[54] STAR Collaboration, "The STAR time projection chamber: a unique tool for studying high multiplicity events at RHIC", Nuclear Instruments and Methods in Physics Research A **499**, 659 (2003).

[55] K. H. Ackermann et al., "The forward time projection chamber in STAR", Nuclear Instruments and Methods in Physics Research A **499**, 713 (2003).

[56] J. Abele et al., "The laser system for the STAR time projection chamber", Nuclear Instruments and Methods in Physics Research A **499**, 692 (2003).

[57] The Home page of the SVT Subsystem of STAR http://www.star.bnl.gov/public/svt/svt.htm

[58] R. Bellwied et al., "The STAR Silicon Vertex Tracker: A large area Silicon Drift Detector", Nuclear Instruments and Methods in Physics Research A **499**, 640 (2003).

[59] Y. V. Fisyak et al., "Overview of the Inner Silicon detector alignment procedure and techniques in the RHIC/STAR experiment", J. Phys.: Conf. Ser. **119**, 032017 (2008); S.Margetis et al., "Alignment experience in STAR", CERN Yellow report (2007).

[60] S. Bouvier, "The silicon strip detector for STAR", Nuclear Instruments and Methods in Physics Research A **549**, 27 (2005).

[61] M. Beddo et al., "The STAR Barrel Electromagnetic Calorimeter", Nuclear Instruments and Methods in Physics Research A **499**, 725 (2003).

[62] C.E. Allgower et al., "The STAR endcap electromagnetic calorimeter", Nuclear Instruments and Methods in Physics Research A **499**, 740 (2003).

[63] W. J. Llope for the STAR TOF Group, "The large-area time-of-flight upgrade for STAR" Nuclear Instruments and Methods in Physics Research B **241** 306 (2005).

[64] F.S. Bieser et al., "The STAR trigger", Nuclear Instruments and Methods in Physics Research A **499**, 766 (2003).

[65] S. Baumgart, Yale University, "A study of Open Charm Production in Heavy Ion Collisions of Center-of-Mass Energy 200 GeV per Nucleon", PhD Thesis (2010).

[66] W. J. Llope et al., "The TOFp/pVPD Time of Flight System for STAR", Nucl. Instrum. Meth. A **522**, 252 (2004).

[67] G. Bocquest et al., "Transverse momentum spectra of charged particles in p$\bar{p}$ collisions at $\sqrt{s}$=630GeV", Phys Lett B **366**, 434 (1996).

[68] "GEANT - Detector Description and Simulation Tool"
http://wwwasd.web.cern.ch/wwwasd/geant/.

[69] The STAR Experiment webpage, STAR Geometry in simulation and reconstruction
- http://drupal.star.bnl.gov/STAR/comp/prod/MCGeometry.

[70] "The STAR Experiment webpage - Centrality in Year 7 Au+Au 200 GeV",

[71] M. L. Miller et al., "Glauber modeling in High-Energy Nuclear Collisions", Annu. Rev. Nucl. Part. Sci. **57**, 205 (2007).

[72] Fisyak Y. V. et al., "Overview of the Inner Silicon detector alignment procedure and techniques in the RHIC/STAR experiment.", J. Phys.: Conf. Ser. **119** 032017 (2008).

[73] Hans Bichsel, "A method to improve tracking and particle identification in TPCs and silicon detectors", Nucl. Instrum. Meth. A **562**, 154 (2006).

[74] B. I. Abelev et al., "Strange particle production in p+p collisions at $\sqrt{S}$ = 200GeV", Phys. Rev. C **75**, 064901 (2007).

[75] W. D. Hulsbergen, "Decay Chain Fitting with a Kalman Filter", Nucl. Instrum. Meth. A **552**, 566 (2005).

[76] J. Vanfossen, personal communication.

[77] A. Hoecker et al., "TMVA - Toolkit for Multivariate Data Analysis", Proceedings of Science PoS ACAT **040**, (2007).

[78] Adler et al., STAR Collaboration, "Centrality dependence of charm production from single electrons measurement in Au+Au collisions at $\sqrt{S_{NN}}$ = 200 GeV", Phys. Rev. Lett. **94**, 082301, (2005).

[79] P. Braun-Munzinger et al., "Maximum Relative Strangeness Content in Heavy Ion Collisions Around 30 A. GeV", Nucl. Phys. A **697**, 902 (2002).

[80] P. Braun-Munzinger et al., "Hadron production in Au-Au collisions at RHIC", Phys. Lett. B **518** 41 (2001).

[81] Daniel Magestro, "Evidence for chemical equillibrium at RHIC", J. Phys. G **28**, 1745 (2002).

[82] T. Sjostrand et al., "High-Energy-Physics event generation with PYTHIA 6.1", Comput. Phys. Commun. **135**, 238 (2001).

[83] M. Honda et al., "Inelastic cross-section for p-air collisions from air shower experiment and total cross-section for p p collisions at SSC energy", Phys. Rev. Lett. **70**, 525 (1993).

[84] I. Kuznetsova and J. Rafelski, "Heavy Flavor Hadrons in Statistical Hadronization of Strangeness-rich QGP", Eur. Phys. J. **C51**, 113 (2007).

[85] L. Gladilin, "Charm Hadron Production Fractions", arXiv:hep-ex/9912064v1 (1999).

[86] J. Adams et al. (STAR Collaboration), "Open Charm yields in d+Au collisions at $\sqrt{S_{NN}}$ = 200 GeV", Phys.Rev. Lett. **94** 062301 (2005).

[87] B. I Abelev et al. (STAR Collaboration), "e-print Arxiv: nucl-ex/0805.0364 (2008).

[88] Y. Zhang, "Open charm hadron measurement in p+p and Au+Au collisions at $\sqrt{S_{NN}}$ = 200 GeV in STAR", Quark Matter Conference, Annecy, France (2011).

[89] A. Rose, "STAR Integrated Tracker", CHEP, 24-28 March 2003, La Jolla, California, ePrint nucl-ex/03070015.

[90] D. Chakraborty and J. D. Hobbs, "Alignment Strategy for the SMT Barrel Detectors", October 13, 1999, D0 Note (unpublished).